

离子阱系统中的量子操控

(申请清华大学理学博士学位论文)

培养单位：交叉信息研究院

学 科：物理学

研 究 生：安 硕 明

指导教师：金 奇 奂 副 教 授

二〇一七年四月

Quantum Control in the trapped ion system

Dissertation Submitted to
Tsinghua University
in partial fulfillment of the requirement
for the degree of
Doctor of Philosophy
in
Physics
by
Shuoming An

Dissertation Supervisor : Associate Professor Kihwan Kim

April, 2017

关于学位论文使用授权的说明

本人完全了解清华大学有关保留、使用学位论文的规定，即：

清华大学拥有在著作权法规定范围内学位论文的使用权，其中包括：（1）已获学位的研究生必须按学校规定提交学位论文，学校可以采用影印、缩印或其他复制手段保存研究生上交的学位论文；（2）为教学和科研目的，学校可以将公开的学位论文作为资料在图书馆、资料室等场所供校内师生阅读，或在校园网上供校内师生浏览部分内容；（3）根据《中华人民共和国学位条例暂行实施办法》，向国家图书馆报送可以公开的学位论文。

本人保证遵守上述规定。

（保密的论文在解密后应遵守此规定）

作者签名：_____

导师签名：_____

日 期：_____

日 期：_____

摘 要

量子涨落关系被认为是热力学第二定律在量子世界中的更精确的体现。为了验证量子Jarzynski等式，量子功的两点测量是必须的。我们利用声子的投影测量实现了对量子功的直接测量并验证了量子Jarzynski等式。在进行声子投影测量的时候，我们利用了二能级的量子绝热捷径。量子绝热捷径将会缩减较长的绝热时间到任意短的时间。之后针对声子态的不同的量子绝热捷径在实验上被实现并比较了。在所有这些方案中，逆绝热方案由于它的鲁棒性和不需要更多的功需求而脱颖而出。为了提升囚禁离子的能力，新的五段刀片径被研发并测试。其所需的工具和设备也在本文中被详细描述。未来几个新实验得计算和模拟也在本文中展示。

关键词：离子阱；量子信息；量子热力学；量子绝热捷径

Abstract

The Quantum fluctuation relations can be regarded as the more accurate version of the second law of thermodynamics in the quantum regime. To test the quantum Jarzynski equality, the two points measurement of the quantum work is required. We utilize the phonon projective measurement to realize the directive measurement of quantum work and test the quantum Jarzynski equality with the trapped ion. When realizing the phonon projective measurement, the shortcut to adiabaticity (STA) for the two level system is applied. The STA will reduce the long duration required by the adiabatic process to arbitrarily short one. Later different STA protocols for the motional states are realized and compared. Among all different protocols, the counter-diabatic driving protocol stands out for its robustness and without more payment of work. To improve the trapping condition, a new five segments blade trap is developed and tested. The tools and equipments for developing the new trap are described in this thesis. Several theoretical calculation and simulation for the future experiments are also presented.

Key words: Trapped Ion; Quantum Information; Quantum Thermodynamics, Quantum Adiabatic shortcut

Table of contents

List of figures	v
1 Introduction	1
1.1 Quantum control with the trapped ion	2
1.2 Thesis organization	3
2 Yb ion and ion trap	5
2.1 The Paul trap	5
2.2 CPO simulation	8
2.3 Micro-motion compensation	11
2.4 Dimension analysis of the background gas collision rate	14
2.5 Vapor pressure	15
2.6 Laser ionization, cooling, pumping and detecting of Yb ion	16
3 laser-ion interaction	19
3.1 Coherent control with lasers	19
3.1.1 Radiation patterns and C.G. coefficients	20
3.1.2 One beam Zeeman qubit flipping with pulse lasers	24
3.1.3 Two beam Raman qubit flipping	27
3.1.4 Spin-dependent force	31
3.1.5 Spin-independent force, squeezing, beam splitting operation and the fidelity measurement.	33
3.1.6 Mølmer-Sørensen gate and XY model	37

3.1.7	A multi-species entanglement scheme	39
3.1.8	The mode of a chain of mixed ions	40
3.2	Quantum control in the dissipated way	41
3.2.1	Natural reservoir	42
3.2.2	Engineered reservoir	44
4	Experimental setup	51
4.1	The vacuum, blade traps, helical resonators and filters	51
4.2	Diode laser systems	60
4.3	The pulse laser system	68
4.4	The detecting system	71
5	Experimental test of the quantum Jarzynski equality	75
5.1	The quantum Jarzynski equality	75
5.2	The thermal state preparation	76
5.3	Phonon projective measurement	77
5.4	Applying work with spin dependent force and the fast effective adiabatic ramp	83
5.5	Work distribution, Jarzynski equality and the Crooks relation	86
6	Experimental realization of Shortcut to adiabaticity	89
6.1	Transport in the phase space	91
6.2	Transitionless driving	91
6.3	Unitarily equivalent driving	93
6.4	Multi-frequency driving	95
7	Conclusion and outlook	99
	References	101
	Appendix A Codes related with CPO	107
	Appendix B Breit-Rabi-Zeeman splitting	113

Appendix C	Debye-Waller factor and the Lamb-Dicke parameter	117
Appendix D	RF switch without dead time and the drawing of the invar confocal cavity	121
Appendix E	The code used to calculate the position and mode structure of a mixed ion chain	123

List of figures

2.1	The Four rod trap.	6
2.2	The instantaneous potential in the four rod trap.	7
2.3	The potential in the center zone of the trap simulated with CPO.	10
2.4	The electric field generated by the micro-motion compensation electrodes. .	11
2.5	The excited state population for different laser detuning under the influence of micro-motion.	13
2.6	The laser path before the trap for basic operations.	16
2.7	The lasers used for cooling, pumping and detecting.	18
3.1	The radiation pattern for the dipole transition.	21
3.2	The radiation pattern for the quadrupole transition.	22
3.3	The CG coefficient for the dipole transition between S and the lower P states of Yb 171 ion.	23
3.4	The single beam flipping.	25
3.5	The time evolution of the single beam flipping for the Zeeman qubit.	26
3.6	The Raman qubit flipping.	28
3.7	Carrier, blue and red Rabi flipping.	30
3.8	The spin dependent force configuration.	31
3.9	The phase space trajectory of the ion experienced the spin dependent force.	32
3.10	The spin dependent force test data.	32
3.11	The Spin-independent force scheme.	33
3.12	The size of the coherent states dependent on the time.	35

3.13	The squeezed state.	35
3.14	The time scan of the Beam splitting operation.	36
3.15	The beam splitting operation.	37
3.16	The position and mode structure of a mixed ion chain.	41
3.17	The optical pumping speed.	42
3.18	The heating rate measurement of the blade trap.	44
3.19	The intuitive illustration from the view of coherent population trapping(CPT) to explain the engineering reservoir.	45
3.20	The simulation to choose the best pumping speed.	46
3.21	The fidelity against time for the coherent state reservoir.	46
3.22	The phonon distribution and Wigner quasi-distribution of the final state in the engineered reservoir for coherent state.	46
3.23	The phonon distribution and Wigner quasi-distribution of the squeeze state generated by the engineered reservoir.	47
3.24	The even cat states generated by the engineered reservoir.	48
3.25	The time evolution of the cat states in the time dependent reservoir.	49
3.26	The time evolution of the σ_z operation for the cat code.	50
4.1	The vacuum and detecting set up.	53
4.2	The 5 segment blade trap.	54
4.3	The vacuum chamber and the trap with holder and ovens inside.	55
4.4	Helical resonator's Q	57
4.5	The picture of the helical resonator and the trap frequency-power relation.	58
4.6	The circuit model simulation of the bifilar helical resonator connected with voltage picker and the rectifier.	59
4.7	The simulation of the mixer used as the voltage controlled attenuator.	60
4.8	The board drawings of the filter designed to apply DC on the RF coil and DC blades.	61
4.9	Reflected fields from cavity due to several round-trips inside the cavity, cited from Ref. [1].	62

4.10	The reflection signal and its phase.	63
4.11	The error signal for slow and fast modulation.	63
4.12	The error signal we get from the Iodine lock.	64
4.13	The remained amplitude modulated error signal.	65
4.14	The error signal comparison between the one and double pass AOM configuration in the frequency modulation lock.	66
4.15	The error signal before and after locking for the Yb hollow cathode lamp.	66
4.16	The beam path of the all fiber solution of the 370nm laser system.	67
4.17	The repetition rate and intensity noise eater for the pulse laser.	70
4.18	The imaging simulation of the CVI lens at 370 nm.	71
4.19	The imaging simulation of the Photon Gear large N.A. lens at 370 nm.	72
5.1	The $ n\rangle = 6\rangle$ thermalization under the natural reservoir.	77
5.2	Thermal state preparation of the phonon and measurement results.	78
5.3	The phonon projective measurement.	80
5.4	The adiabatic blue sideband.	81
5.5	The waveforms used to apply the work and the adiabatic transformation.	84
5.6	Test of the rapid adiabatic process.	85
5.7	The dissipated work distribution, the Jarzynski equality and Crooks relation results.	86
6.1	The classical analog of adiabatic shortcut.	90
6.2	The comparison between different transportation schemes.	92
6.3	The illustration for the transitionless transport.	93
6.4	The illustration for the unitarily equivalent transport.	94
6.5	Waveforms and robustness of different order polynomials waveforms.	96

6.6	Waveforms for the Fourier optimization scheme of different order N and their robustness against the trap frequency errors. (a) The maximum amplitude of $f(t)$ increases rapidly with the order N and decreases quickly with the shortcut ratio s . (b) With the same $s = 1$, the robustness would be better for a larger order N . With the same order $N = 3$, the robustness would be better for a larger shortcut ratio s	98
6.7	Phonon excitations in the instantaneous frame during different STA protocols and the robustness against trap frequency errors.	98
A.1	The potential of the blade trap.	107
A.2	The effective potential calculated from the electric field simulated with CPO.	110
A.3	The potential generated by the bias DC on the ground blades.	110
A.4	The potential generated by the micro-motion compensation electrodes.	111
A.5	The codes and results of the final results of the CPO simulation.	112
B.1	The code to calculate the energy levels and the magnetic field strength for the clock qubit.	114
B.2	The energy level and the strength of the magnetic field for the clock qubit.	114
C.1	The Rabi rate dependence on the phonon number.	118
C.2	$\Omega_{n,n+1}$ for different n	119
D.1	RF switch without dead time.	122
D.2	Invar confocal design used for PDH lock and F-P monitor.	122
E.1	The Mathematica code used to get the position of an ion chain.	124
E.2	The Mathematica code used to get the axial frequencies and mode vector of the axial mode of an ion chain.	125
E.3	The Mathematica code used to get the radial frequencies and mode vector of an ion chain.	126

Chapter 1

Introduction

With the development of experimental technology, people are already not just satisfied with understanding the quantum world, but also trying to utilize the quantum nature of small particles to realize something that can not be imagined in the classical world, such as the quantum teleportation[2], quantum computation[3] and quantum simulation[4, 5]. Just like the hydrogen atom is the best platform to explore the quantum theory at first, at the beginning of the experimental quantum era, the crystallized trapped ion is also a good platform to realize some simple quantum machines, which can do something impossible before or save a lot of time compared with the classical machine. After the first 2-qubit gate[6] was proposed in the trapped ion system, the experimental quantum computation becomes popular. The fascinating features of the trapped ion is that it is easy enough to be understood and can be controlled in many ways. As for the DiVincenzo criteria[7], the trapped ion can fulfill all the seven requirements in principle. The remaining thing is to scale the small toy up to a real machine. Along the way to this long term goal, we need to develop new and better ways to control ions in all kinds of degrees of freedom. In this thesis, I will introduce some new control methods we developed and some interesting experiments conducted with them. I hope what we do can contribute to the blooming trapped ion community.

1.1 Quantum control with the trapped ion

The controllability of quantum systems is a fundamental issue concerning whether one can drive a quantum system to a desired state. The classical control maintains or changes the state of a specific system with close or open control loops. For the quantum system, inspired by the classical way, people also developed similar control tools, such as the quantum lock-in amplifier[8]. But when we deal with a trapped ion, we should consider more about the unique quantum features. For example, the quantum measurement is greatly different from the classical measurement and also a quantum system can be in the coherent superposition state. For the trapped ion, we should be able to deal with internal states, external motional states and also the coupling between these two. To finish this job we may need suitable hardwares and softwares. The Paul trap is a good hardware to control the macroscopic motion state of ions. It allows people to see the single atom/ion for the first time, before which the single atom is only a nomenclature in textbooks. In this thesis, I will introduce the blade trap we develop in order to control the macroscopic motional state better. To control the microscopic motional state and the internal states, we also develop several new schemes, which can be seen as the software. These schemes can be in the coherent ways with the unitary evolution of a closed quantum system, or can be in the dissipated ways. We can use the environment as a tool to drive the quantum system, where the environment can be natural or an engineered reservoir. When we drive the quantum state, its time evolution can be in the dynamical ways or the adiabatic ways. Even the adiabatic driving with an engineered reservoir is proposed[9].

To control a quantum system better, for example when we need to do feedback or to get the quantum work like in this thesis, we may need to measure a quantum system to get more information. The von Neumann projective measurement means the measurement projects the initial state to one of the eigenstate of the orthogonal projectors with the corresponding probability. There is also another way called the weak or continuous measurement. The system we are interested in is coupled to another auxiliary system and we apply the projective measurement on the auxiliary system. Every such measurement only gives us parts of the information of the original system. It will not destroy all the superposition or mixing of the original system. These quantum measurements may play an important role in some quantum

control schemes. I mainly do the experiments during the five years as a Ph.D. candidate. So this thesis will not cover all the possible quantum control methods but will mainly show our experiments with some new control schemes realized by us. I will also describe some schemes which I believe can be realized in the trapped ion system. For more background of the quantum control, the reference [10] will be a good choice.

1.2 Thesis organization

In the second chapter, I will first introduce the basic principle and the simulation of the linear Paul trap. How to get the desired vacuum conditions will also be described. Then I will focus on the Yb ion. The cooling, pumping and detecting of the trapped ion with high fidelity are the most basic operations we should realize at first of every project.

In the third chapter, I will introduce the theory of the basic operation to control the quantum system. These operations can be the laser-ion interaction or the time evolution of the ion when it contacts with the environment, no matter natural or engineered.

The fourth chapter will be used to show the important hardware that I have built. It will be helpful to the younger students.

The following two chapters will be about the two published papers. I will try to not just repeat the paper material but add more details, unpublished data and more related concerns.

The final chapter will serve as a conclusion.

Chapter 2

Yb ion and ion trap

“...we never experiment with just one electron or atom or (small) molecule.”

—E. Schrödinger, 1952

2.1 The Paul trap

A charged particle can not be hold by the static electric field. According to the Laplace equation, a 3D potential minimum point should be the position of charges that generate this field. Such point of charges will overlap with the ion that you want to trap. However, the Paul trap allows a charged particle trapped by a radio frequency field[11] in the quadrupole configuration (or even higher order). I have used the four rod and blade trap, both linear Paul trap. So I will only focus on the basic principle and the simulation of this kind of traps. Let us start from the simple four rod trap (see Fig. 2.1). To give an intuitive idea, we start from the instantaneous potential generated by the RF voltage applied on the two rods (see Fig. 2.2). Once it rotates, the time average effect will work as an harmonic potential to trap the ion. Now let us derive the exact formula to describe this pseudo-potential. Firstly, we assume the RF field has no z component and the end cap electrodes are applied with DC voltage U_0 . The ion in the center position will feel the electric potential

$$V(x, y, t) = \frac{V_0}{2} \frac{x^2 - y^2}{R^2} \cos(\Omega t) + \kappa \frac{U_0}{2} \frac{2z^2 - x^2 - y^2}{Z^2}, \quad (2.1)$$

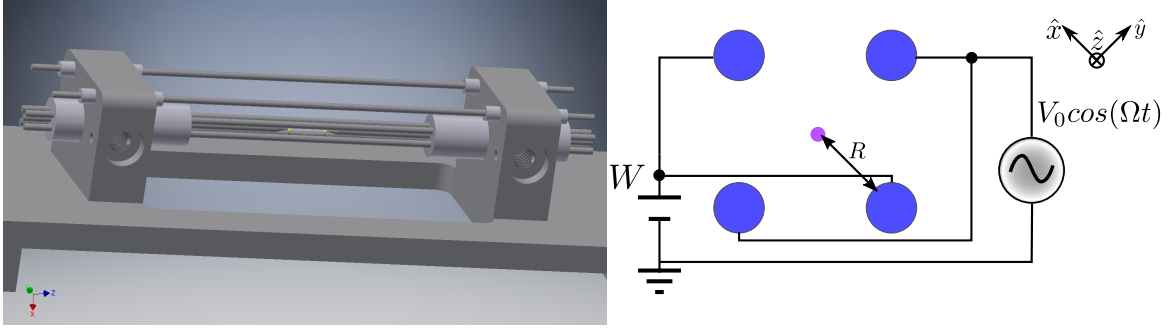


Fig. 2.1 The Four rod trap. The left 3D drawing shows the holder and the micro-motion compensation bars with the four rod trap. In the right drawing, we apply the radio frequency potential $V_0 \cos(\Omega t)$ on two rods and the other two are applied with DC potential W to separate the degenerate two motional modes along the \hat{x} and \hat{y} directions.

where the R is the effective distance from the trap center to the RF rod, Z is the effective distance from the end cap to the center and κ is the geometric factor. This is easy to understand. The center point is the extreme point of the potential. So there should not be the first order term and the leading order should be the second order term. Considering the Laplace equation, the sign before x^2 and y^2 should be opposite and the absolute values should be the same for the RF field. The DC potential from the end caps should be harmonic along the \hat{z} direction at the center and it will push the ion away from the center along the \hat{x} and \hat{y} directions. Considering the symmetrical geometry and the Laplace equation, the sign and absolute values of the coefficients of the second order terms should be as Eq. 2.1. The electric field then should be

$$\mathbf{E}(x, y, z, t) = -V_0 \frac{x\hat{x} - y\hat{y}}{R^2} \cos(\Omega t) - \kappa U_0 \frac{2z\hat{z} - x\hat{x} - y\hat{y}}{Z^2}. \quad (2.2)$$

Here the bias DC on the other two rods are zero. The motion of the ion with charge Q and mass M still obeys the Newton's second law. So we can get the motion equation

$$\ddot{u}_i + [a_i + 2q_i \cos(\Omega t)] \frac{\Omega^2}{4} u_i = 0, \quad (2.3)$$

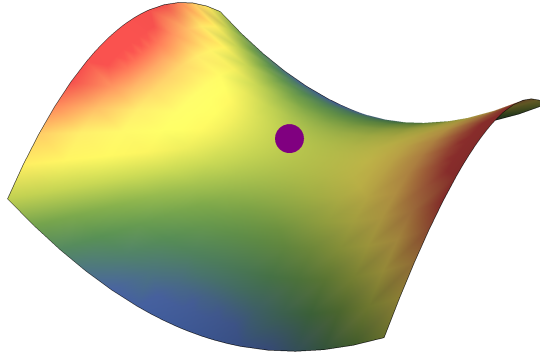


Fig. 2.2 The instantaneous potential in the four rod trap. When it rotates, the ion will be hold at the center position.

where $\mathbf{u} = u_x\hat{x} + u_y\hat{y} + u_z\hat{z}$ is the position of the ion using the coordinate system shown in Fig. 2.1,

$$a_x = a_y = -a_z/2 = -\frac{4\kappa QU_0}{mZ^2\Omega^2}, \quad (2.4)$$

and

$$q_x = -q_y = \frac{2QV_0}{mR^2\Omega^2}, \quad q_z = 0. \quad (2.5)$$

This is the famous Mathieu equation and its solution can be found in Ref. [12]. When $|a_i| \ll 1$ and $|q_i| \ll 1$, its approximate solution up to the first order is

$$u_i(t) = u_{1i} \cos(\omega_i t + \varphi_i) \left[1 + \frac{q_i}{2} \cos(\Omega t) \right], \quad (2.6)$$

where

$$\omega_i = \frac{\Omega}{2} \sqrt{a_i + \frac{1}{2}q_i^2}. \quad (2.7)$$

and the phase φ_i is determined by the initial motional state of the ion. The secular motional frequency ω_i is the important parameter for a trap and the $\cos(\Omega t)$ term is the intrinsic micro-motion.

2.2 CPO simulation

Though we get the analytical formula for the trap, the real situation is highly dependent on the exact geometry condition. To know the exact situation, the first thing when we try to make a new trap is to simulate the trap potential of the exact model. There are several different numerical methods to solve this problem (see Ref. [13]). I choose the boundary element method here. It reduces the complexity a lot and the potential calculated is smoother. We use the CPO¹ program. Its basic operations have been showed step by step in Ref. [14]. However its GUI, model builder and mesh function are really not friendly. So I combine Autodesk Inventor, Comsol and CPO together to simulate the pseudo potential. Firstly, I use the Inventor to build the 3D model of the trap. Here we should build only the surface of the trap and export the model in .stp file or others can be recognized by Comsol. Then I make the mesh on the surfaces with Comsol. It will adjust the size of the mesh according to the importance of the area automatically. We should notice the number of the mesh is limited in CPO. So in Comsol, we should choose the suitable precision. We export these mesh from the Comsol and in the file all the nodes of the mesh are listed. With the suitable program(I use Mathematica here), I can make the file that CPO can use to work. The example code can be found in the Appendix A.

The CPO program can only simulate the potential and field. The pseudo potential can be calculated through the electric field with some approximation. If in the oscillating homogeneous electric field, the ion oscillates around its average position, its motion is described by

$$M\ddot{x} = F_x(t) = eE_0 \cos(\Omega t), \quad (2.8)$$

and

$$x(t) = \bar{x} + \zeta(t) = \bar{x} - \zeta_0 \cos(\Omega t), \quad \bar{x} = constant, \quad \zeta_0 = \frac{eE_0}{M\Omega^2}. \quad (2.9)$$

Here the field strength E_0 is homogeneous. In the quadrupole field, the field $E_0(x(t))$ is however highly inhomogeneous. If we consider the time average effect of the force and do

¹<http://simion.com/cpo/>

the first order approximation

$$\langle eE_0(x(t)) \cos(\Omega t) \rangle \approx e \langle [E_0(\bar{x}) + \frac{\partial E_0(\bar{x})}{\partial \bar{x}} \zeta'] \cos(\Omega t) \rangle = e \frac{\partial E_0(\bar{x})}{\partial \bar{x}} \langle \zeta' \cos(\Omega t) \rangle \quad (2.10)$$

As an approximation we use ζ instead of ζ' :

$$\langle \zeta' \cos(\Omega t) \rangle = -\frac{1}{2} \zeta_0 = -\frac{eE_0(\bar{\zeta})}{2M\Omega^2} \quad (2.11)$$

The force is the deviation of the potential with a negative sign. So from the average force we derive the effective(or pseudo) potential:

$$\psi(\bar{z}) = \frac{eE_0^2(\bar{z})}{4M\Omega^2}. \quad (2.12)$$

Now we see as long as we can get the electric field strength, we get the effective potential.

We can simulate the electric field with CPO program. The detailed code can be found in Appendix. A. After getting the pseudo potential, we can add the potential from the bias DC on the DC blades used to separate the degenerate radial motional level. In the similar way we can also study the effect of the DC on the micro-motion bars and each DC segment on the Blade. By fitting the potential, we can also find all the non-harmonic high order coefficients. In the simulation showed in Fig. 2.3, I use 400V on the RF, 10V for the bias DC and 100V on the micro-motion bar. The position is showed in *mm* and indicates only $0.08\mu\text{m}$ displaced by the micromotion bar. It is too small because of the shielding effect. So I use the bifilar helical resonator and apply the DC directly on the RF blades through suitable filers.

From the simulation results we know to get 2 – 3 MHz we may need several hundreds of Volts on the RF blades. In fact, in our blade trap ($450 \times 550 \mu\text{m}^2$) at 26 MHz driving frequency, to get 3 MHz trap frequency the RF voltage V_0 is about 900 volts, which is measured with the RF pick-up circuit used in the RF power stabilization setup. The commercial RF source even amplified is not enough to get such high voltage. So people use a $\lambda/4$ helical resonator to change a RF power source to a high voltage low current source [15]. We use a bifilar configuration and add the pick-up capacitor for the RF power stabilization. Its loaded Q is

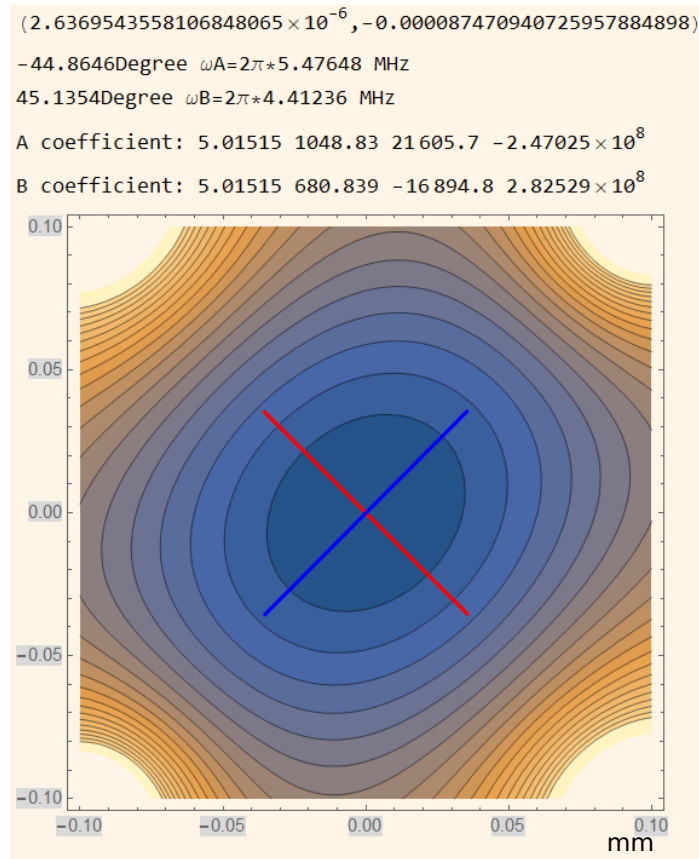


Fig. 2.3 The potential in the center zone of the trap simulated with CPO. The bias DC applied on the DC blades will separate the two degenerate radial motional modes. The ion position and the direction of the mode mode can also be figured out. The detailed code can be found in the Appendix. A. I use 400V on the RF, 10V for the bias DC and 100V on the micro-motion bar. The position is showed in *mm* and is too small. Thus we choose to use the bifilar helical resonator to apply DC on the RF blades through filters.

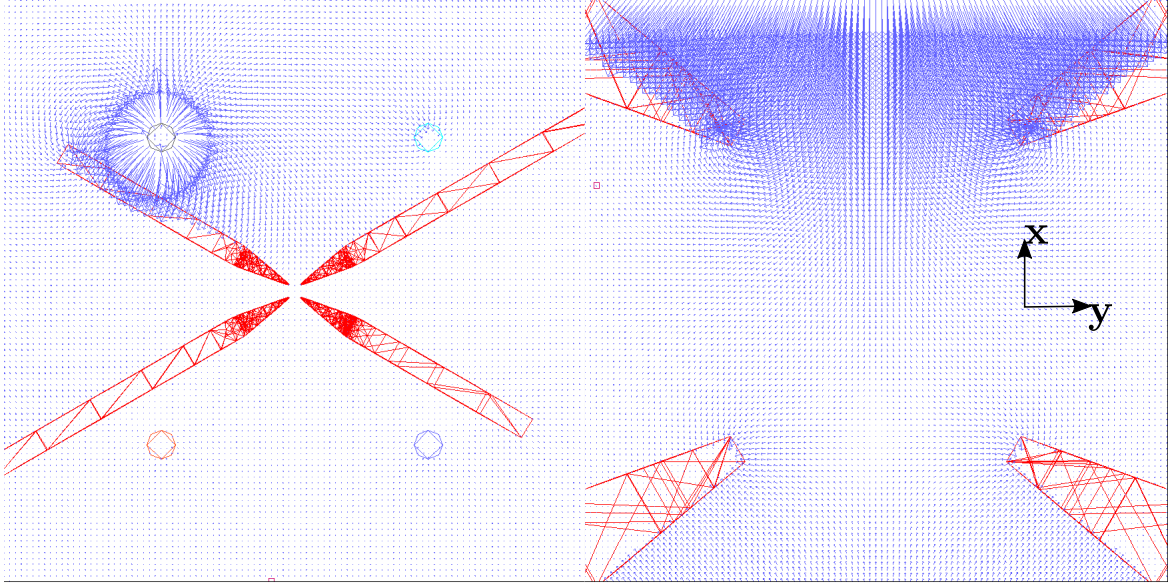


Fig. 2.4 The electric field generated by the micro-motion compensation electrodes. The \mathbf{E} field is modified by the blades and its direction is always along x without any significant y component. We can see the clear shielding effect from the blade.

about 200 after connected with the blade trap. And we can get 3 MHz from 3 W. The bias DC is applied to separate the degenerate radial reap frequencies. In the Simulation, we find the electric field from the micro motion compensation bar will be strongly modified by the blade. In Fig. 2.4, we see the \mathbf{E} field is always along the x direction, though the bar is not place right above the center. Because of the effect of the micro-motion compensation bars are relatively weak, we apply the micro-motion compensation voltages on the DC and RF blades. The details of the helical resonator and the RF power stabilization will be discussed in the fourth chapter.

2.3 Micro-motion compensation

To get a stable and crystalized ion, we should compensate the unwanted DC field \mathbf{E}_{DC} at the RF null. When such field appears, we should rewrite Eq. 2.3 as

$$\ddot{u}_i + [a_i + 2q_i \cos(\Omega t)] \frac{\Omega^2}{4} u_i = \frac{e\mathbf{E}_{DC} \cdot \hat{u}_i}{M}. \quad (2.13)$$

Its solution expanded to the leading order of a_i and q_i is

$$u_i(t) \simeq [u_{0i} + u_{1i} \cos(\omega_i t + \varphi_i)] [1 + \frac{q_i}{2} \cos(\Omega t)], \quad (2.14)$$

where

$$u_{0i} \simeq \frac{e\mathbf{E}_{DC} \cdot \hat{u}_i}{M\omega_i^2}. \quad (2.15)$$

Thus the average position will be displaced by u_{0i} and an excess micro-motion term with the amplitude of $u_{0i}q_i/2$ and the frequency of the trap driving frequency Ω will appear. When it is serious, the laser cooling will be highly affected. To see its effects we follow the treatment in Ref. [16]. When the position of the ion is modulated, the laser field the ion sees will also be modulated with the trap driving frequency Ω . Assuming the laser field with the amplitude \mathbf{E}_0 , frequency ω_{laser} , wave vector \mathbf{k} and phase φ_{laser} in the rest frame of the ion the laser field should be

$$\mathbf{E}(t) = \mathbf{E}_0 \cos[i\mathbf{k} \cdot \mathbf{u} - i\omega_{laser}t + \varphi_{laser}]. \quad (2.16)$$

If the phase of the RF on the two blades are the same, the contribution of the excess micro-motion in the $\mathbf{k} \cdot \mathbf{u}$ is

$$k_i u_{0i} q_i \cos(\Omega t) / 2 = \beta \cos(\Omega t). \quad (2.17)$$

Because it is the power component, we can express the modulation with Bessel functions as

$$\exp[i\beta \cos(\Omega t)] = \sum_{n=-\infty}^{\infty} J_n(\beta) \exp[in(\Omega t + \pi/2)]. \quad (2.18)$$

With the dipole approximation $\langle e | e\mathbf{x} \cdot \mathbf{E} | g \rangle = P|\mathbf{E}|$ and the weak coupling condition $P|\mathbf{E}_0|/\hbar \ll \gamma$, where $|e(g)\rangle$ is the excited(ground) state and γ is the line width of the excited state, we can get the steady solution for the population of the excited state

$$P_e = \left(\frac{P|\mathbf{E}_0|}{\hbar} \right)^2 \sum_{n=-\infty}^{\infty} \frac{J_n^2(\beta)}{(\omega_{atom} - \omega_{laser} + n\Omega)^2 + (\gamma/2)^2}. \quad (2.19)$$

In our trap for Yb ion, $\gamma = 2\pi$ 20MHz and $\Omega = 2\pi$ 26MHz. Then we can plot the P_e as Fig. 2.5. We can see that even the slope can be with a different sign with the normal

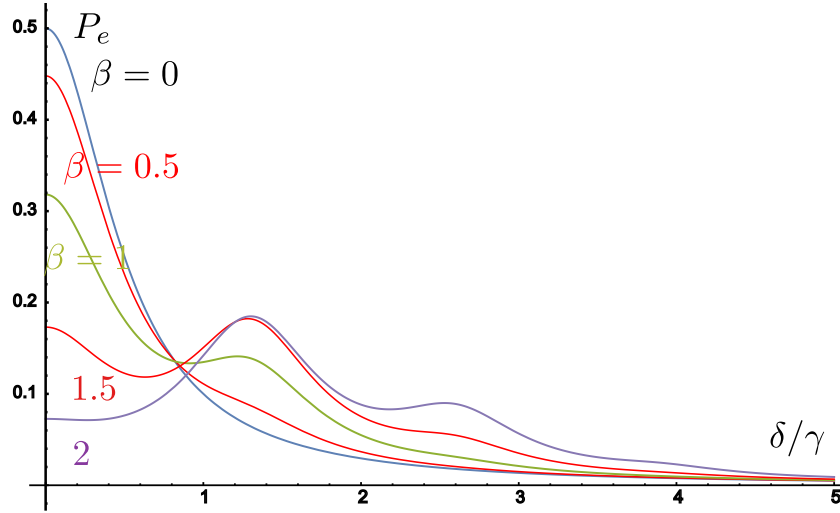


Fig. 2.5 The excited state population for different laser detuning under the influence of micro-motion.

situation ($\beta = 0$). In such situation, the cooling laser will not cool but heat the ion. To reduce the β to 0, we should compensate all the DC field at the RF null. We can use the time-to-amplitude converter (TAC) to do this as described in Ref. [16]. However we have another easier and convenient method that works very well for us. We use only the CCD and the RF power switch in Appendix. D to do this. At high RF power the ion should be closer to the best position. So when we increase the RF power, we should see the ion moves to the best position. Then we can apply the compensation voltage to push the ion to the best position at the lower power situation until the ion position fixes in different RF power. This will work for the DC parallel to the image plane. The DC orthogonal to the image plane can be detected with the count difference of the PMT signal. If the ion is displaced orthogonally to the image plane, the direction of micro-motion should be in the image plane. In our laser configuration, the cooling laser is also in the image plane. So the cooling count will be different for the low and high RF power, if there is DC field orthogonal to the image plane. The two ways should be applied iteratively until both the position and the PMT count keep for the low and high RF power of the trap. In the experiment, we use the two DC blades and one RF blade to realize the micro-motion compensation. Because these blades are just about $300 \mu\text{m}$ to the RF null,

the precision for the DC applied is very high. We make a voltage divider to reduce the DC from the high voltage source by 20 times. Thus the precision is increased by 20 times from the original 0.1 V from the high voltage board.

2.4 Dimension analysis of the background gas collision rate

To trap the ion, just the suitable quadrupole RF field is not enough. We should provide a vacuum environment to avoid the collision between the gas molecular and the trapped ion. Here I will use dimension analysis to solve this collision frequency. Firstly, I find all the physical factors that can affect the collision frequency and their dimensions (Gauss's Unit):

- polarization factor of H_2 α and for convenient I use α/ϵ_0 : $[L]^3$
- ion's charge q and for convenient I use q^2 : $[M][L]^3[T]^{-2}$
- gas pressure p : $[M][L]^{-1}[T]^{-2}$
- gas temperature T and for convenient I use $k_B T$: $[M][L]^2[T]^{-2}$
- mass of H_2 M : $[M]$
- collision frequency f : $[T]^{-1}$

In this process, we assume that the ion is fixed, so its mass will disappear. According to Π theorem, we get 6 quantities and 3 basic dimensions. So we can get 3 non-dimensional parameters, and they can be:

$$\Pi_1 = \frac{p\alpha}{\epsilon_0 k_B T} \quad \Pi_2 = \frac{q^2 \epsilon_0}{M\alpha} f^{-2} \quad \Pi_3 = \frac{p^2 (k_B T)}{M^3 f^6}$$

In order to get the reasonable f , we must consider how these factors affect f : f is bigger when p , α , q^2 get bigger, and f is smaller when M , $k_B T$ get bigger. In this way, we can decide which quantity is the factor of denominator and which is the factor of numerator. After some trials I get the result:

$$f \propto \frac{pq}{k_B T} \sqrt{\frac{\alpha}{M\epsilon_0}}, \quad (2.20)$$

which is derived from $\Pi = \Pi_1^2 \Pi_2$. Up to now we do not have the coefficient. But this is not very important. Because we have gotten the information that f is proportional to p . Under normal operation, we keep the vacuum at $10^{-10} - 10^{-11}$ Torr level and the life time of the bright ion is about several hours. Use this as a standard, we can expect the collision frequency when we improve the vacuum or reduce the temperature. We should notice that the collision does not mean the ion is gone. It may be excited to other meta stable states or forms molecular with H atom. Most times we can recover the dark ion with 638 nm laser (from F states) or the strong 374 nm pulse laser (molecular ion or melted ion). Typically the single ion can stay in the trap for more than one week at 3 MHz, during which the cooling laser is not always on.

2.5 Vapor pressure

To trap the ion, we should firstly make the atom vapor flow in the vacuum. The drawings are listed in Fig. 4.3. Here the vapor pressure calculation is presented here to know the exact temperature we need to generate the atom flow. When the solid Yb becomes vapor, the pressure in side the solid and the vapor should be the same. The pressure of the atom vapor flow is the same as the vacuum pressure inside the chamber. So from the equation related the temperature and the vapor pressure, we can get the temperature we need to generate the Yb atom vapor flow. From the Ref. [17], we know the vapor pressure in general is

$$P(T) = 10^{A - \frac{B}{T} - C \log_{10}(T) - DT^3}. \quad (2.21)$$

From the reference above, we know $A = 11.992$ $B = 8111$ $C = 1.0849$ $D = 0$ for Yb. Here the $P(T)$ is in the unit of Torr and T is the absolute temperature. For 10^{-11} Torr, the temperature should be $130 + 273.15$ K. For 10^{-8} Torr, the temperature should be $200 + 273.15$ K. For 6×10^{-7} Torr, the temperature should be $260 + 273.15$ K. In the baking stage of the vacuum preparation, the temperature is limited within 200 Celsius degrees and the vacuum can reach 4×10^{-8} Torr. Thus the Yb oven is safe when we bake the vacuum chamber. When the atomic oven is tested for the threshold current with the molecular pump,

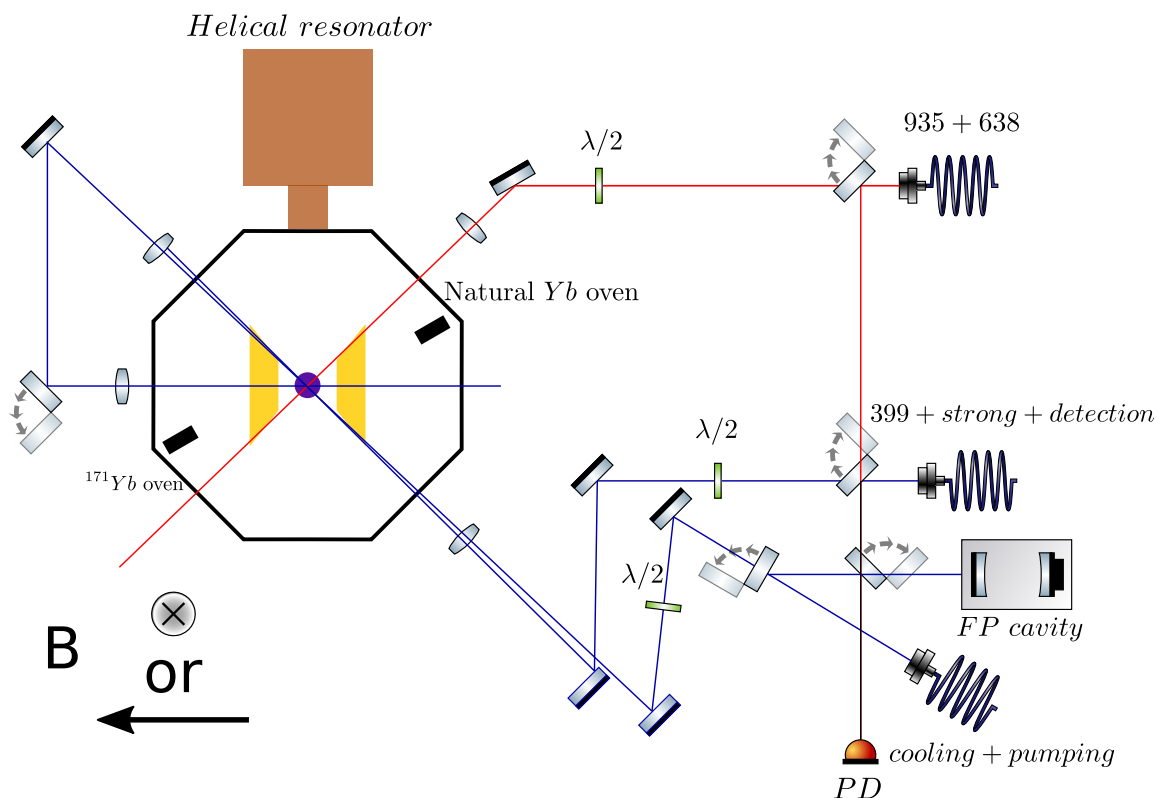


Fig. 2.6 The laser path before the trap for basic operations. We use the polarization maintaining fibers and flipping mirrors to combine several lasers to save the optics for alignment. The magnetic field B can be applied in the vertical or horizontal direction to reduce the probability to realize the coherent population trapping (CPT) in the S levels. Parts of drawings of components are from the Component Library.

the vacuum is about 6×10^{-7} Torr. Thus in the final vacuum of 10^{-11} Torr, we should reduce the current heating the oven tube. It should be half of the tested value as a rule of thumb. More information about the vacuum can be found in the fourth chapter.

2.6 Laser ionization, cooling, pumping and detecting of Yb ion

For different ion species, we may need different lasers to realize all the basic operations. In the case of Yb, we follow the suggested scheme and values as described in Ref. [14] and make some modifications. The laser path before the trap is shown in Fig. 2.6. The ionization

is realized with two-photon process. We firstly excite the Yb atom from the ground state 1S_0 to 1P_1 with 398.9108 nm laser for $^{171}\text{Yb}^+$ and 398.9115 nm laser for $^{174}\text{Yb}^+$ (see Ref. [18] for the energy levels). The second step from 1P_1 to ion state need at least 394.1 nm laser. This can be realized with the strong beam of 369.5 nm or 374 nm pulse laser (not showed in Fig. 2.6). Because the power of the pulse laser is much higher than that of the diode laser, we choose to use the 374 nm pulse laser together with the strong beam for the second step. This pulse laser is used for the Raman transition and coherent control also. The oven should be perpendicular to the ionization laser to reduce the Doppler shift. The abundance of ^{174}Yb is 31.8%. If we use the natural Yb oven, we will get ^{174}Yb with high probability. The abundance of ^{171}Yb is 14.3%. So we need to use the enhanced ^{171}Yb for the oven to load the corresponding ion. Because the 399 nm, the strong beam and the detection beam are combined in one PM fiber, once we get the ion and align the detection beam well, the alignment of the ionization beams are automatically optimized. Thus only a small power of 399 nm (200 μW) focused down to 40 μm with a lens of 150 mm is enough for us.

To cool down the $^{174}\text{Yb}^+$ ion, we use 369.5252 nm cooling laser for $^2S_{1/2}$ to $^2P_{1/2}$ and 935.1802 nm re-pumping laser ($^2P_{1/2}$ has a probability of 0.5% to decay to the meta stable state $^2D_{3/2}$) for $^2D_{3/2}$ to $^3[3/2]_{1/2}$. The wavelength for $^{171}\text{Yb}^+$ are 369.52633 nm and 935.1882 nm. However because of the hyperfine splitting of $^{171}\text{Yb}^+$, we need other frequency added to the cooling laser. The absolute frequency is calibrated with the I_2 vapor saturated absorption spectrum as in Fig.4.12, which will be described in the fourth chapter. The lasers for cooling, pumping and detecting of $^{171}\text{Yb}^+$ is plotted in Fig. 2.7. For the cooling, we add a 14.748 GHz modulation on the 369.5263 nm through the second order sideband of a 7.374 GHz EOM. And the cooling laser is red-detuned by $\Gamma/2 = 2\pi \times 10\text{MHz}$ to achieve the maximum cooling power. For the re-pumping 935 nm laser, for the hyperfine splitting reason we also add a 3.07 GHz modulation through the fiber EOM from EOSPACE. In this way, the closed cycling transition can be used for Doppler cooling. And the ion can be cooled down to the thermal state of $\bar{n} = 10$ average phonon. For the optical pumping, we add a 2.105 GHz modulation through the EOM and only the ground state is not excited. The requirement of the polarization are similar for cooling and pumping but a little different from detecting. That

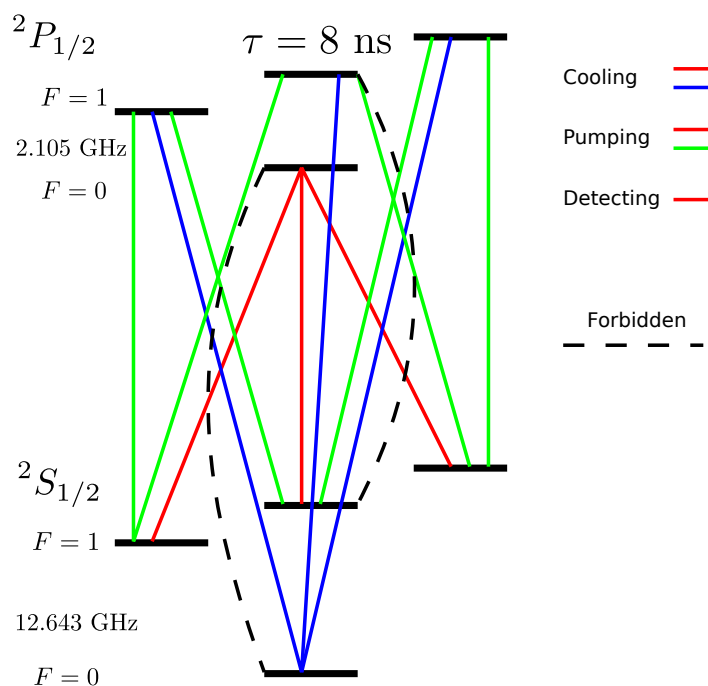


Fig. 2.7 The lasers used for cooling, pumping and detecting of $^{171}\text{Yb}^+$.

is the reason why we combine the cooling and pumping in one PM fiber. The key point for the detecting is the forbidden transitions in Fig. 2.7. In this way, the excited state is included in a closed cycling transition to scatter a lot photons and the ground state is far off-resonant with at least 2.105 GHz.

There is another cooling beam you may already notice. We reuse the cooling beam with a flipping mirror after the laser passing the chamber. When two cooling laser beams overlap at the ion position, the scattering of the ion will decrease, and even the motion of the ion can be modulated. We can see the ion becomes a line not a point. This second cooling along the Raman beam direction is used for the alignment of the Raman beam. It is convenient and quick compared with other methods.

We also use 638 nm laser to re-pump the dark ion from F states, which may be formed when ion collides with the background gas every several hours. We scan its wavelength from 638.6101 – 638.6151 nm. Its alignment is guaranteed by coupled to the fiber for 935 nm laser.

Chapter 3

laser-ion interaction

To control the internal states and the motional states, we can use the resonant microwave for the hyperfine qubit, resonant lasers for the optical qubit and Raman lasers for the hyperfine qubit. Traditionally because of the small Lamb-Dicke parameter, we can not use the microwave field to control the motion. And the individual ion addressing with lasers looks more practical than with microwaves. However the microwave with giant gradients works. Just like the Raman laser scheme, there is also a huge position-dependent energy difference. The entanglement operation (see Ref. [19]) even the single qubit addressing have been realized (see Ref. [20]). I have used only the lasers to realized the coherent control with one ion and will focus on the theoretical background of what I have really realized.

3.1 Coherent control with lasers

The laser is an extremely coherent electromagnetic field. To improve its coherence, we also develop different stabilization schemes, which will be described in the next chapter. Such nature makes lasers suitable for the quantum coherent control. The laser-ion interaction can be in the dipole or quadrupole ways.

3.1.1 Radiation patterns and C.G. coefficients

The radiation pattern shows how the direction, polarization of lasers relate to the interaction strength. Before we build the beam paths, we should consider the relation between the directions of the magnetic field, the laser wave vector and also the polarization. The CG coefficient shows the relative strength and phase for different transitions. It is very important when the coherent interference happens among all the possible transitions.

We define the direction of magnetic \mathbf{B} field is the vertical z axis. For the dipole interaction its radiation pattern looks like Fig. 3.1. The results for the quadrupole transition are also showed in Fig. 3.2. The exact formula can be found in Ref. [21]. In the quadrupole transition, we notice when $\delta m = 0$, the wave vector of lasers should be 45 degree tilted from the magnetic field in order to maximize the strength of the interaction.

To know the relative phase and strength for different transitions, we should know the CG coefficient (see Ref. [22]). For the dipole transition, considering the hyperfine interaction, the angular coupling in the way as

$$\mathbf{L} + \mathbf{S} = \mathbf{J} \quad \mathbf{J} + \mathbf{I} = \mathbf{F}, \quad (3.1)$$

where \mathbf{L} is the orbital angular momentum, \mathbf{S} is the electron spin and \mathbf{I} is the nuclear spin. We use the subscript e and g to denote the excited and ground states of the two level system. Then the C.G. coefficients between the Zeeman levels $|L_e, F_e, m_e\rangle$ and $|L_g, F_g, m_g\rangle$ is

$$CG = (-)^{F_e - M_e + J_e + I + F_g + k + L_e + S + J_g + k} \sqrt{(2J_g + 1)(2F_g + 1)(2L_e + 1)(2J_e + 1)(2F_e + 1)} \\ \begin{pmatrix} F_e & k & F_g \\ -m_e & q & m_g \end{pmatrix} \begin{Bmatrix} J_e & k & J_g \\ F_g & I & F_e \end{Bmatrix} \begin{Bmatrix} L_e & k & L_g \\ J_g & S & J_e \end{Bmatrix}, \quad (3.2)$$

where $k = L_e - L_g = 1$ and $q = m_e - m_g$. As a conclusion, all the possible dipole transitions for $^{171}\text{Yb}^+$ between the $^2S_{1/2}$ and $^2P_{1/2}$ states are showed in Fig. 3.3.

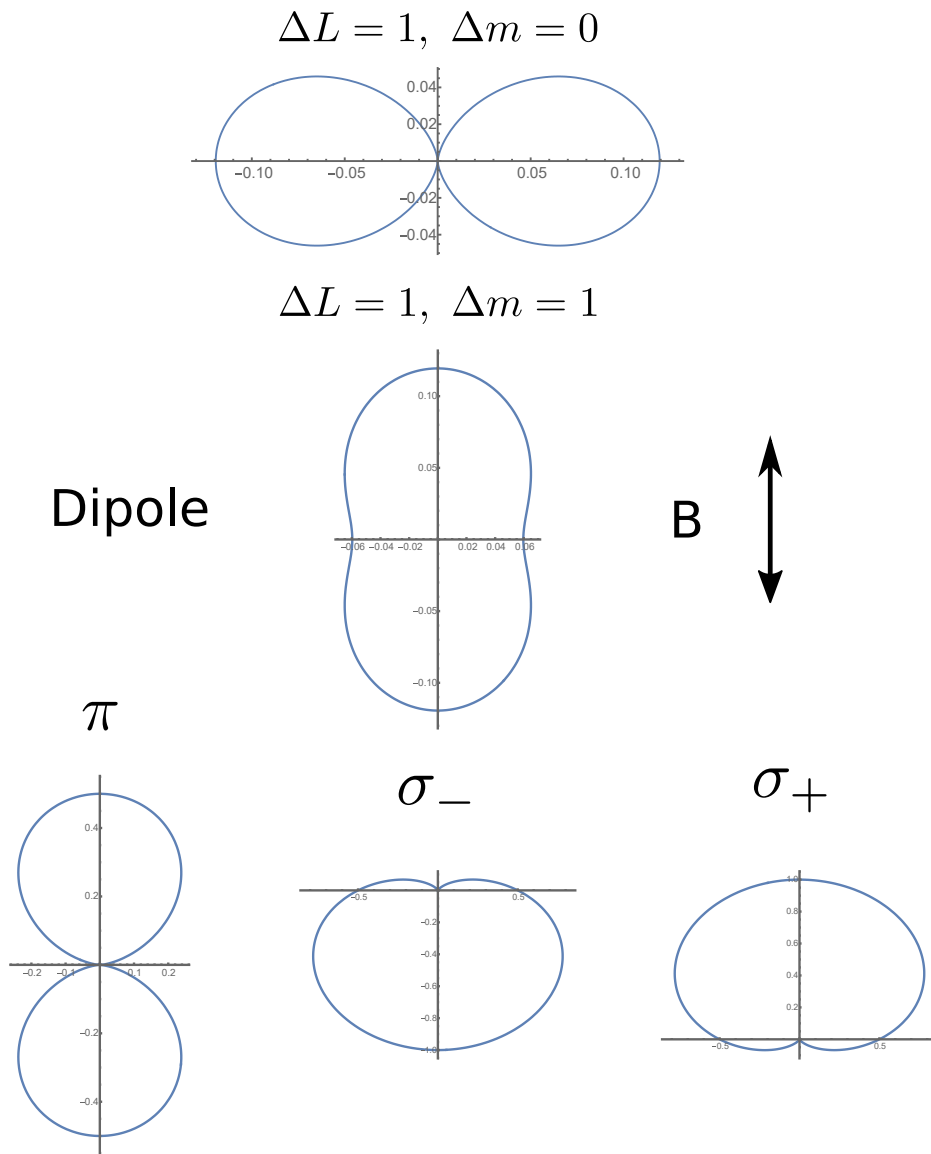


Fig. 3.1 The radiation pattern for the dipole transition. It is homogeneous along the ϕ direction. Here I plot the relative strength along the θ direction. For the $\Delta m = 1$ transition, patterns for different polarization are also listed.

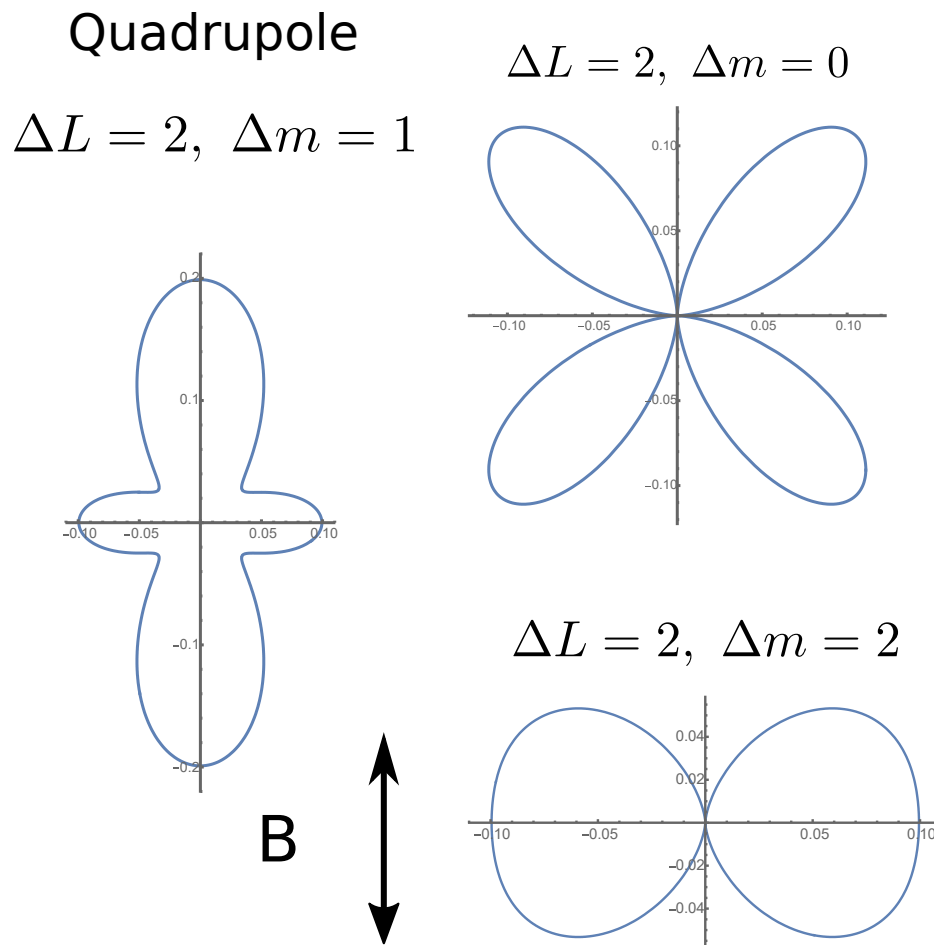


Fig. 3.2 The radiation pattern for the quadrupole transition. It is homogeneous along the ϕ direction. Here I plot the relative strength along the θ direction.

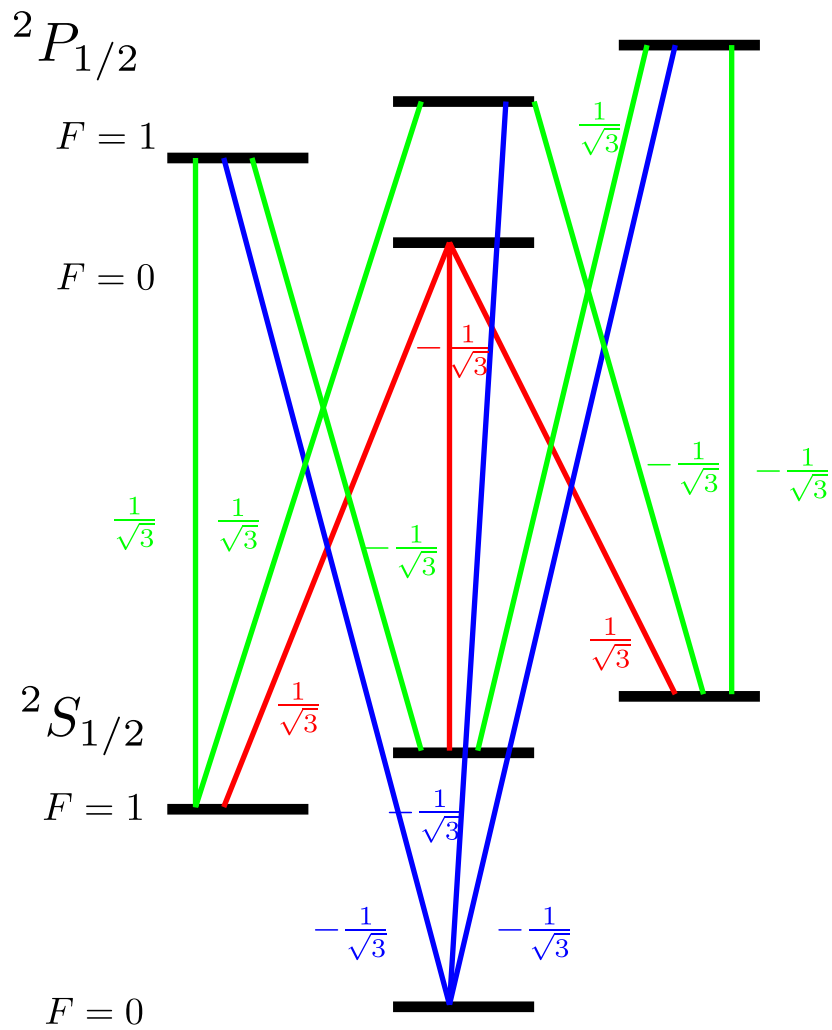


Fig. 3.3 The CG coefficient for dipole transitions between $^2S_{1/2}$ and $^2P_{1/2}$ of $^{171}\text{Yb}^+$.

For the quadrupole transitions, with the similar definition as the dipole transitions, the C.G. coefficient is

$$CG = (-)^{k+L_e+S+J_g+J_e+I-M_e} \sqrt{(2J_g+1)(2F_g+1)(2L_e+1)(2J_e+1)(2F_e+1)} \\ \begin{pmatrix} F_g & k & F_e \\ M_g & q & -M_e \end{pmatrix} \begin{Bmatrix} L_e & J_e & S \\ J_g & L_g & k \end{Bmatrix} \begin{Bmatrix} J_e & F_e & I \\ F_g & J_g & k \end{Bmatrix}, \quad (3.3)$$

where $k = 2$.

3.1.2 One beam Zeeman qubit flipping with pulse lasers

In experiment, we realize the qubit operation with the pulsed Raman lasers. I have used the 355 nm picosecond pulse laser¹ and the 375 nm picosecond pulse laser². In the following, I will only describe the calculation based on the Mira lasers. Though we use the pulse laser, we can still consider the different tooth in the comb as the CW laser for simplicity. For the treatment in the frequency-comb picture, Ref. [23] is a good reference.

Every time when I begin to build the Raman beam paths, I will start from the single beam qubit flipping to reduce the uncertainty. When only one beam works, we do not need to consider the overlap between the two Raman beams and the delay-line. Besides the single beam flipping can be also a good tool to predict the \mathbf{B} field direction.

The repetition rate of the pulse laser is 76.2106 MHz and the hyperfine qubit splitting is 12.643 GHz. Each pair of tooth with 166×76.2106 MHz separation will be only about 8 MHz detuned from the qubit splitting. Such detuning can avoid the one beam flipping when we use the two beam Raman flipping. And this small amount can be covered by the Zeeman splitting, which means if we adjust the \mathbf{B} well (see Fig. 3.4), we should see the transition between the ground state and one of the Zeeman levels in the up states. The \mathbf{B} should be perpendicular to the optical table, the polarization of the pulse laser should be linear and tilts away from the \mathbf{B} field with a suitable angle. Thus both π and $\sigma_+ + \sigma_-$ component exist. From the Fig. 3.4, we know there are two Raman passages. Considering all the related CG

¹from HighQ company

²Verdi-Mira from Coherent company

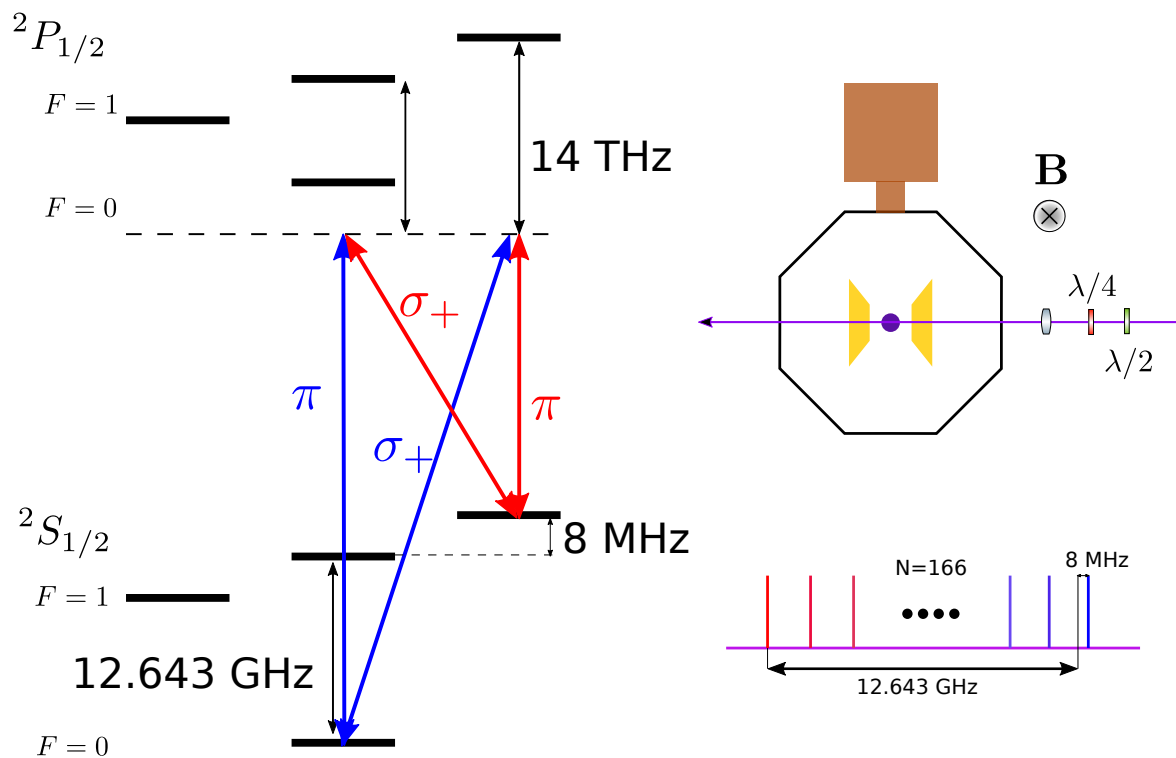


Fig. 3.4 The single beam flipping for the Zeeman qubit. The CG coefficients for all the dipole interactions are $-\frac{1}{\sqrt{3}}$. The two Raman passages will coherently add together.

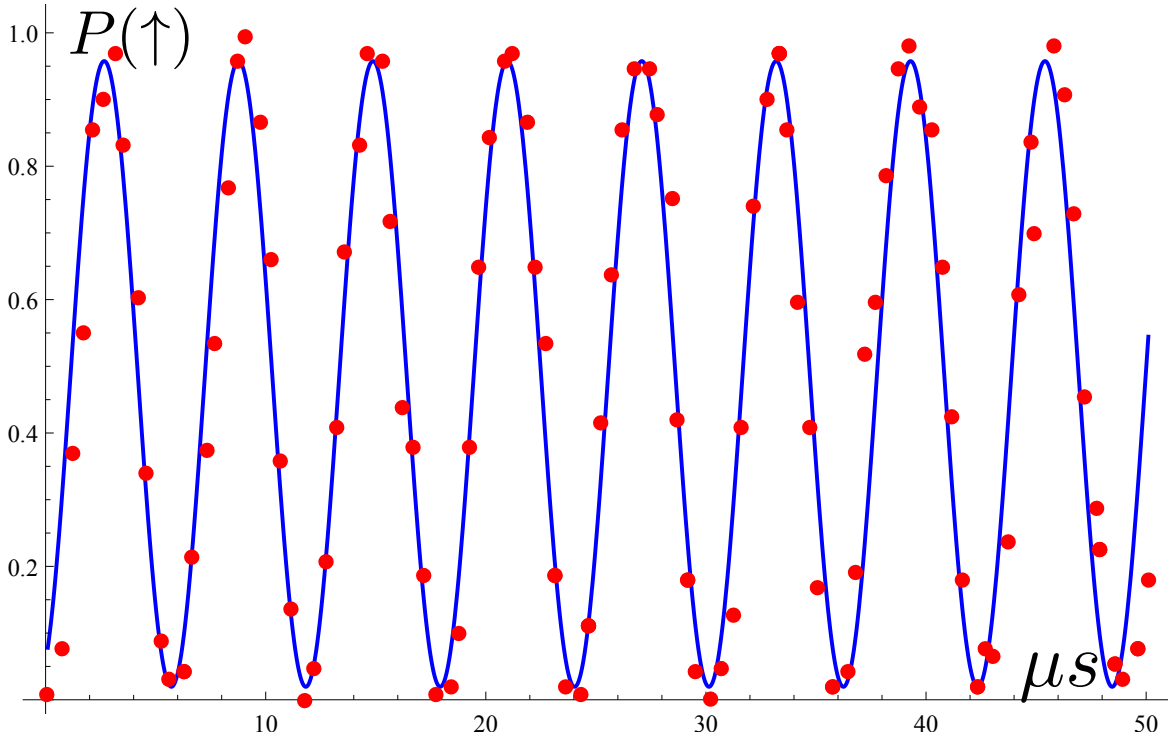


Fig. 3.5 The time evolution of the single beam flipping for the Zeeman qubit.

coefficients are $-\frac{1}{\sqrt{3}}$, they will coherently add. In experiment, after we overlap the pulse laser with the second cooling laser showed in Fig. 2.6 and make sure of the \mathbf{B} and polarization, we keep the pulse laser on and adjust the strength of the \mathbf{B} field. When the Zeeman splitting reach about 8 MHz, we should see the bright count from the PMT. Then we can optimize the alignment, polarization and \mathbf{B} to get the best flipping from one beam as showed in Fig. 3.5. The Lamb-Dicke parameter of the one beam flipping is zero.

Except for the alignment, another advantage of the one beam flipping is that it can help us to adjust the direction of the \mathbf{B} field well. In the Raman configuration, the direction of \mathbf{B} field and the Raman beams should be the same. We can use the one beam flipping as a good reference. After we optimize the one beam configuration, we change the direction of \mathbf{B} field to parallel to the Raman beams. If there is small misalignment, the pulse laser will contain the π component, which will cause the single beam Zeeman qubit flipping. Only when the \mathbf{B} field and the pulse laser are parallel, the pulse laser contains only $\sigma_+ + \sigma_-$. In such situation, we should not see any excitation. By playing with three pairs of \mathbf{B} field coils,

we can align the direction of \mathbf{B} field along the Raman beams with the help of the excitation from one beam of pulse laser.

3.1.3 Two beam Raman qubit flipping

To control the motional states of ions, we use two counter-propagating Raman beams. In this way, the Lamb-Dicke parameter can be maximized. We have tried three different configurations as showed in Figure. 3.6. All of them can realize the qubit flipping. If we want to use the two Raman passages together, the directions of \mathbf{B} and polarizations of Raman beams should be orthogonal to each other. If not, the CG coefficients will give opposite signs for these two Raman passages, and they will cancel out. If we just use one Raman passage, as the last configuration, we can also realize the qubit flipping and also the spin dependent-force or beam splitting operation, where the qubit is not involved. In our final setup, we choose the last configuration.

I will give a simplified calculation of the Raman transition based on the continued wave picture and the effective Hamiltonian theory [24]. The real Hamiltonian for the Raman process is ($\hbar = 1$):

$$H = \frac{\Omega_r}{2} |e\rangle\langle\uparrow| e^{i(\Delta+\delta)t+i\mathbf{k}_r\cdot\mathbf{x}-i\phi_r} + \frac{\Omega_r}{2} |e\rangle\langle\downarrow| e^{i(\Delta+\delta+\omega_{HF})t+i\mathbf{k}_r\cdot\mathbf{x}-i\phi_r} \\ + \frac{\Omega_b}{2} |e\rangle\langle\downarrow| e^{i\Delta t+i\mathbf{k}_b\cdot\mathbf{x}-i\phi_b} + \frac{\Omega_b}{2} |e\rangle\langle\uparrow| e^{i(\Delta-\omega_{HF})t+i\mathbf{k}_b\cdot\mathbf{x}-i\phi_b} + \text{H.c.} \quad (3.4)$$

Using the effective Hamiltonian theory, the frequency and operator for each term is

$$\omega_1 = \Delta - \omega_{HF} \quad \hat{h}_1^\dagger = \frac{\Omega_b}{2} e^{i\mathbf{k}_b\cdot\mathbf{x}-i\phi_b} |e\rangle\langle\uparrow| \quad (3.5)$$

$$\omega_2 = \Delta \quad \hat{h}_2^\dagger = \frac{\Omega_b}{2} e^{i\mathbf{k}_b\cdot\mathbf{x}-i\phi_b} |e\rangle\langle\downarrow| \quad (3.6)$$

$$\omega_3 = \Delta + \delta \quad \hat{h}_3^\dagger = \frac{\Omega_r}{2} e^{i\mathbf{k}_r\cdot\mathbf{x}-i\phi_r} |e\rangle\langle\uparrow| \quad (3.7)$$

$$\omega_4 = \Delta + \delta + \omega_{HF} \quad \hat{h}_4^\dagger = \frac{\Omega_r}{2} e^{i\mathbf{k}_r\cdot\mathbf{x}-i\phi_r} |e\rangle\langle\downarrow| \quad (3.8)$$

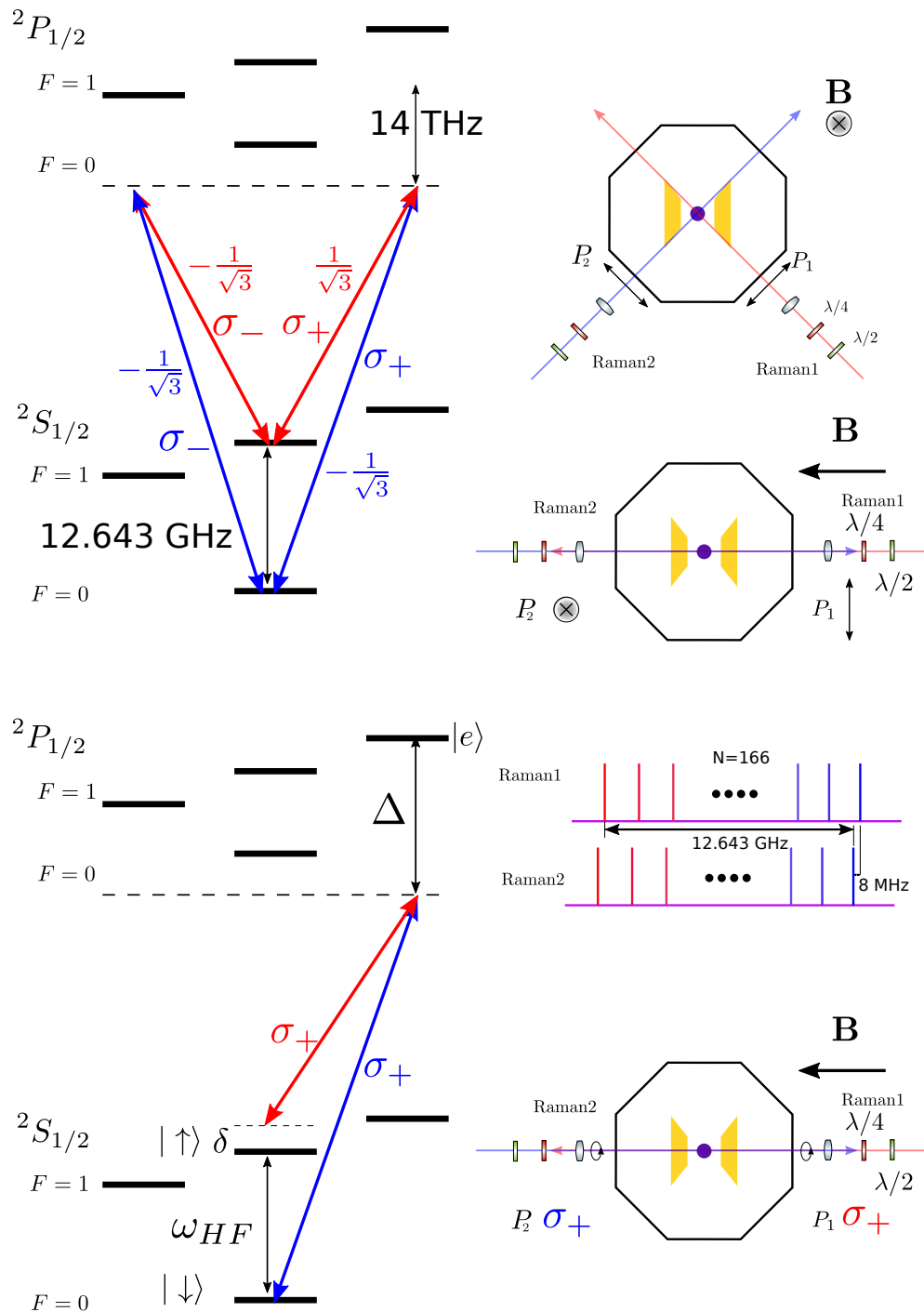


Fig. 3.6 Three different configurations for the Raman transition to control the qubit. From top to bottom, in the top two configuration, we use the two Raman passages. Considering the CG coefficients, we find the **B** and the polarizations of the two beams have to be orthogonal to each other. Otherwise, these two Raman passages will get an opposite signs and cancel out. In the last configuration, we use only one Raman passage by control the polarizations. Later we will see only this configuration allows us to realize the spin-independent force.

The second and the third terms contribute the Raman transition mainly. However, in order to see the whole picture I write down the effective Hamiltonian considering all the terms:

$$\begin{aligned}
H_{eff} = & \frac{1}{4} \left(\frac{|\Omega_b|^2}{\Delta} + \frac{|\Omega_r|^2}{\Delta + \delta + \omega_{HF}} \right) |\downarrow\rangle\langle\downarrow| \\
& + \frac{1}{4} \left(\frac{|\Omega_b|^2}{\Delta - \omega_{HF}} + \frac{|\Omega_r|^2}{\Delta + \delta} \right) |\uparrow\rangle\langle\uparrow| \\
& + \left[\frac{\Omega_b \Omega_r^*}{8} \left(\frac{1}{\Delta} + \frac{1}{\Delta + \delta} \right) |\uparrow\rangle\langle\downarrow| e^{i(\mathbf{k}_b - \mathbf{k}_r) \cdot \mathbf{x} - i\delta t - i(\phi_b - \phi_r)} + \text{H.c.} \right] \quad (3.9)
\end{aligned}$$

where the fast oscillating terms (faster than δ like ω_{HF}) have been ignored and the AC Stark shift of the $|e\rangle$ has been ignored. The differential AC Stark shift reduce the energy gap between $|\uparrow\rangle$ and $|\downarrow\rangle$ as:

$$\Delta_{DAC} = \frac{|\Omega_b|^2}{4} \left(\frac{1}{\Delta - \omega_{HF}} - \frac{1}{\Delta} \right) + \frac{|\Omega_r|^2}{4} \left(\frac{1}{\Delta + \delta} - \frac{1}{\Delta + \delta + \omega_{HF}} \right). \quad (3.10)$$

Normally, $\Delta = 14\text{THz}$ and δ takes the value from 0 to several MHz. We can set $\Omega = \frac{\Omega_r^* \Omega_b}{4} \left(\frac{1}{\Delta} + \frac{1}{\Delta + \delta} \right) \approx \frac{\Omega_b^* \Omega_r}{4} \left(\frac{1}{\Delta} + \frac{1}{\Delta + \delta} \right) \approx \frac{\Omega_b^* \Omega_r}{2\Delta}$, $\Delta \mathbf{k} = \mathbf{k}_b - \mathbf{k}_r$ and $\phi = \phi_b - \phi_r$. After compensating the differential AC Stark shift

$$H_{eff} = \frac{\Omega}{2} |\uparrow\rangle\langle\downarrow| e^{i\Delta \mathbf{k} \cdot \mathbf{x} - i\delta t - i\phi} + \text{H.c.} \quad (3.11)$$

Using the Lamb-Dicke approximation

$$\begin{aligned}
e^{i\Delta \mathbf{k} \cdot \mathbf{x}} &= e^{i(k_x \hat{x} + k_y \hat{y})} \\
&= e^{ik_x x_0 (ae^{-i\omega_x t} + a^\dagger e^{i\omega_x t}) + ik_y y_0 (be^{-i\omega_y t} + b^\dagger e^{i\omega_y t})} \\
&= e^{i\eta_x (ae^{-i\omega_x t} + a^\dagger e^{i\omega_x t}) + i\eta_y (be^{-i\omega_y t} + b^\dagger e^{i\omega_y t})} \\
&= 1 + i\eta_x (ae^{-i\omega_x t} + a^\dagger e^{i\omega_x t}) + i\eta_y (be^{-i\omega_y t} + b^\dagger e^{i\omega_y t}) + \dots \quad (3.12)
\end{aligned}$$

Here we stop to the first order. When $\delta < \Omega \ll \omega_x (\omega_y)$, the interaction is called carrier transition

$$H_{carrier} = \frac{\Omega}{2} \sigma_+ e^{-i\delta t - i\phi} + \text{H.c.}, \quad (3.13)$$

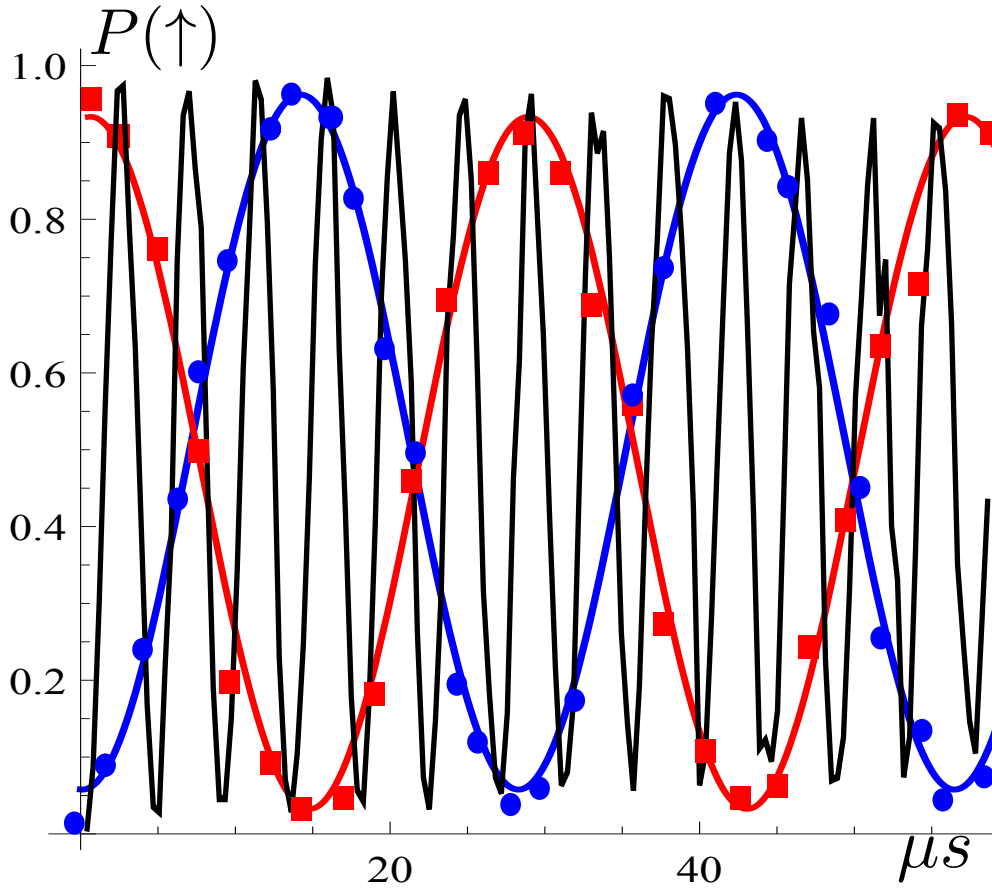


Fig. 3.7 Carrier, blue and red Rabi flipping. Black curve is for carrier. Blue and red curves are the blue and red sideband Rabi flipping.

where $\sigma_- = |\downarrow\rangle\langle\uparrow|$ and the off resonant couplings to the higher order of the motion are neglected. If the off-resonant coupling to the higher order of the motional modes is considered, because it is symmetric about the carrier transition, the AC Stark shift cancels out. When $\delta \approx \omega_x(\omega_y)$, the interaction is called blue-sideband transition for the $x(y)$ motional mode

$$H_{blue} = i\frac{\eta_x\Omega}{2}\sigma_+a^\dagger e^{-i(\delta-\omega_x)t-i\phi} + \text{H.c.} \quad (3.14)$$

When $\delta \approx -\omega_x(-\omega_y)$, the interaction is called red-sideband transition for the $x(y)$ motional mode

$$H_{red} = i\frac{\eta_x\Omega}{2}\sigma_+a e^{-i(\delta+\omega_x)t-i\phi} + \text{H.c.} \quad (3.15)$$

In Fig. 3.7 , we show the experiment data for these three transitions.

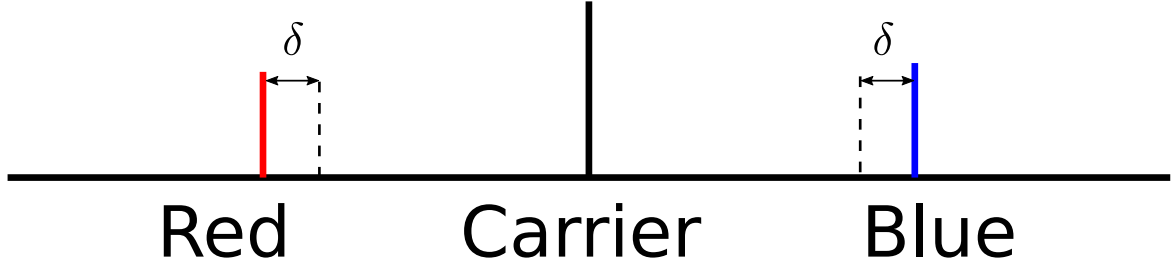


Fig. 3.8 The single beam flipping for the Zeeman qubit. The detuning of the red and blue sideband are the same amount δ but in different direction.

3.1.4 Spin-dependent force

When we apply the detuned red and blue sidebands as showed in Fig. 3.8. The Hamiltonian is

$$\begin{aligned}
 H &= i\frac{\eta_x\Omega}{2}\sigma_+a^\dagger e^{i\delta t-i\phi_b} + i\frac{\eta_x\Omega}{2}\sigma_+ae^{-i\delta t-i\phi_r} + \text{H.c.} \\
 &= -\frac{\eta_x\Omega}{2}\sigma_{\phi_S}(ae^{-i\delta t}e^{i\phi_M} + a^\dagger e^{i\delta t}e^{-i\phi_M}),
 \end{aligned} \tag{3.16}$$

where $\phi_M = \frac{\phi_b - \phi_r}{2}$, $\phi_S = \frac{\pi}{2} + \frac{\phi_b + \phi_r}{2}$ and the spin operator $\sigma_{\phi_S} = \cos\phi_S\sigma_x + \sin\phi_S\sigma_y = e^{-i\phi_S}\sigma_+ + e^{i\phi_S}\sigma_-$. This is the so-called spin dependent force (see more in Ref. [25]). When $\phi_S = \pi$ and $\phi_M = 0$, this is the σ_x dependent force

$$H = \frac{\eta_x\Omega}{2}\sigma_x(ae^{-i\delta t} + a^\dagger e^{i\delta t}). \tag{3.17}$$

If we start from the spin down state, because $|\downarrow\rangle = \frac{1}{\sqrt{2}}(|+_x\rangle + |-_x\rangle)$, the motion will separate to two parts and entangled with the spin states. After $T = \frac{1}{8}$, the two parts will recombine at the original point in the phase space. The radius of the motion is $\frac{\eta_x\Omega}{2\delta}$ [26], and the trajectory in the phase space looks like Fig. 3.9. In experiment we test the duration scan with a fixed δ and also the δ scan with a fixed duration. The results are showed in Fig. 3.10.

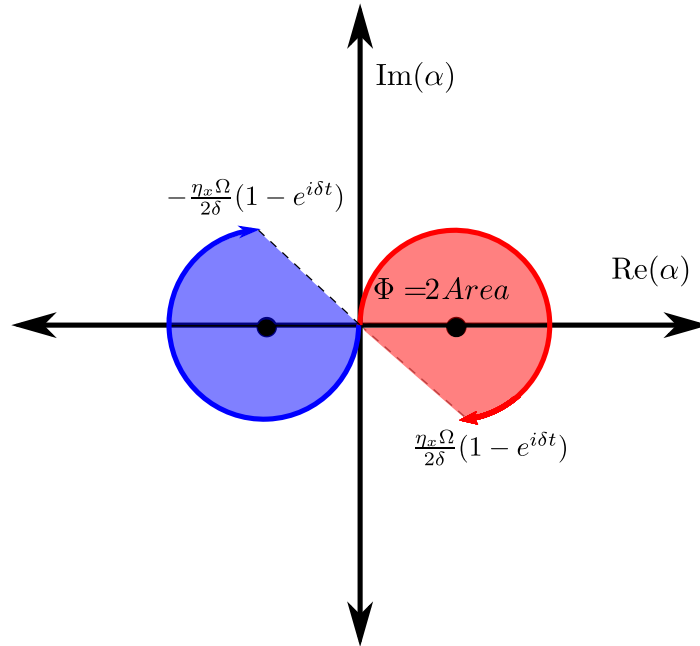


Fig. 3.9 The phase space trajectory of the ion experienced the spin dependent force. The initial state can be decomposed into two parts $|\downarrow\rangle = \frac{1}{\sqrt{2}}(|+_x\rangle + |-_x\rangle)$. Each part will be displaced by the σ_x spin dependent force with opposite directions. The radius of the trajectory is $\frac{\eta_x\Omega}{2\delta}$. The area enclosed by the trajectory is one half of the geometric phase Φ .

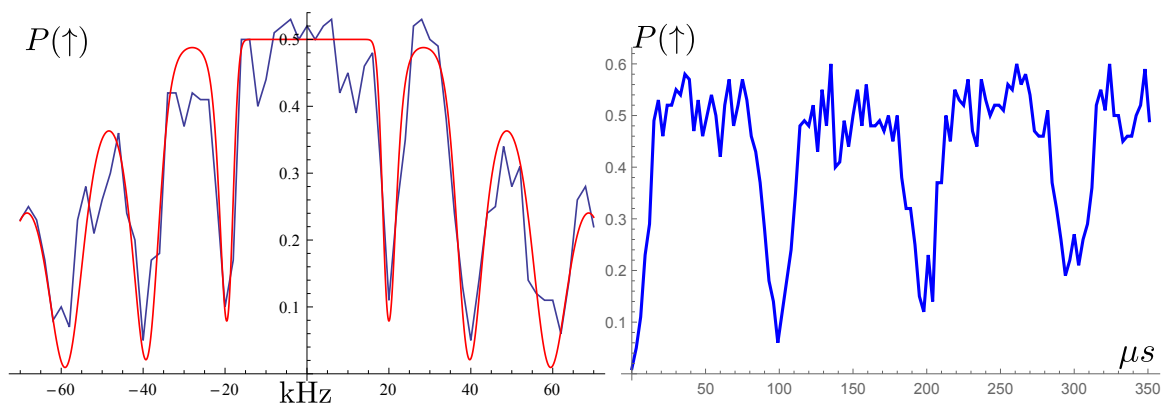


Fig. 3.10 The spin dependent force test data. On the left side we fix the duration to be $50\mu s$ and scan the detuning δ . On the right side, we fix the detuning $\delta = 10\text{kHz}$ and scan the duration. The decay comes from motional heating and decoherence.

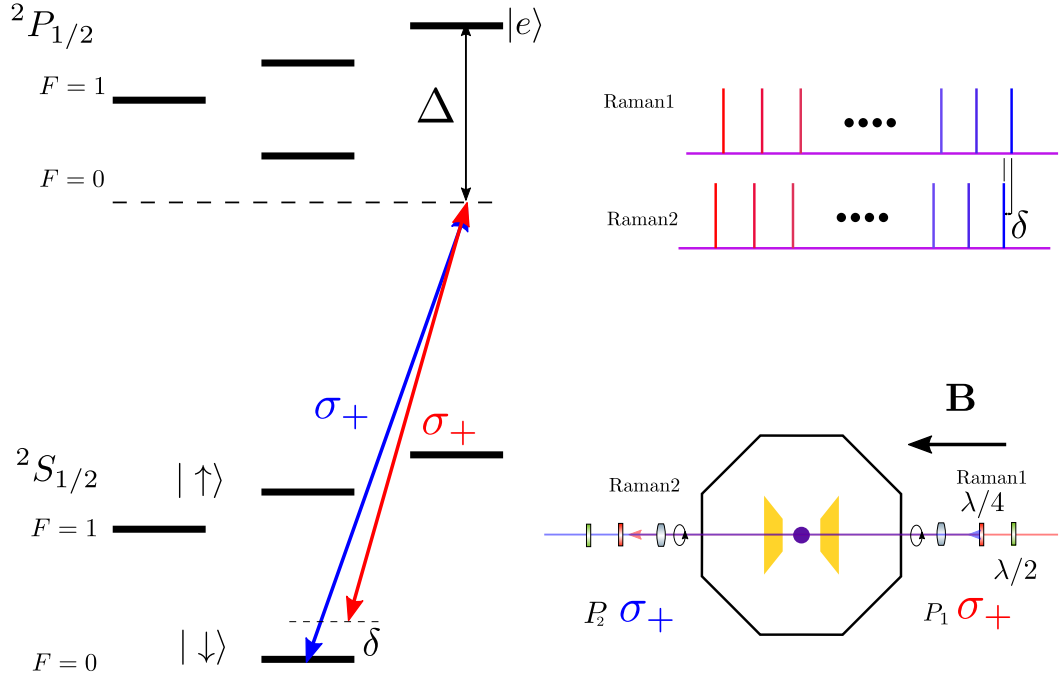


Fig. 3.11 The Spin-independent force scheme. When the detuning between the two Raman beams is close to the frequency of the motional modes, we can manipulate only the motional states and ignore the spin part.

3.1.5 Spin-independent force, squeezing, beam splitting operation and the fidelity measurement.

When the Raman detuning is close to the gap between the motional levels, as showed in Fig. 3.11, we can manipulate only the motional states and ignore the spin part. Still using the effective Hamiltonian method, the off resonant coupling terms are

$$H = \frac{\Omega_r}{2} |\downarrow\rangle\langle e| e^{-i(\Delta+\delta)t - i\mathbf{k}_r \cdot \mathbf{x} + i\phi_r} + \frac{\Omega_b}{2} |\downarrow\rangle\langle e| e^{-i\Delta t - i\mathbf{k}_b \cdot \mathbf{x} + i\phi_b} + \text{H.c.} \quad (3.18)$$

The frequency and operators are

$$\omega_1 = \Delta + \delta \quad \hat{h}_1 = \frac{\Omega_r}{2} |\downarrow\rangle\langle e| e^{-i\mathbf{k}_r \cdot \mathbf{x} + i\phi_r} \quad (3.19)$$

$$\omega_2 = \Delta \quad \hat{h}_2 = \frac{\Omega_b}{2} |\downarrow\rangle\langle e| e^{-i\mathbf{k}_b \cdot \mathbf{x} + i\phi_b}. \quad (3.20)$$

Then the effective Hamiltonian should be

$$H_{eff} = \left(\frac{|\Omega_r|^2}{4(\Delta + \delta)} + \frac{|\Omega_b|^2}{4\Delta} \right) (|e\rangle\langle e| - |\downarrow\rangle\langle\downarrow|) + \left[\frac{\Omega_b^* \Omega_r}{8} \left(\frac{1}{\Delta} + \frac{1}{\Delta + \delta} \right) e^{i\Delta\mathbf{k}\cdot\mathbf{x} - i\delta t - i\phi} (|e\rangle\langle e| - |\downarrow\rangle\langle\downarrow|) + \text{H.c.} \right], \quad (3.21)$$

where $\Delta\mathbf{k} = \mathbf{k}_b - \mathbf{k}_r$ and $\phi = \phi_b - \phi_r$. The first line is the AC Stark shift. When we consider only the $|\downarrow\rangle$, it can be ignored. If we define $\Omega = \frac{|\Omega_b^* \Omega_r|}{2\Delta}$ and the spin is prepared in the spin ground state, the effective Hamiltonian is

$$H_{eff} = -\frac{\Omega}{2} e^{i\Delta\mathbf{k}\cdot\mathbf{x} - i\delta t - i\phi} + \text{H.c.} \quad (3.22)$$

When $\delta \approx \omega_x(\omega_y)$, considering the Eq. 3.12, the effective Hamiltonian can be simplified as the displacement operation

$$H_{dis} = i\frac{\eta_x \Omega}{2} a^\dagger e^{i\nu t - i\phi} + \text{H.c.}, \quad (3.23)$$

where $\nu = \omega_x - \delta$ and the negative sign has been absorbed in ϕ . Applying this Hamiltonian, we can easily displace $\hat{D}(\alpha)$ the ion in the phase space. We show the relationship between the displacement amount and the duration of the interaction as in Fig. 3.12.

When $\delta \approx 2\omega_x(2\omega_y)$, we can expand the Eq. 3.12 to second order terms of $\eta_x(\eta_y)$, the effective Hamiltonian can be simplified as the squeezing operation

$$H_{sqz} = \frac{\eta_x^2 \Omega}{4} a^{\dagger 2} e^{i\mu t - i\phi} + \text{H.c.}, \quad (3.24)$$

where $\mu = 2\omega_x - \delta$. Applying this Hamiltonian, we can easily squeeze $\hat{S}(\mathbf{r})$ the ion in the phase space. The example data is showed in Fig. 3.13.

When $\delta \approx \omega_x - \omega_y(\omega_y - \omega_x)$, we can expand the Eq. 3.12 to second order terms of $\eta_x(\eta_y)$, the effective Hamiltonian can be simplified as the beam splitting operation

$$H_{bs} = \frac{\eta_x \eta_y \Omega}{2} a^\dagger b e^{i\xi t - i\phi} + \text{H.c.}, \quad (3.25)$$

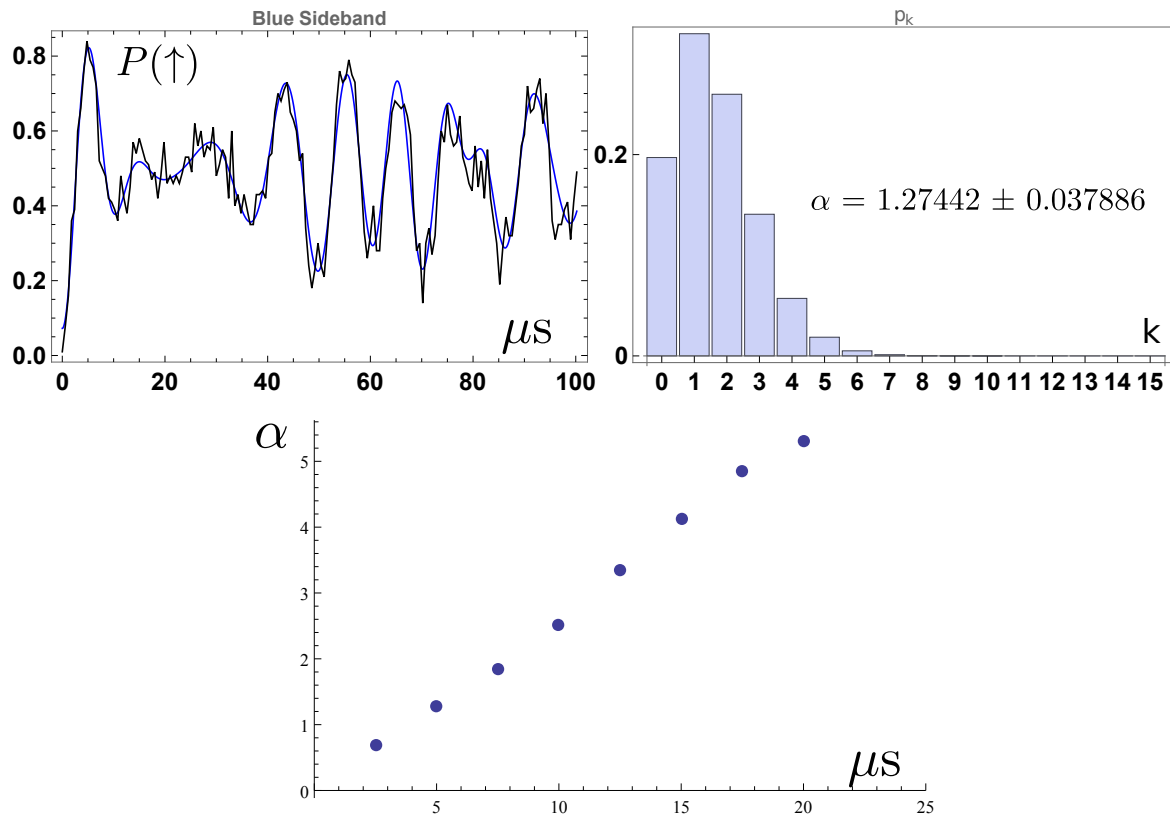


Fig. 3.12 The size of the coherent states dependent on the time. We apply the spin independent force for different duration and measure the final amplitude of the coherent state. The time is in the unit of μs .

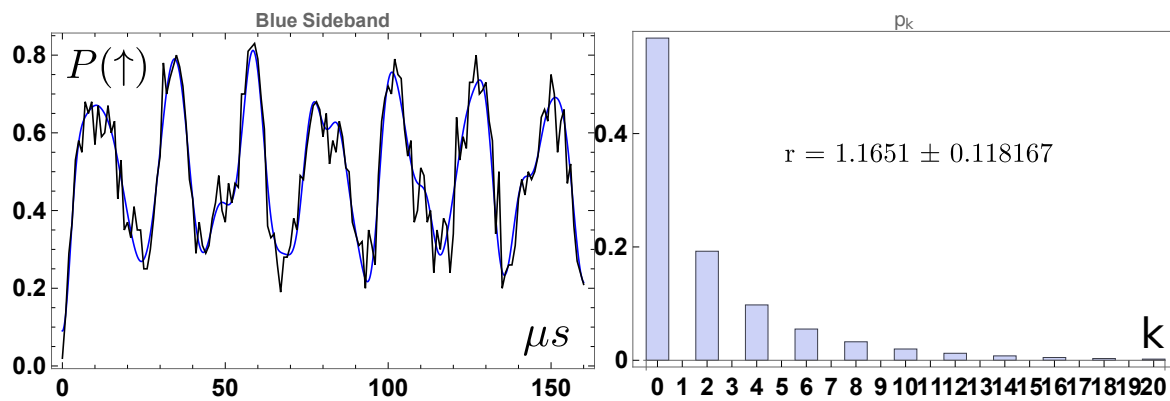


Fig. 3.13 The squeezed state. We apply the spin-independent squeezing operation. After a period, the squeezed state is prepared.

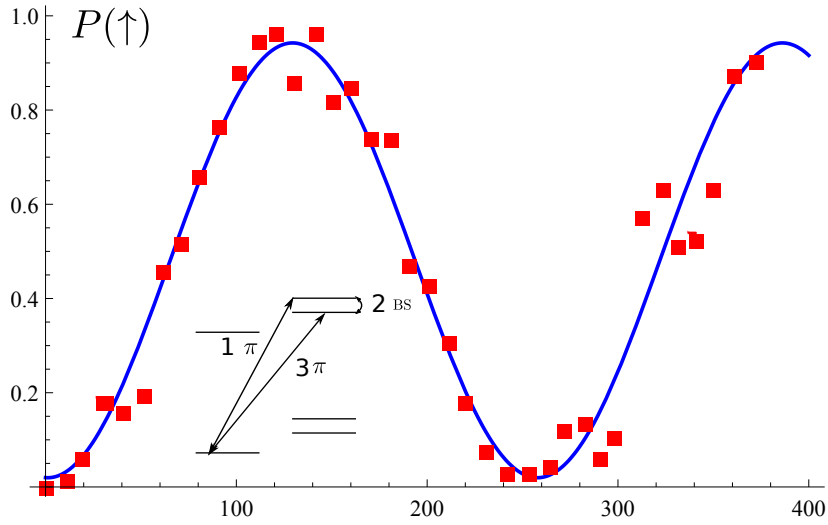


Fig. 3.14 The time scan of the Beam splitting operation. To test the BS operation, we apply the π blue sideband on the X mode. Then we vary the duration of the BS operation. And apply another π blue sideband on the Y mode. The oscillation indicates the population transfer between the two motional modes.

where $\xi = \omega_x - \omega_y - \delta$ and the negative sign has been absorbed in ϕ . Here we show the experiment data on this beam splitting operation between two radius modes in Fig. 3.14.

The fidelity measurement based on the beam splitting operation was proposed by our theory collaborator Professor Myungshik Kim [27]. Here I will show the basic theory. The fidelity between two separable states ρ_1, ρ_2 written with the Wigner distribution is:

$$F = \text{Tr}[\rho_1, \rho_2] = \pi \int d^2\alpha W_1(\alpha) W_2(\alpha) \quad (3.26)$$

$$W_{1(2)}(\alpha) = \frac{1}{\pi^2} \int d^2\lambda C_{1(2)S}(\lambda) e^{\alpha\lambda^* - \alpha^*\lambda}. \quad (3.27)$$

After using the definition of the δ function in the Fourier transformation form, we can get

$$F = \frac{1}{\pi} \int d^2\lambda C_1(\lambda) C_2(-\lambda). \quad (3.28)$$

Then we apply the beam splitting operation as showed in Fig. 3.15. With the definition of the

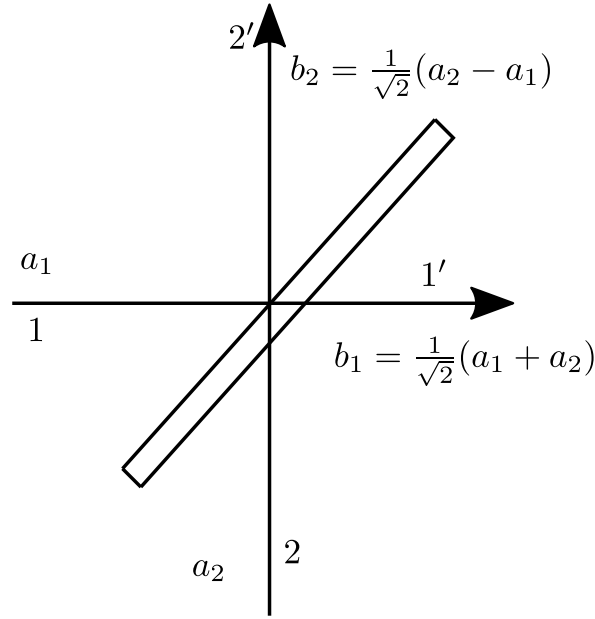


Fig. 3.15 The beam splitting operation.

characteristic function, we can get

$$\begin{aligned}
 C_1(\alpha)C_2(-\alpha) &= \text{Tr}_1[\rho_1 w^{\alpha a_1^\dagger - \alpha^* a_1}] \text{Tr}_1[\rho_2 w^{\alpha a_2^\dagger - \alpha^* a_2}] \\
 &= \text{Tr}_{1,2}[\rho_1 \rho_2 e^{-\sqrt{2}\alpha b_2^\dagger + \sqrt{2}\alpha^\dagger b_2}] \\
 &= \text{Tr}_{2'}[\rho_{2'} e^{-\sqrt{2}\alpha b_2^\dagger + \sqrt{2}\alpha^\dagger b_2}] \\
 &= C_{2'}(-\sqrt{2}\alpha).
 \end{aligned} \tag{3.29}$$

Thus the fidelity is

$$F = \frac{1}{\pi} \int d^2 \alpha C_{2'}(-\sqrt{2}\alpha) = \frac{\pi}{2} W_{2'}(0) = P_{2'} \tag{3.30}$$

This means we just need to measure the parity of the mode 2', we can get the fidelity between the two input states. The two input states can be pure or mixed states but can not be entangled.

3.1.6 Mølmer-Sørensen gate and XY model

When more than one ion is considered, the more interesting multi-body interaction will appear. As the first example, we consider the famous Mølmer-Sørensen gate [28]. When we apply the spin dependent force for N ions, considering Eq. 3.17, we can write down the

Hamiltonian as

$$H = \sum_{i=1}^N \sum_{m=1}^{2N} \frac{\eta_{i,m}\Omega_i}{2} \sigma_x^i (a_m e^{-i\delta_m t} + a_m^\dagger e^{i\delta_m t}), \quad (3.31)$$

where m is used to indicate the different motional modes. Here we use only the radius modes and each ion will contribute two radius modes. The frequency and the operators are

$$\omega_m = \delta_m \quad \hat{h}_m = \sum_{i=1}^N \frac{\eta_{i,m}\Omega_i}{2} \sigma_x^i a_m. \quad (3.32)$$

Applying the effective Hamiltonian theory, we get

$$H_{eff} = \sum_{i \neq j}^N \left(\sum_{m=1}^{2N} \frac{\eta_{i,m}\eta_{j,m}\Omega_i^*\Omega_j}{4\delta_m} \right) \sigma_x^i \sigma_x^j. \quad (3.33)$$

If we include the contribution from the counter-rotating terms and the Raman detuning relative to the carrier transition is redefined as δ ($\delta_m = \omega_m - \delta$), keeping the phase as above, the off resonant coupling is

$$H = \sum_{i=1}^N \sum_{m=1}^{2N} \frac{\eta_{i,m}\Omega_i}{2} \sigma_x^i (a_m e^{-i(\omega_m-\delta)t} + a_m^\dagger e^{i(\omega_m-\delta)t} + a_m e^{-i(\omega_m+\delta)t} + a_m^\dagger e^{i(\omega_m+\delta)t}). \quad (3.34)$$

The effective Hamiltonian is

$$H_{eff} = \sum_{i \neq j}^N \left(\sum_{m=1}^{2N} \frac{\eta_{i,m}\eta_{j,m}\Omega_i^*\Omega_j\omega_m}{2(\omega_m^2 - \delta^2)} \right) \sigma_x^i \sigma_x^j. \quad (3.35)$$

Here we do not include the off-resonant coupling to the carrier transition. The AC Stark shift caused by the two off resonant blue and red sideband will cancel out.

Now we consider a situation that only the off resonant blue (or red) sideband is applied. Considering counter-rotating terms and the coupling to the carrier transition, the Hamiltonian is

$$H = \sum_{i=1}^N \sum_{m=1}^{2N} i \frac{\eta_{i,m}\Omega_i}{2} \sigma_+^i \left(a_m e^{-i(\omega_m+\delta)t-i\phi_b} + a_m^\dagger e^{i(\omega_m-\delta)t-i\phi_b} \right) + \sum_{i=1}^N \frac{\Omega_i}{2} \sigma_+^i e^{-i\delta t-i\phi_b} + \text{H.c.} \quad (3.36)$$

The frequency and the operator in the effective Hamiltonian theory are:

$$\omega_1 = \omega_m - \delta \quad \hat{h}_1 = -i \sum_{i=1}^N \frac{\eta_{i,m} \Omega_i^*}{2} \sigma_{-a_m}^i e^{i\phi_b} \quad (3.37)$$

$$\omega_2 = \delta \quad \hat{h}_3 = \sum_i^N \frac{\Omega_i}{2} \sigma_+^i e^{-i\phi_b} \quad (3.38)$$

$$\omega_3 = \omega_m + \delta \quad \hat{h}_3 = i \sum_{i=1}^N \frac{\eta_{i,m} \Omega_i}{2} \sigma_{+a_m}^i e^{-i\phi_b}. \quad (3.39)$$

The effective Hamiltonian is

$$\begin{aligned} H_{eff} = & \sum_{i \neq j}^N \left(\sum_{m=1}^{2N} \frac{-\eta_{i,m} \eta_{j,m} \Omega_i \Omega_j^* \omega_m}{2(\omega_m^2 - \delta^2)} \right) \sigma_+^i \sigma_-^j \\ & + \sum_{i=1}^N \left(\sum_{m=1}^{2N} \frac{\eta_{i,m}^2 |\Omega_i|^2 \delta}{2(\omega_m^2 - \delta^2)} (n_m + \frac{1}{2}) \right) \sigma_z^i + \sum_{i=1}^N -\frac{|\Omega_i|^2}{4\delta} \sigma_z^i. \end{aligned} \quad (3.40)$$

The $\sum_{i=1}^N \sigma_z^i$ operator commutes with the spin exchange operator $\sum_{i \neq j}^N \sigma_+^i \sigma_-^j$. So the last two terms can be ignored. This is just the Hamiltonian for the XY model. The Ref. [29] has realized this scheme for the spin-1 system. And in Ref. [30, 31], the XY Hamiltonian is realized by increasing the strength of the effective \mathbf{B} field. Under the strong effective magnetic field only the energy conserved terms (the spin exchange terms) remain. Here we proposed a different and easier ways to get the XY Hamiltonian.

3.1.7 A multi-species entanglement scheme

After the first entanglement scheme, the Cirac-Zoller gate proposed, many other methods appear, such as the M.S. gate described above and also the geometric phase gate. Even the reservoir gate has been realized [32, 33]. Here I will give a new and relatively easy scheme to entangle two ions.

1. Start from the ground state of spins and motions for two ions: $|\downarrow\downarrow 0\rangle$.
2. Apply the blue sideband $\pi/2$ pulse on the first ion. The state will be: $\frac{1}{\sqrt{2}}(|\downarrow\downarrow 0\rangle + |\uparrow\downarrow 1\rangle)$.
3. Apply the red sideband π pulse on the second ion. The state will be: $\frac{1}{\sqrt{2}}(|\downarrow\downarrow\rangle + |\uparrow\uparrow\rangle)|0\rangle$.

Only two resonant sideband pulses are enough to entangle two spins. For one specie, we need the single ion addressing ability. For different kinds of ions, we automatically has such ability.

3.1.8 The mode of a chain of mixed ions

One important thing missed in the above discussion is the Lamb-Dicke parameter for the i th ion and the m th motional mode. Here I will simply give the code that can be used to calculate the position, the motional frequency and the mode vector of a ion chain contained different kind of ions following the treatment described in Ref. [34, 35]. As the first step, we should know the position of a mixed ion chain. The position should not be affected by the mass of ions. The interaction between the ions and between the ion and DC field is mass independent. To calculate the position, we should minimize the total energy of the ion chain, where the positions are used as the variables. For an ion chain containing $^{171}\text{Yb}^+$, $^{171}\text{Yb}^+$, $^{137}\text{Ba}^+$ in a series. The position in an example calculation is showed in Fig. 3.16. The next step is to get the axial motional frequencies. In the Lagrangian describing the axial motion, we can get the coupling efficiencies for all the displacements for any two pairs or with itself. It can be written as a matrix. To get the normal mode, we need to diagonalize this matrix. Using the diagonalized results, we can write the Hamiltonian in the decoupled oscillator forms. The eigen vector is the normal mode and the eigen values are the axial motional frequency of the normal mode. Here for different mass of ions, it is convenient to use the mass-weighted coordinates [36]. So after this calculation, we should remember to change back to the real coordinates.

In the similar way, for the radial mode we should firstly get its Lagrangian. It contains two parts. The first is the radial interaction caused by the DC along axial direction. Because of the Laplace equation, in the 3-D potential, the radial part should be $-1/2$ of the axial part. So we can get this part of the radial Lagrangian easily from the matrix we get for the axial motion. The other part of the radial Lagrangian is the interaction caused by the RF applied on the RF electrodes. It is homogeneous for all ions and only contribute to the diagonal parts of the potential. By diagonalize this matrix, we can get the eigen frequencies of the

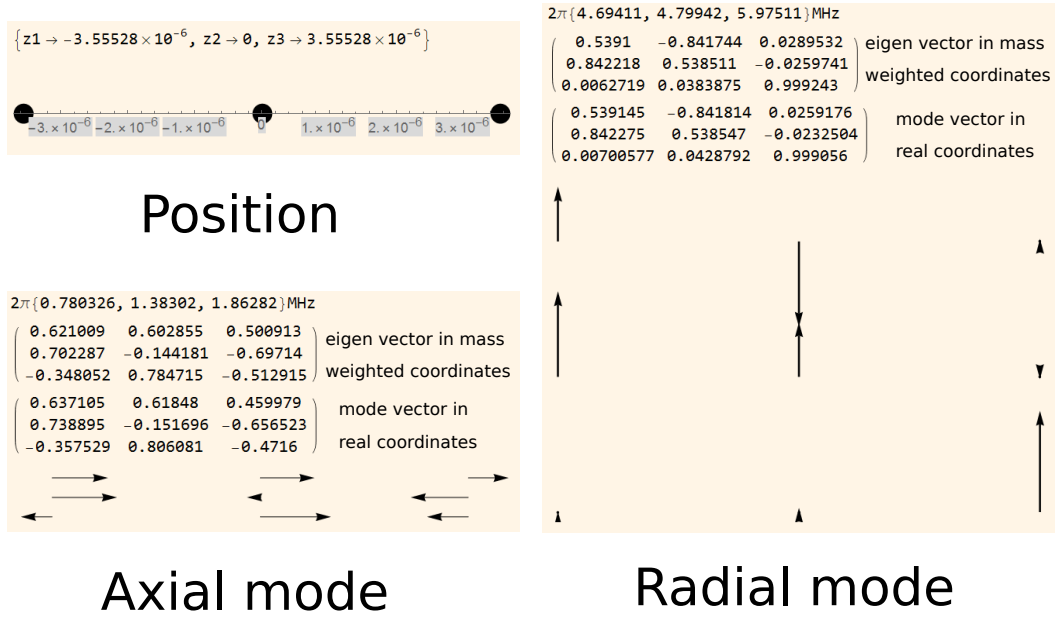


Fig. 3.16 The position and mode structure of a mixed ion chain. We simulate for $\{^{171}\text{Yb}^+, ^{171}\text{Yb}^+, ^{137}\text{Ba}^+\}$. In the simulation we use the mass-weighted coordinates. So after the diagonalize the potential, we should transform the eigen vector to the real coordinate to get the right normal mode vectors.

radial motion. After transform the eigen vector in mass-weighted coordinates back to the real coordinates, we can get the normal mode vectors. The example Mathematica code is showed in Appendix.E.

3.2 Quantum control in the dissipated way

In the above section we have described the basic unitary operation in our trapped ion system. Following, I will describe the basic non-unitary operation in our system. The trapped ion is well isolated system from the environment. However, nothing is perfect in reality. In the coupled whole system, the evolution is still unitary. If we focus only on the sub system, its evolution can be non-unitary. I will start from the natural reservoir then the engineered one.

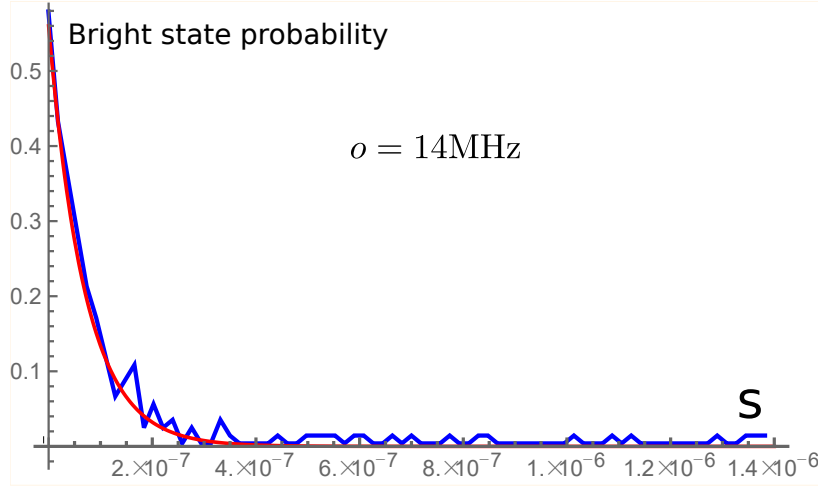


Fig. 3.17 The optical pumping speed. At $3\mu\text{s}$, the state is about 0.023. By fitting the decay, we get the pumping strength $o = 1.42857 \times 10^7$.

3.2.1 Natural reservoir

The first example is the optical pumping or spontaneous emission process. According to the general reservoir theory [37], the system-environment coupling can be written as

$$V(t) = \sum_{\mathbf{k}} g_{\mathbf{k}} \left(b_{\mathbf{k}}^{\dagger} \sigma_{-} e^{-i(\omega - \nu_{\mathbf{k}})t} + b_{\mathbf{k}} \sigma_{+} e^{i(\omega - \nu_{\mathbf{k}})t} \right). \quad (3.41)$$

The $g_{\mathbf{k}}$ is the mode distribution of the reservoir, $b_{\mathbf{k}}$ and $\nu_{\mathbf{k}}$ are the ladder operator and frequency of the mode \mathbf{k} , σ_{-} is for the sin two level system and ω is the energy difference of the two levels. For the optical pumping process, the reservoir can be regarded as the zero temperature thermal reservoir. Thus only $\langle b_{\mathbf{k}} b_{\mathbf{k}}^{\dagger} \rangle = 1$ and all the other correlation is zero. According to the general reservoir theory and use the Weisskopf-Wigner theory of spontaneous emission, the evolution of the system is described by

$$\dot{\rho} = -\frac{o}{2} (\sigma_{+} \sigma_{-} \rho - 2\sigma_{-} \rho \sigma_{+} + \rho \sigma_{+} \sigma_{-}). \quad (3.42)$$

To get the pumping strength o in experiment, we can be fitted through the real data as in Fig. 3.17.

This pumping process is very important in the engineered reservoir. Its strength o is very important to design a good reservoir as described in the next subsection.

The second natural reservoir we encounter in the experiment is the heating reservoir. The stray electrical field keeps kicking the ion. Such coupling to the environment can be described by the boson exchange of the phonon of the ion and the mode of the environment

$$V(t) = \sum_{\mathbf{k}} g_{\mathbf{k}} \left(b_{\mathbf{k}}^{\dagger} a e^{-i(v-v_{\mathbf{k}})t} + a_{\mathbf{k}}^{\dagger} b e^{i(v-v_{\mathbf{k}})t} \right), \quad (3.43)$$

where a and b are the ladder operator of the system and the environment respectively and v and $v_{\mathbf{k}}$ are the energy of the phonon and the mode of the environment respectively. In the same way as described above and assume the thermal reservoir with average occupation \bar{n} , we can get the master equation

$$\dot{\rho}(t) = \frac{\gamma}{2} \bar{n} \left(2\hat{a}^{\dagger} \rho(t) \hat{a} - \rho(t) \hat{a} \hat{a}^{\dagger} - \hat{a} \hat{a}^{\dagger} \rho(t) \right) + \frac{\gamma}{2} (\bar{n} + 1) \left(2\hat{a} \rho(t) \hat{a}^{\dagger} - \rho(t) \hat{a}^{\dagger} \hat{a} - \hat{a}^{\dagger} \hat{a} \rho(t) \right), \quad (3.44)$$

where γ is used to denote the strength of the heating. The lower γ the better will it be for the quantum operation. In experiment, we should measuring the heating rate of each new trap. The heating rate is believe to be proportional to the Negative fourth power of the ion-electrode distance and is strongly affected by the surface quality of the electrodes [38, 39]. Here we show the experiment heating rate data for the five segmented blade trap in Fig. 3.18. It is gold coated and the center zone is $450 \times 550 \mu m^2$.

Another natural reservoir, we see is the motional dephasing reservoir. It is caused by the amplitude fluctuation of the RF driving for the trap. The interaction can be a random Hamiltonian

$$V(t) = \sigma(t)n, \quad (3.45)$$

where $\langle \sigma(t) \rangle = 0$ is the fluctuation of the motional energy level and its width is $\langle \sigma(t)^2 \rangle$. We can directly get the master equation

$$\dot{\rho}(t) = -\Gamma(n.n.\rho(t) - 2n.\rho(t).n + \rho(t).n.n), \quad (3.46)$$

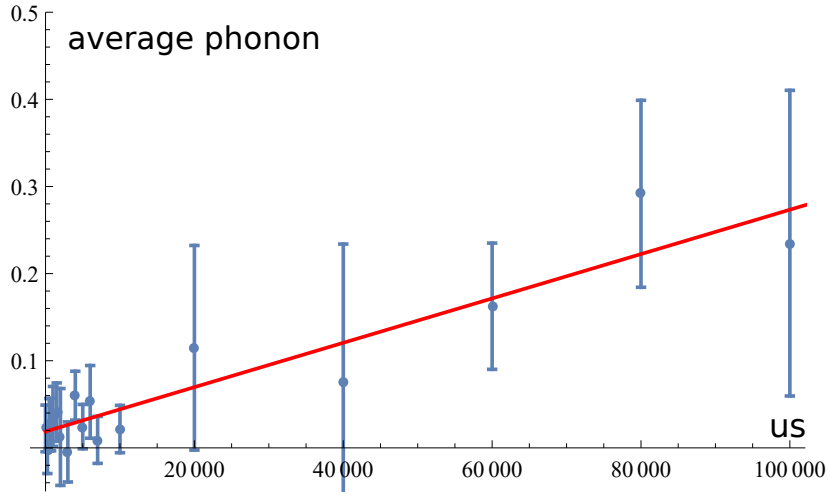


Fig. 3.18 The heating rate measurement of the blade trap. The heating rate $\gamma \approx 3$ phonon/s.

where $\Gamma = \langle \sigma^2 \rangle$ is the strength of the motional decoherence. We can measure the e^{-1} time of the Ramsey decay between the $n = 0$ and $n = 1$ motional states and it is just $\frac{1}{\Gamma}$. To reduce such noise, we stabilize the RF power after the helical resonator. It will be described in the next chapter.

3.2.2 Engineered reservoir

The reservoir is not always bad for the experiment. It can also be used to prepare the useful state [40, 41]. In this section, I will introduce the idea to prepare the coherent state, the squeezed state, the cat state and also the time dependent reservoir for gate operation.

As the first step, an intuitive illustration from the view of coherent population trapping(CPT) is give in Fig. 3.19. For the coherent state reservoir, we apply red sideband, the carrier transition and the optical pumping together. The red and carrier will form a small CPT structure as showed in Fig. 3.19. The ratio c_{n+1}/c_n in the dark state is the ratio between the carrier and red multiplied by the squared root of the phonon numbers $\frac{c}{r\sqrt{n+1}}$. This is just a coherent state

$$|\alpha\rangle = e^{-|\alpha|^2/2} \sum_{i=0}^{\infty} \frac{\alpha^i}{\sqrt{i!}} |i\rangle. \quad (3.47)$$

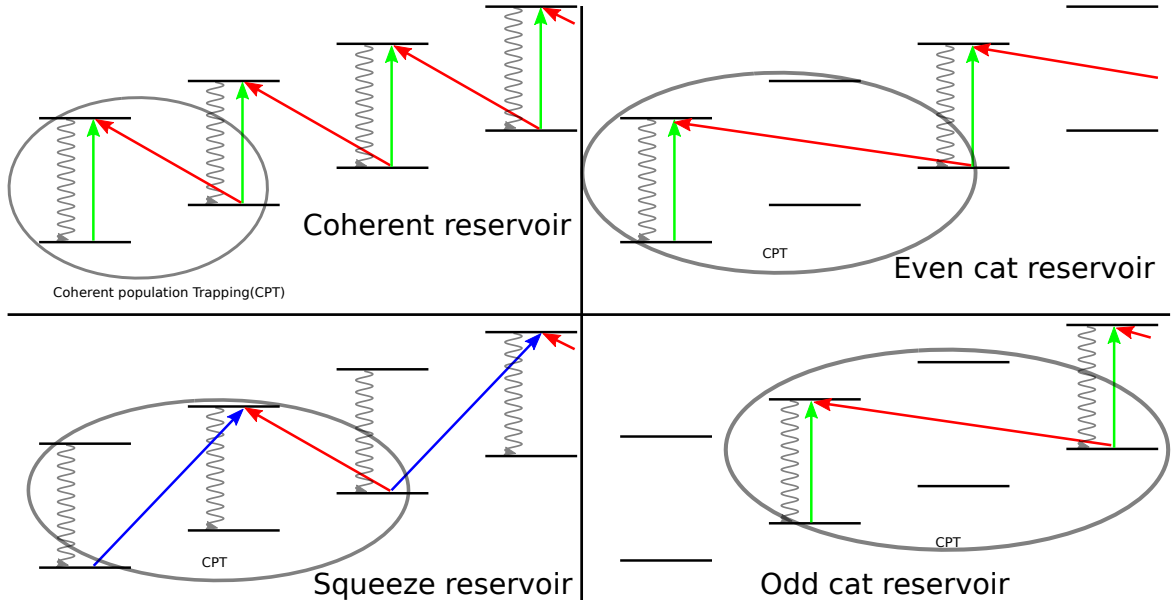


Fig. 3.19 The intuitive illustration from the view of coherent population trapping(CPT) to explain the engineered reservoir. In the coherent state reservoir, the red and carrier will form a CPT structure.

In the similar way, if we start from $|0\rangle$ and apply the red, blue sideband and the optical pumping together, we can get the squeezed state finally

$$|r\rangle = \frac{1}{\sqrt{\cosh r}} \sum_{i=0}^{\infty} (-\tanh r)^i \frac{\sqrt{(2i)!}}{2^i i!} |2i\rangle. \quad (3.48)$$

To check the theory, the numerical simulation is conducted. We apply the carrier, red sideband and optical pumping together. The Rabi rate of the carrier transition is α times of that of the red sideband

$$(\Omega_c - \Omega_r a)|\psi\rangle = 0 \quad \Omega_c = \alpha\Omega_r, \quad (3.49)$$

the solution of which is $|\psi\rangle = |\alpha\rangle$.

The strength of the optical pumping is very important. We can fix the time of the interaction and scan the pumping speed ω . Then we check the fidelity between the generated state and the target state. As an example data, we use $\alpha = 2$, $\Omega_r = \frac{\pi}{13 \times 10^{-6}}$ and the time is $t = 5\pi/\Omega_c$. After we choose the best pumping speed as in Fig. 3.20, we check the fidelity against time in Fig. 3.21. After a enough duration, we check the final state as in Fig. 3.22.

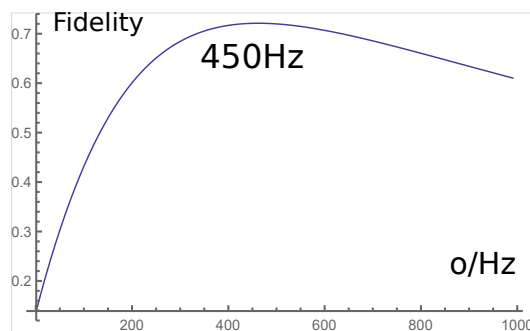


Fig. 3.20 The simulation to choose the best pumping speed. For the specific parameter, we should choose the best pumping speed. Too small or too large will decrease the evolution speed in the engineered reservoir.

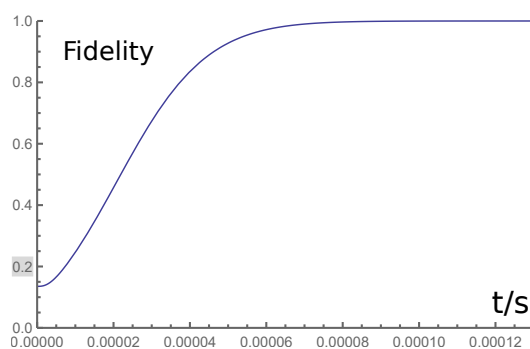


Fig. 3.21 The fidelity against time for the coherent state reservoir. We choose the shortest time to reach the required fidelity. If the time is too long, the decoherence from environment will decrease the fidelity.

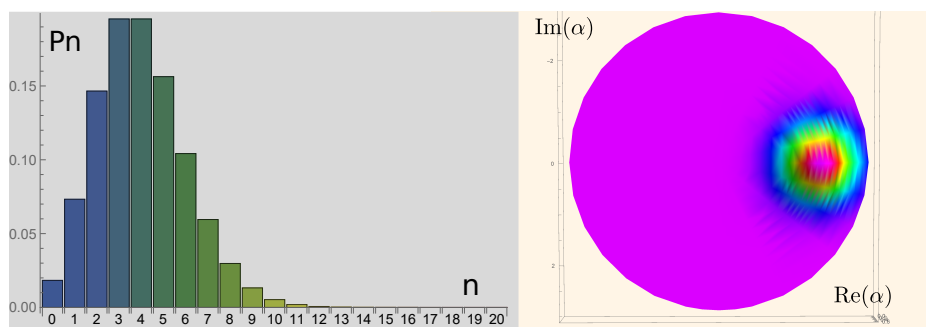


Fig. 3.22 The phonon distribution and Wigner quasi-distribution of the final state in the engineered reservoir for coherent state. Here $\alpha = 2$.

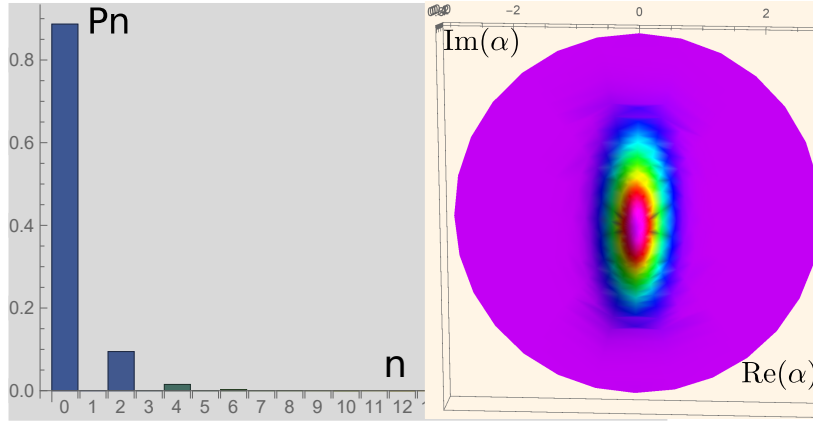


Fig. 3.23 The phonon distribution and Wigner quasi-distribution of the squeeze state generated by the engineered reservoir. The state in theory is $r = 0.5$.

The reservoir for the squeeze state is realized by applying the red, blue and pumping together. The ratio of the Rabi rate between the blue and red is $\tanh(r)$ in Eq. 3.48. We also need to choose the best pumping speed and the most suitable duration. The final result is showed in Fig. 3.23.

The cat state is more complicated. We apply the second order red, the carrier and optical pumping together

$$(\Omega_{2r}a^2 - \Omega_c)|\psi\rangle = 0. \quad (3.50)$$

The Ω_{2r} and Ω_c are the strength of the second order red sideband and the carrier. The spin operator is erased by the pumping process. It has two solutions: α and $-\alpha$ and $\alpha = \sqrt{\frac{\Omega_c}{\Omega_{2r}}}$. The finally dark state is highly depended on the initial state [42]. The operations in this reservoir keep the parity of states. If we start from $|0\rangle$, we will reach the even cat state $|\alpha\rangle + |-\alpha\rangle$. If $|1\rangle$, we get odd cat state $|\alpha\rangle - |-\alpha\rangle$. To check the theory, we do the numerical simulation starting from $|0\rangle$. The first step is to choose the best pumping strength and the suitable duration. The resulted state is showed in Fig. 3.24.

The engineered reservoir can not only prepare state but also be used to perform the gate operation [9]. We need to modify the parameters of the reservoir adiabatically. Then the dark state will also evolve. If we start from the even cat state and add the red sideband and change the parameters to push the $|-\alpha\rangle$ component in the even cat to close a circle. The area of the circle is just half of the geometric phase added on the $|-\alpha\rangle$ component. If area

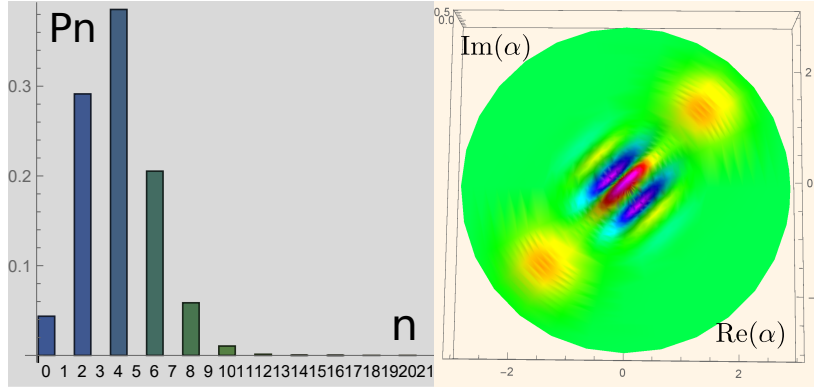


Fig. 3.24 The even cat states generated by the engineered reservoir. Here the relative phase between the carrier and the second red is π . And the strength of the carrier $\Omega_c = 2^2\Omega_{2r}$

is 2π , the geometric phase is π and the even cat will become odd. The simulation of this process is showed in Fig. 3.25. Now we have the σ_x operation for the single qubit in the cat code. The σ_z rotation is relatively complicated. We start from $|\alpha\rangle = |0_\alpha\rangle + |1_\alpha\rangle$ (without normalization), which is the state on the equator of the Bloch sphere of the cat code. If we can get the $|-\alpha\rangle$ component as much as we want, we can get the σ_z operation. We firstly reduce the α in the reservoir. Then generate the cat state with an angle of ϕ . Finally rotate the state with an angle of $-\phi$. In the end, we will get $\frac{1+e^{i\phi}}{2}|\alpha\rangle + \frac{1-e^{i\phi}}{2}|-\alpha\rangle$. This is just $|0_\alpha\rangle + e^{i\phi}|1_\alpha\rangle$. Thus we have realize the σ_z operation for the cat code. The simulation result is showed in Fig. 3.26.

Up to now we get all the single qubit gates. We need still the two qubit entanglement operation. Different from the Ref. [33], we use the beam splitting interaction to realize entangle cat qubit on two different modes. We start from $|\sqrt{2}\alpha^1\rangle + |-\sqrt{2}\alpha^1\rangle$ on the first mode. Then we apply the beam splitting operation between the first and the second mode. After a suitable time, we can get the state $|\alpha^1\alpha^2\rangle + |(-\alpha^1)(-\alpha^2)\rangle$ (without normalization). It is just the bell state of the cat code $|0_\alpha^1 0_\alpha^1\rangle + |1_\alpha^1 1_\alpha^2\rangle$. Now we have all the gates need for the cat code.

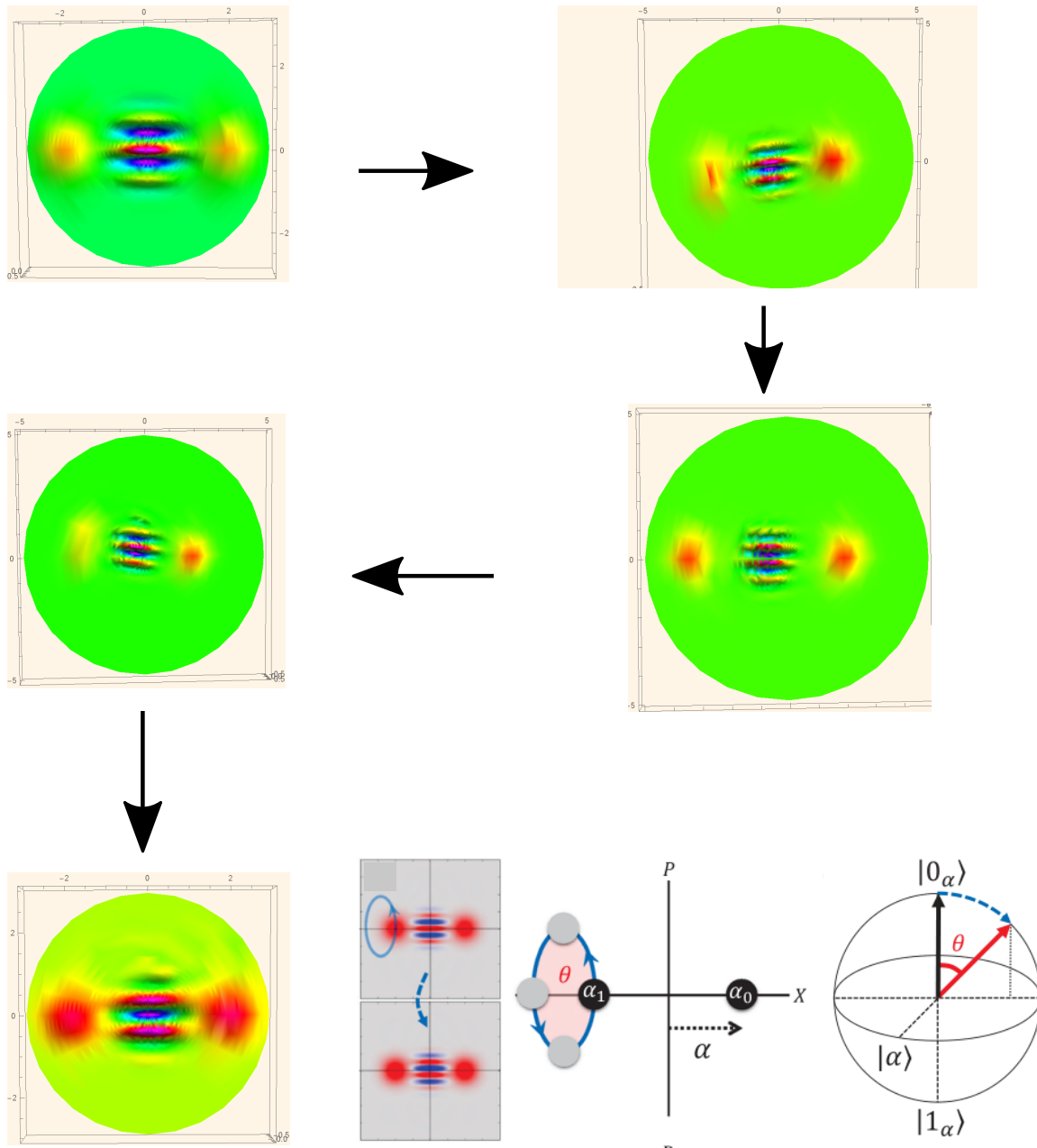


Fig. 3.25 The time evolution of the cat states in the time dependent reservoir. The even cat state after an adiabatic evolution will be the odd cat state. In the cat code this represent a σ_x rotation with a angle of π . Here we use $|0_\alpha\rangle = |\alpha\rangle + |-\alpha\rangle$ and $|1_\alpha\rangle = |\alpha\rangle - |-\alpha\rangle$ without the normalization. The final picture is cited from Ref. [9].

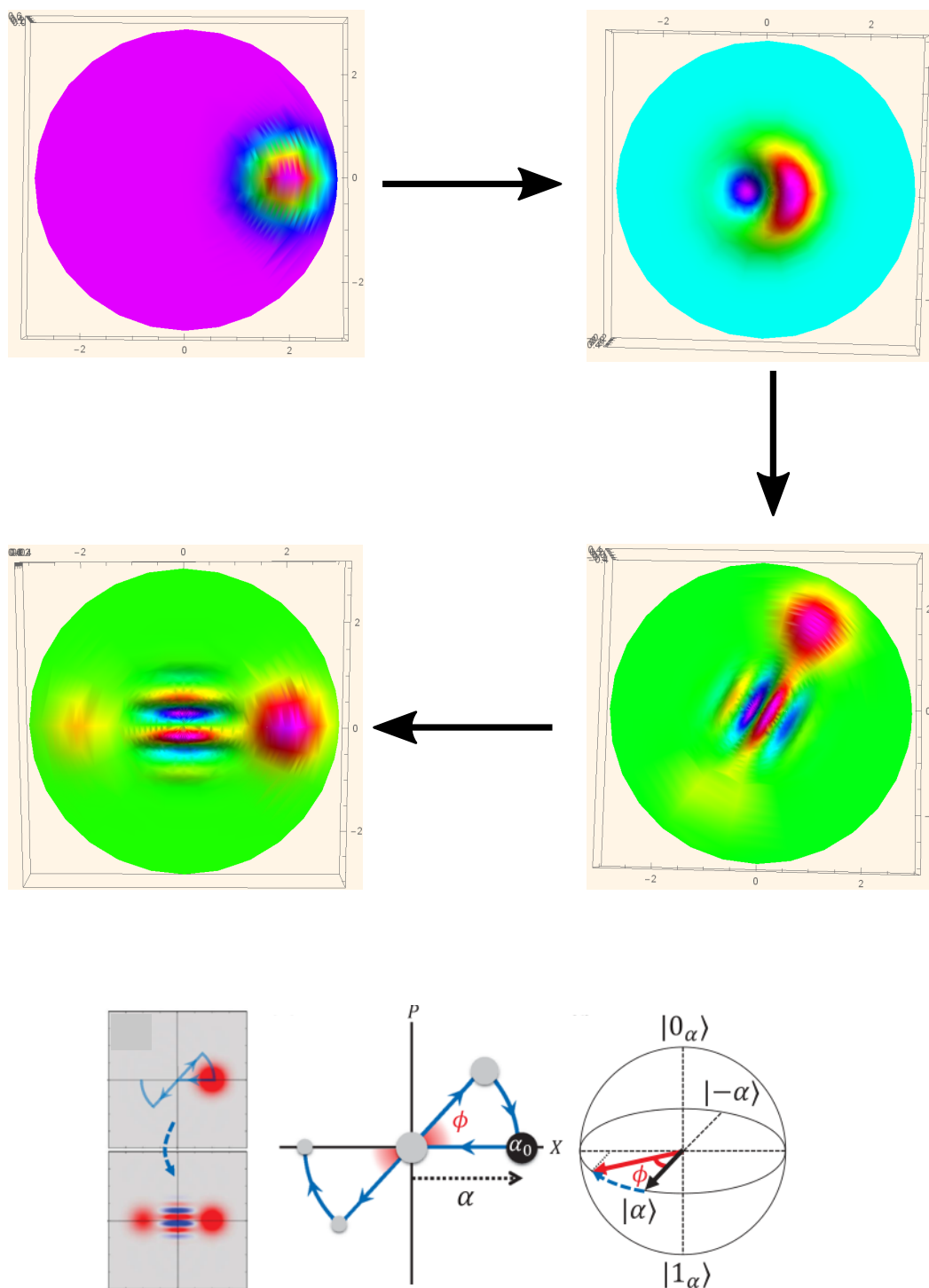


Fig. 3.26 The time evolution of the σ_z operation for the cat code. All the evolution is realized with the reservoir. Starting from $|\alpha\rangle$, we first reduce the size of the cat state reservoir to zero. Then increase the size of the cat along an axis of angle ϕ . Finally we rotate the cat state back with an angle of $-\phi$. As the final result, we realize the σ_z rotation. The final picture is cited from Ref. [9].

Chapter 4

Experimental setup

The purpose of this chapter is to describe what I have build in our lab. It will help the successors get familiar with the set up quickly.

4.1 The vacuum, blade traps, helical resonators and filters

To prepare the UHV (ultra high vacuum) environment is very important to trap the ion. To get about hours level collision rate, the vacuum should be 10^{-11} Torr level. We should be very careful not to contaminate the inner surface of all the vacuum components by the body oil. To reduced the out gassing rate of the stainless steel (mainly water vapor), we should bake the vacuum components for a long time to make all the surface of the steel yellow (chrome yellow). The thicker the oxidization layer, the smaller the out gassing rate will be. Typically we bake all the steel components to 300°C for several days. The joint components made of steel and glass or ceramic together are not baked separately but baked after the assembling of the whole vacuum system up to 200°C for 1 – 2 weeks.

After assembling everything together, the vacuum system is placed in a big oven. It is connected with a big ion pump (500L) and a turbo pump with a stainless steel bellows. The valve inside the big oven should be all metal, because it will be baked up to 200°C . At first, we turn on the turbo pump. After several hours, the vacuum will go to 10^{-7} Torr measured by the gauge at the turbo pump side. Now we should degas the atomic oven and the Ti

sublimation pump and also the ion pump. For the atomic oven, we use half of the current threshold for several minutes. The Ti sublimation pump should be degassed according the instruction in the manual. The ion pump has a limited life time and it strongly depends on the current. So in the vacuum condition now, we should not turn it on for a long time. For degassing and activating it, we just need to turn on and off it for several times. After we feel the turbo pump is roughly saturated, we close the valve for the turbo pump and on the valve for the outside big ion pump (500L). This big ion pump keeps heated up by heating tapes and its vacuum without connected with anything is 1×10^{-10} Torr. After connected with the whole system, the vacuum can be 10^{-8} Torr measured at the big ion pump. Now we can turn on the inner small ion pump (20L) (turn on and off it for several times at the beginning). Up to now, the big oven should begin to work. The temperature rising rate should be smaller than value for all the components we use in our system, which can be found with the manufacturers. Typically, we increase from the room temperature to 200°C in 24 hours. During the high temperature condition, we keep recording the vacuum measured at the inner small and outside big ion pump until the vacuum stops decreasing. Typically it can be 5×10^{-8} Torr at the inner pump and takes about 1-2 weeks. If the reading stops decreasing, we can turn off and on the inner ion pump. Then we turn off the heating tape for the outside big ion pump. The inside vacuum can drop to 3×10^{-8} Torr. After it reaches the room temperature, we begin to reduce the temperature of the big oven with the same rate as it is increased. After reaching the room temperature, the inside vacuum can be 2×10^{-10} Torr. Now we open the door of the oven and run the Ti sublimation for several times. During the first run, after the current is shut down, the vacuum keeps dropping quickly. Once it goes below the initial vacuum, we close the inside all-metal valve connected to the bellows with torque wrench and record the torque we use. The torque should be larger than the previous values. If lucky (all the components are clean enough and no leakages), after the first run, the vacuum can drop below 5×10^{-11} Torr and the inner ion pump will show "Low pressure". If not, we repeat running the Ti sublimation pump. If the vacuum is different from the values I list above too much, we should check all the sealing points with acetone. If there is leakage

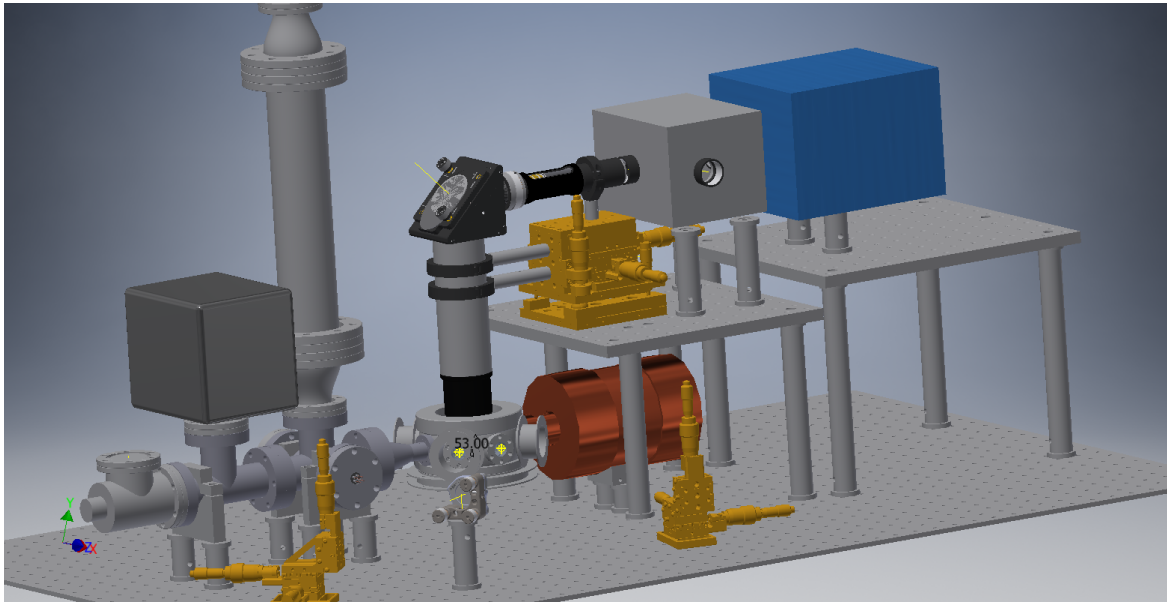


Fig. 4.1 The vacuum and detecting set up. We use ion pump (the black cube) and Ti sublimation pump (inside the long vertical tube) to maintain the UHV condition. The detecting system is designed to allow us to adjust the objective lens in $\hat{x} - \hat{y} - \hat{z}$ directions and also the notch and pitch directions. This imaging set up should allow us to align the objective lens perfectly.

and the acetone is applied, the pressure will drop quickly and increase back to the initial value after the acetone evaporates.

The trap is showed in Fig. 4.2. The size should be estimated by the CPO simulation. A key point for our trap is to make the horizontal distance larger than the vertical distance to avoid the scattering from the blade into the imaging system. The trap with its holder and the oven together with the chamber are showed in Fig. 4.3.

After we prepare the trap and the whole vacuum system and put it on the optical table, we should apply suitable RF and DC to the electrode. The DC voltages are used to separate the two radial modes, adjust the micro motion conditions and also trap the ion along the axial direction. The RF field should be high enough (larger than 500 V) to give us a high enough trapping frequency. If it is too small, the motional sideband should be too crowded and the gate speed will also drop a lot to avoid the off resonant coupling. However if we directly apply the RF from the commercial source and the amplifier, the power is not enough and most of the power will be reflected to the amplifier and destroy it. To realize the impedance matching

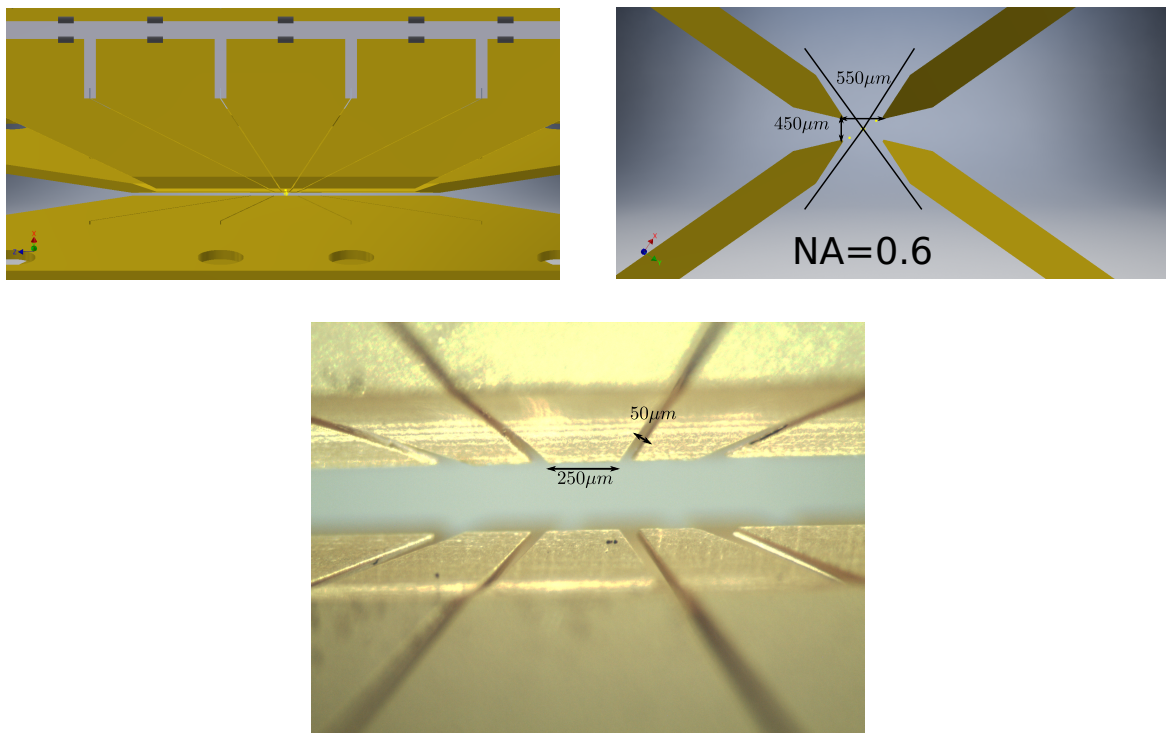


Fig. 4.2 The 5 segment blade trap. The basic sizes are showed. We should make the horizontal distance larger than the vertical distance to avoid the scattering from the blade into the imaging system.

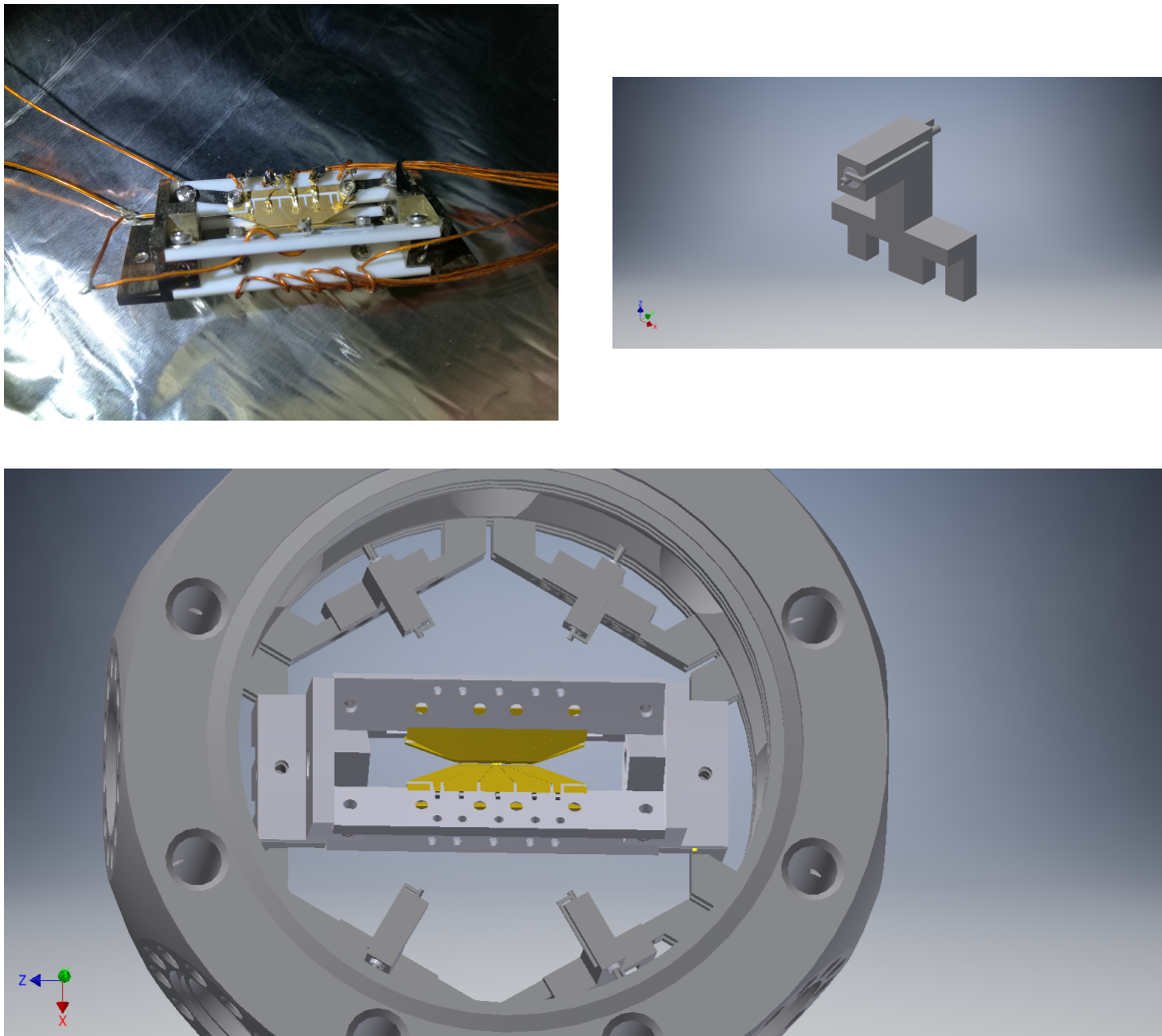


Fig. 4.3 The vacuum chamber and the trap with holder and ovens inside. The blades are placed on the macor holders and the macor holders are supported by two stainless steel X structure. The ground part of the DC blades are connected to this X structure.

and amplify the voltage, we use the helical resonator. It is basically a $\lambda/4$ resonant and use the helical coil inside to reduce its length [15]. For example, when the driving frequency is $2\pi \times 25\text{MHz}$, we need 3m long coaxial tube. If we use the helical resonator, it is just 20cm long. To trap the ion stably, especially for multi ions, the driving frequency should be at least 7 times of the trap frequency and minimize the micro-motion along the axial direction. In experiment, we use 3MHz trap frequency. So we choose 25MHz driving frequency after connected with the trap. The diameter of the tube is 10cm and the turns of the coils inside should be about 8 – 9. Before connecting the trap, the resonant frequency is 33MHz. We measure its Q value about 400 by dividing the resonant frequency by the measured resonant line-width from the reflection from the directional coupler after the amplifier. The RF flows on the surface of the copper. The skin depth is

$$d = \sqrt{\frac{2}{\omega\mu\mu_0\sigma}} = 9\mu\text{m}, \quad (4.1)$$

where for Cu, $\sigma = (1.673 \times 10^{-8}\Omega \cdot \text{m})^{-1}$, $\mu\mu_0 = 4\pi \times 10^{-7}\text{H/m}$ and $\omega = 2\pi \times 50\text{MHz}$. To improve Q factor, we use dilute phosphoric acid to clean the copper surface. A example data for the Q measurement is showed in Fig. 4.4. The capacitance of the blade trap is about 2pF. Connected, it drops to 25MHz and the Q value drops to 200. To compensate the phase and amplitude difference between the coils, we add a 10nF capacitor between the two wires after the coil structure. The amplified amplitude of the RF is

$$V_0 = h\sqrt{QP}, \quad (4.2)$$

where h is the geometric factor, Q is the quality factor and P is the power of the RF. The picture of the helical resonator and the trap frequency-power relation are showed in Fig. 4.5.

We also add the RF power stabilization set up to improve the motional coherence time. We connect one coil with a RF picker and a rectifier. I simulate the whole set up with the circuit model as showed in Fig. 4.6. The output voltage is much higher than the reality. And Q is also too good. The reason I believe is the circuit model can not include the radiation

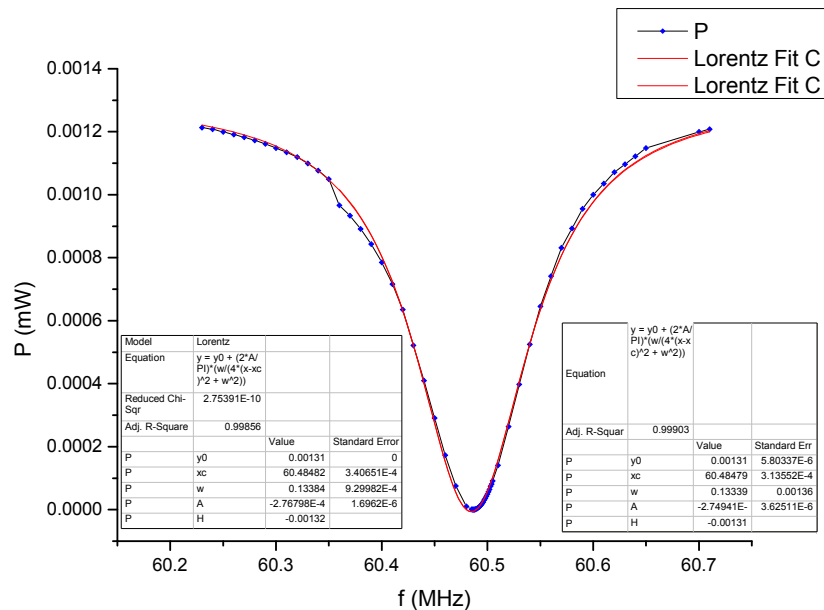


Fig. 4.4 Helical resonator's Q

dissipation. If we increase the resistance in this circuit, we can get the similar result as the experiment data. Thus the radiation effect can be simulated by adding an effective resistance. To increase Q we also need to reducing the radiation through reducing the length of RF wires and ground them by a nearby ground wires. At first we use the rectifier as the drawing made by ourselves. However we find its speed is not fast enough. Later we find a commercial RF power detector bought from a local company ¹. Its speed is more than hundreds times faster than the one we make. We use the detected DC voltage as the input of a digital PI controller and the error signal. At first we feedback the error signal to the AM port of the RF source. However, we find this function has several μs delay. Finally we use the RF mixer as the voltage controlled attenuator. Its speed is fast enough compared with the characteristic dumping frequency of the helical resonator, which is $\frac{25\text{MHz}}{Q=200} = 125\text{kHz}$ for us. The only problem for the mixer solution is that the output will be distorted as showed in Fig. 4.7. We use the traditional output as the DC input to control the amplitude of the RF. In experiment we see this distortion. But the ion is still trapped well. We believe the helical resonator filters

¹<http://www.shx-sh.com/>

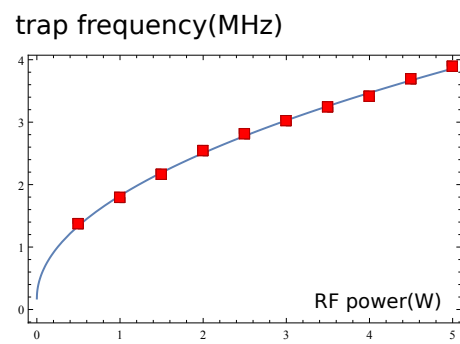
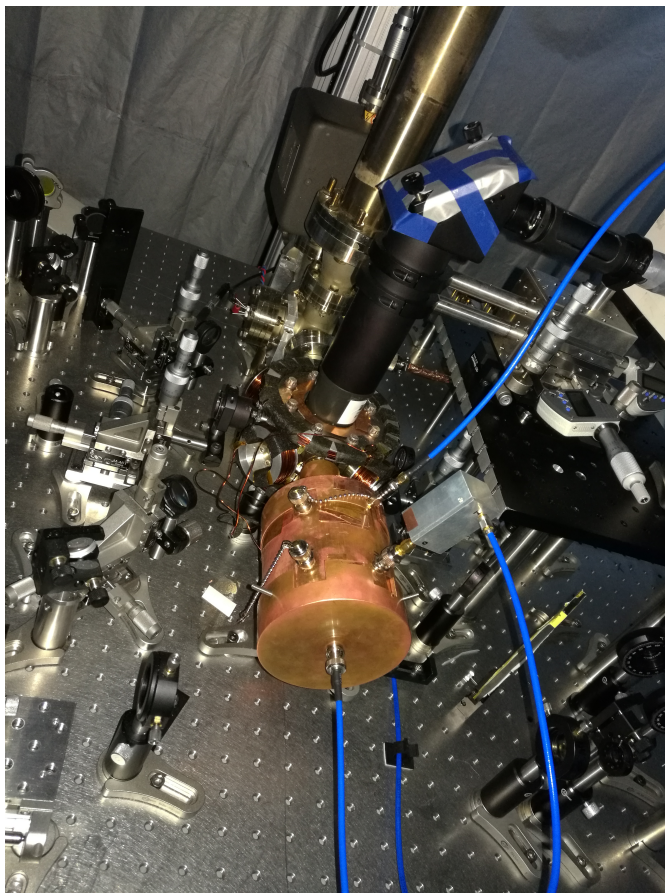
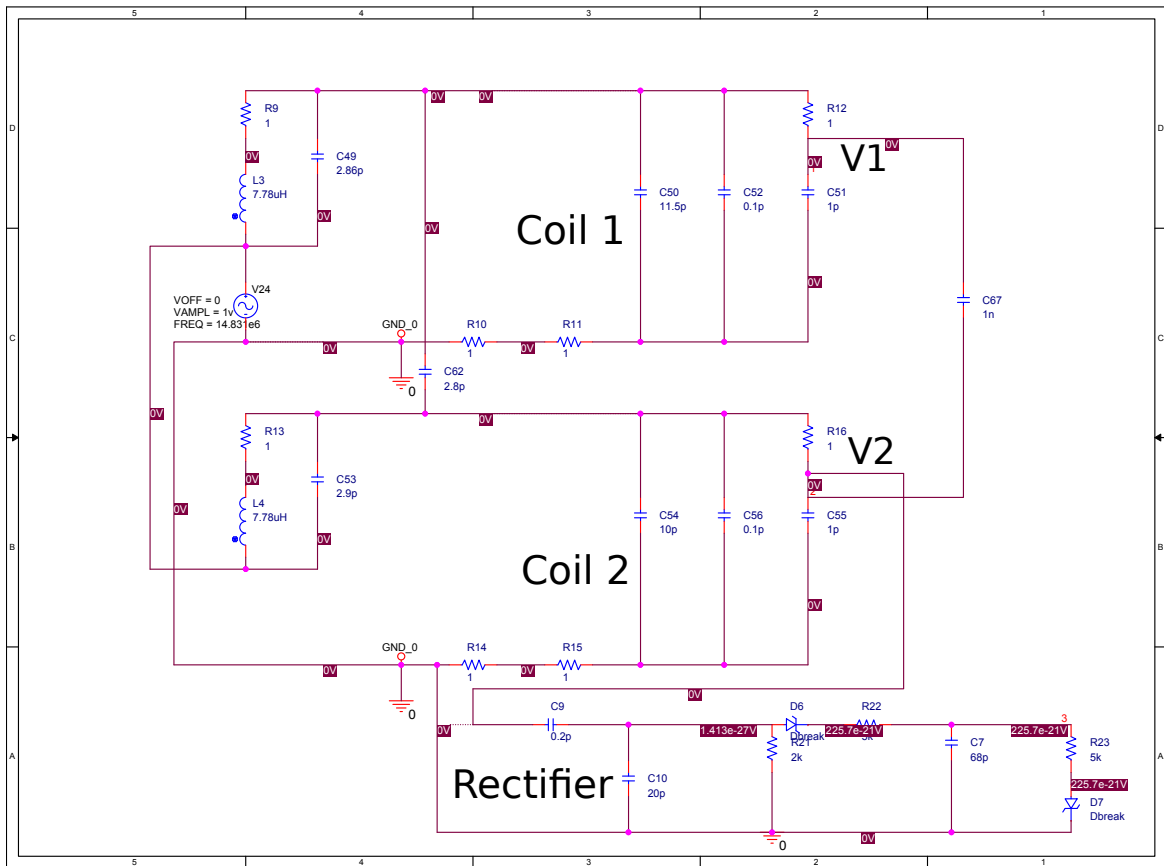
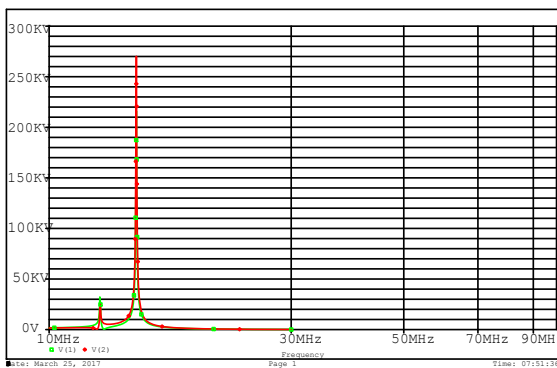


Fig. 4.5 The picture of the helical resonator and the trap frequency-power relation.



Without 1nF capacitor



With 1nF capacitor

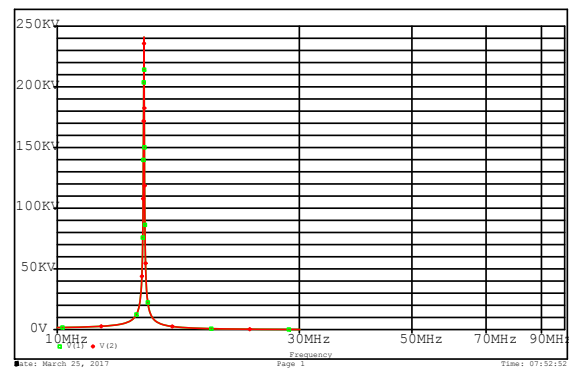


Fig. 4.6 The circuit model simulation of the bifilar helical resonator connected with voltage picker and the rectifier. To make sure the amplitude and phase same between the two coils, we add 1 nF capacitor between this two coils. The output voltage is much higher than the reality, because we do not consider the radiation dissipation. It is used to find the general features of the helical resonator.

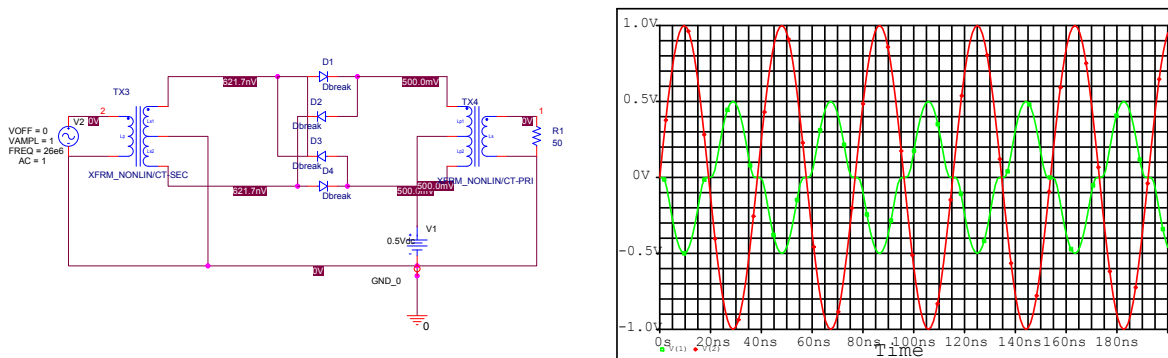


Fig. 4.7 The simulation of the mixer used as the voltage controlled attenuator. We use the traditional output as the DC input to control the amplitude of the RF. The shape of the output will be distorted. In experiment we see this effect. But the ion is still trapped well.

out all the other frequency components other than the resonant frequency. With the RF power stabilization setup, we improve the motional coherence time four times.

The DC voltages we apply to the blades should be filtered to reduce the noise and short the RF pick up to the ground within a short loop to reduce the radiation. We find the ceramic capacitors will generate noise (pulsed tens MHz noise) and a resistor is needed to get rid of such noise. We need to apply the DC on the DC blades and also to the coil of the helical resonator. We design two boards that works well without noticeable noise as showed in Fig. 4.8. We measure the cut off frequency and the suppression at the trap frequency and the driving frequency to choose the best values of the R and C. We should notice that the capacitor at low frequency side works as an ideal capacitor. At the high frequency side, the parasitic inductance will be more important. And the larger the C is, the larger the parasitic inductance will be. However the smaller the C is, the cut off frequency will be higher also. We should make a balance.

4.2 Diode laser systems

For ionizing, cooling, pumping and detecting, we use the diode lasers. Depending on the situation, we may need to stabilize the frequency, power, polarization and pointing stability.

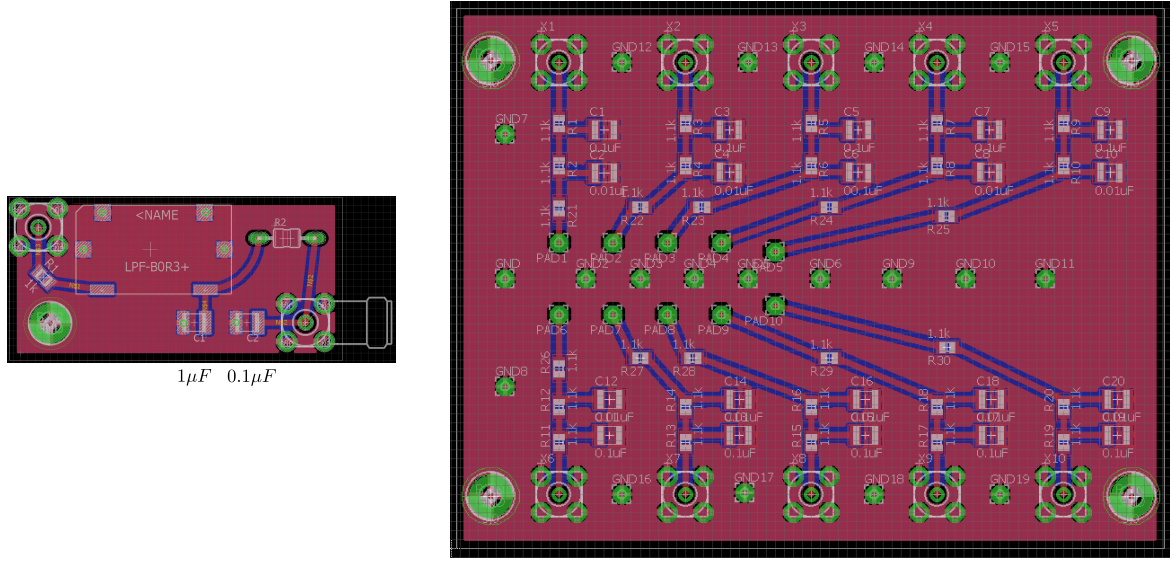


Fig. 4.8 The board drawings of the filter designed to apply DC on the RF coil and DC blades.

For a two level system, the scattering rate is

$$\Gamma_{sc} = \frac{\frac{I}{I_{sat}} \frac{\Gamma}{2}}{1 + \frac{I}{I_{sat}} + \frac{4\Delta_l^2}{\Gamma^2}}, \quad (4.3)$$

where I is the intensity of the incident light; $\Gamma = 1/\tau$ is the spontaneous emission rate of the transition, with τ the natural lifetime of the excited state, and is related to the natural line width $\gamma = 2\pi/\Gamma$; and Δ_l is the detuning of the incident light from the resonant frequency. We have also used the saturation intensity I_{sat} , which is given by

$$I_{sat} = \frac{\pi hc \Gamma}{3\lambda^3 R_{br}} \quad (4.4)$$

where R_{br} is the branching ratio from the upper level to the lower level. For Yb ion, $\tau = 8\text{ns}$ and the line width of the spectroscopy is 20MHz, which is too large for the motional sideband resolving. Typically, we need MHz level stability of the laser frequency to ionize, cool, pump and detect the ion. If for the quadrupole transition, we need to reduce the line width of the laser a lot. In this subsection, I will introduce all the stabilization setup I have built and also the typical beams path.

We will introduce the PDH lock at first. The reflected fields from cavity is:

$$F(\omega) = \frac{E_{ref}}{E_{inc}} = \frac{r(\exp(i\frac{\omega}{\nu_{fsr}}) - 1)}{1 - r^2 \exp(i\frac{\omega}{\nu_{fsr}})} \quad (4.5)$$

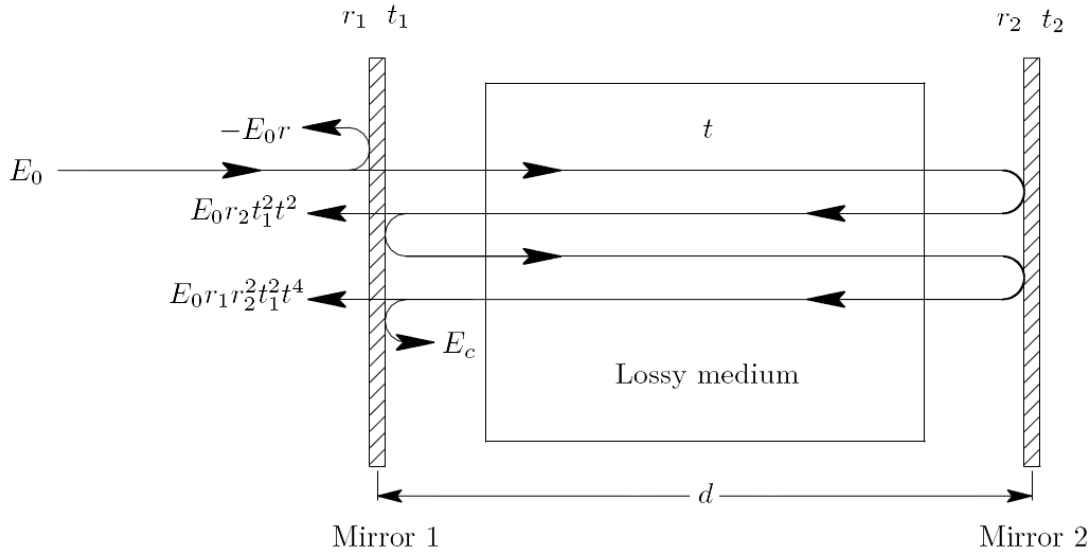


Fig. 4.9 Reflected fields from cavity due to several round-trips inside the cavity, cited from Ref. [1].

For the cavity we make, we estimate the amplitude reflection rates of the 2 mirrors are both $r = 0.993$, the length of the cavity is $L = 0.15\text{m}$ and the free space range is $\nu_{fsr} = \frac{c}{4L} = 500\text{MHz}$ for the confocal cavity. The finesse is $F = \frac{\pi r}{1-r^2} = 224$. We can get the reflection against frequency and its phase in Fig. 4.10. We find that its phase has different signs when the laser's frequency is higher or lower than the resonant frequency. The problem is the phase is a mathematical concept. It is not an electronic signal that we can directly use as the error signal. So we need develop some method to change the phase to some kind of electronic signal. This is the key point of PDH lock. To do this we introduce two kinds of modulation-demodulation. They can change the phase to some electronic signal. If we add a

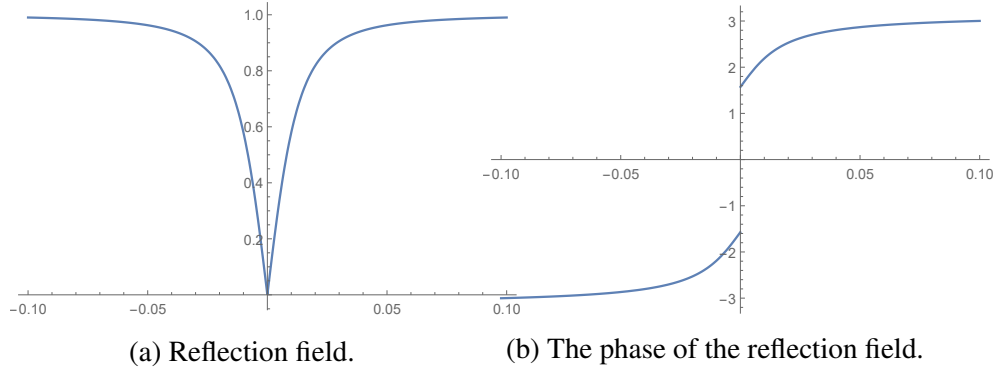


Fig. 4.10 The reflection signal and its phase. The horizontal axis is in the unit of w/v_{fsr} .

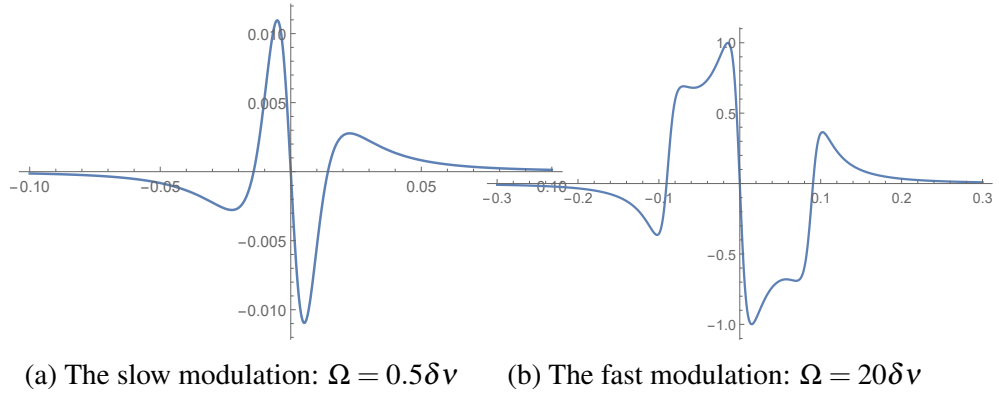


Fig. 4.11 The error signal for slow and fast modulation. The horizontal axis is in the unit of w/v_{fsr} .

phase modulation by the Pockels cell or frequency mixer, we can get:

$$E_{inc} \approx E_0[J_0(\beta)e^{iwt} + J_1(\beta)e^{i(w+\Omega)t} - J_1(\beta)e^{i(w-\Omega)t}] \quad (4.6)$$

$$E_{ref} = E_0[F(w)J_0(\beta)e^{iwt} + F(w+\Omega)J_1(\beta)e^{i(w+\Omega)t} - F(w-\Omega)J_1(\beta)e^{i(w-\Omega)t}] \quad (4.7)$$

So what we can measure is the Ω frequency part in $P_{ref} = |E_{ref}|^2$. sin or cos part depends on the relative phase. The slow modulation means Ω is very small compared with the cavity linewidth $\delta\nu = \frac{v_{fsr}}{F} \approx 2\text{MHz}$. The fast modulation means the Ω is larger than $\delta\nu$. The numerical results are showed in Fig. 4.11. Between these two kinds of error signals, we choose the fast modulation. It can give us a wider error signal. That's the PDH lock. Its

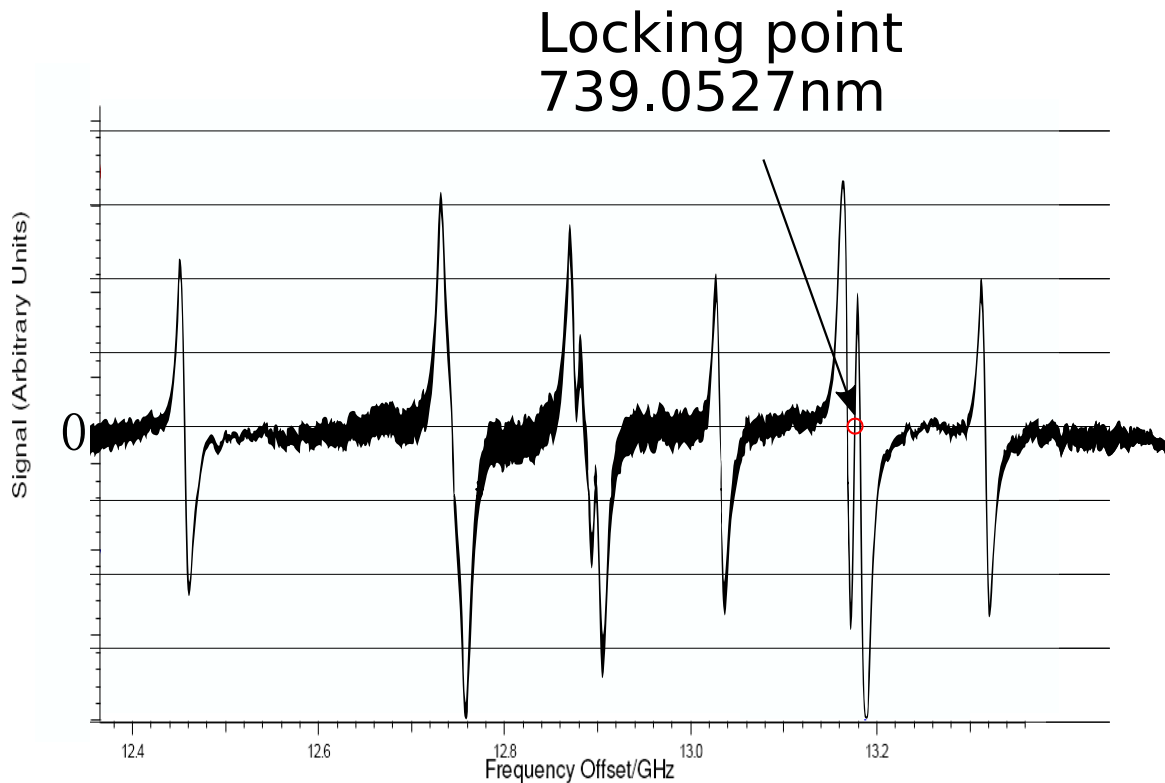


Fig. 4.12 The error signal we get from the Iodine frequency modulation lock. We should notice that the error signal is not symmetric along the horizontal axis. This is the so called remained amplitude modulation.

property is the fast reaction to the change of wavelength but may be not reliable in a long time. So we still need a natural frequency standard.

For this purpose, we build the I_2 lock for the 740nm laser, the Te_2 lock for the 493nm laser and the hollow cathode lamp lock for the 370nm laser. The I_2 lock set up is similar to the one described in the Ref. [43]. So I only show the error signal we get in Fig. 4.12. If we are careful enough, we should notice that the error signal is not symmetric along the horizontal axis. This is the so called remained amplitude modulation. It may change the locking point and reduce the locking range. When it is too serious, the error signal will not pass zero even. When we do the frequency modulation lock, we add the frequency modulation on the AOM. However, the output power and direction are also modulated by this frequency modulation. The intensity of the strong beam and the overlap between the



Fig. 4.13 The remained amplitude modulated (RAM) error signal. When the strong beam is modulated with the amplitude or direction, the resulted error signal will be asymmetric.

prob beam will be modulated. This effective strong beam amplitude modulation will modify the symmetric error to be asymmetric vertically as showed in Fig. 4.13.

To correct this error, in the Te_2 lock, I modify the AOM to the double pass configuration. Then the direction of the output from the AOM will not be modified. I compare the result with the one pass configuration and the double pass configuration as showed in Fig. 4.14. It is clear that, the double pass configured AOM can reduce the remained amplitude modulation a lot. For more information on this remained amplitude modulation see Ref. [44].

When the frequency of the laser is close to the crowded molecular transition lines, we can use different vapor cell to lock. However when I use the 370nm diode laser, the frequency is too high for most molecular transitions. So we choose to use the hallow cathode lamp of Yb and the amplitude-modulated polarization spectroscopy [45]. Here we turn on and off the AOM to get the difference between the saturated prob and non-saturated prob beams. When the strong saturated laser is on, it will saturate the same polarization component in the prob beam. The counter propagating configuration will give us the Doppler free signals. We can also do this with the frequency modulation method. However, the on-off modulation method will not introduce the remained amplitude modulation. Even we use the double pass AOM configuration, the AOM efficiency is still frequency dependent. The remained amplitude modulation still exists though very small. The error signal around the transition of $^{171}Yb^+$ is showed in Fig. 4.15.

The problem is the wide error signal. Its width is about $2\pi \times 400\text{MHz}$. And we can reduce the error signal to 5mV after locking. Compared with the $V_{pp} = 1V$ of the error signal, we estimate the linewidth of the laser is about $400 \times \frac{1000}{5} = 2\text{MHz}$. It is not that small but enough for our daily operation. The drawing of this setup is showed in Fig. 4.16.

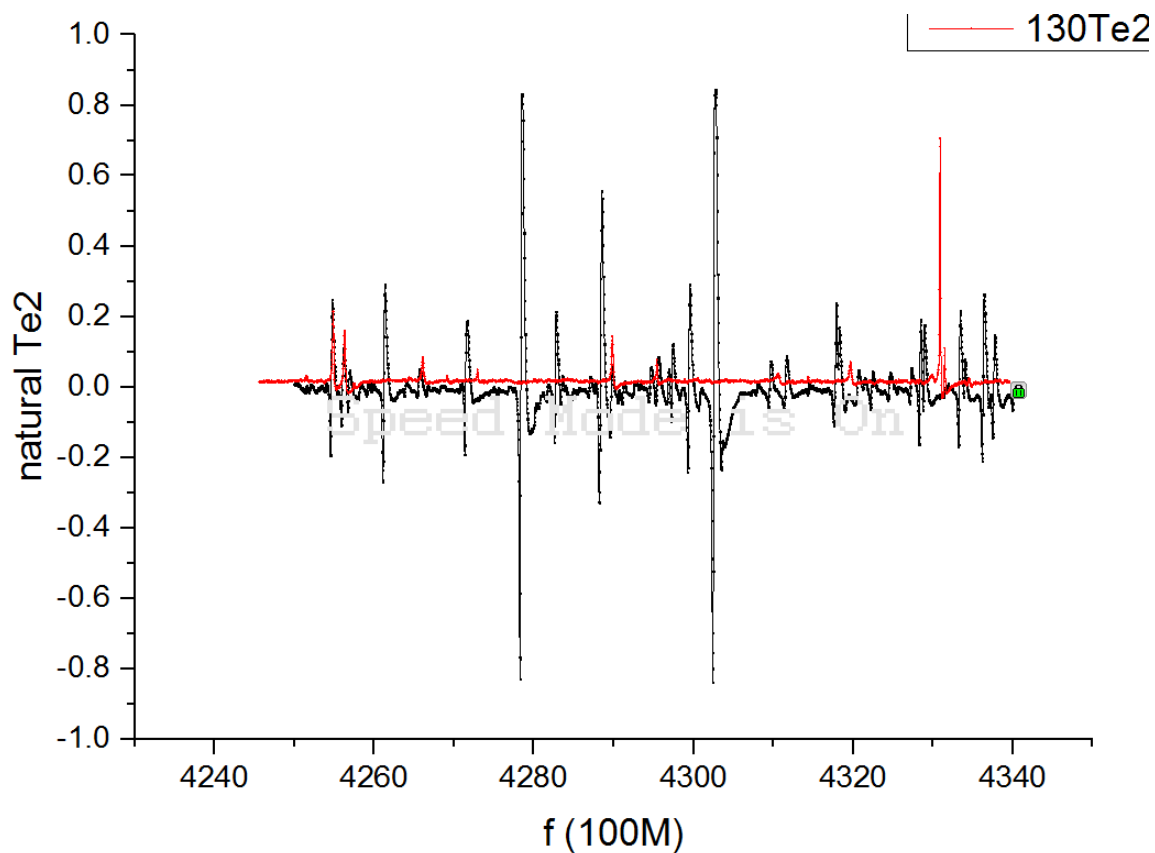


Fig. 4.14 The error signal comparison between the one and double pass AOM configuration in the frequency modulation lock. I use two different cell. So the peaks can not overlap. We guess the Te_2 isotopes are different in the different cells. The black one is filled with the natural Te_2 . The red line is for the one pass configuration and the black one is for the double pass configuration.



Fig. 4.15 The error signal before and after locking with the Yb hollow cathode lamp.

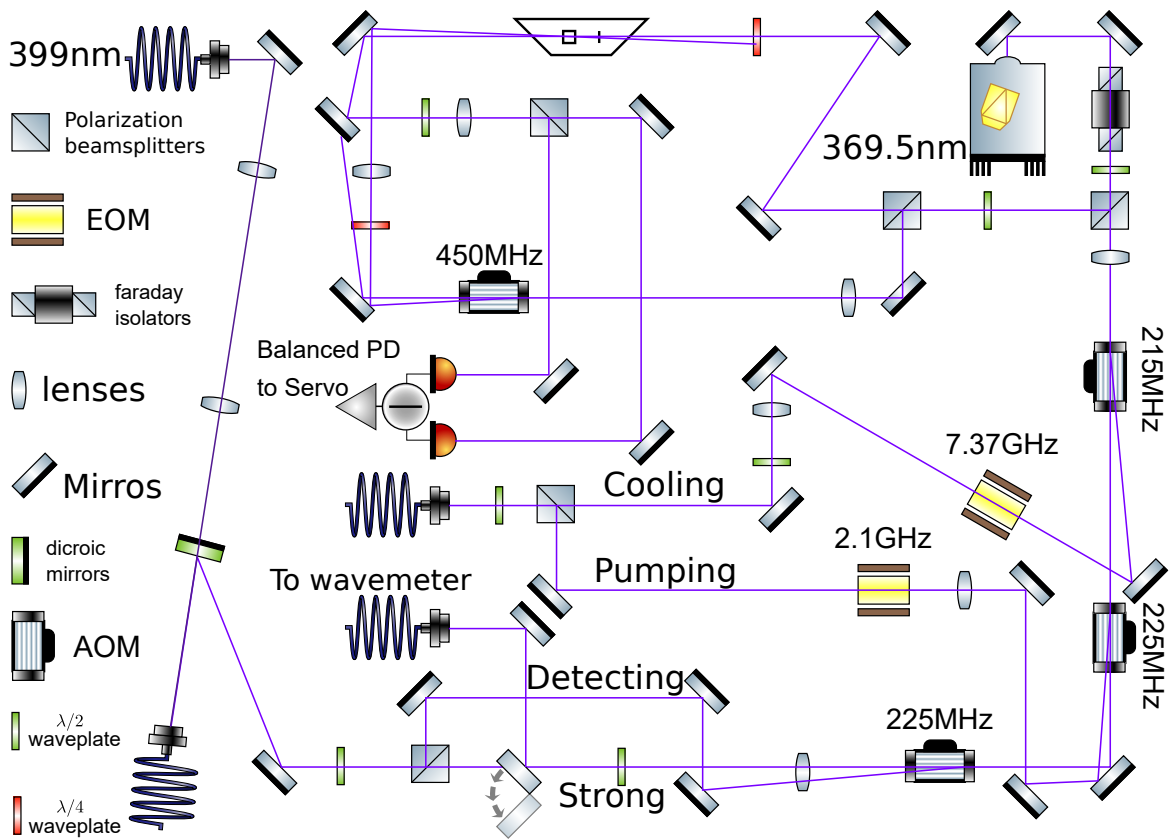


Fig. 4.16 The beam path of the all fiber solution of the 370nm laser system. The hallow cathode lamp lock setup is on the top. I use about 2mW for the laser frequency stabilization and the remained 1.5mW is used for cooling, pumping and detecting.

The problem I have with this 370nm diode laser is its small power. After the isolator only 3.5mW left. If I use the same optics as used in the old 740-370 laser system, the power will not be enough. So I try to use all AOMs in a series. Because operations for ion are not conducted at the same time, we can reuse the laser power. In order to improve the pointing stability and also simplify the alignment, I choose to couple all the diode laser beams into polarization maintaining fibers. To save the fibers and simplify the optics, we combine the cooling and pumping laser into one fiber, the detecting and the strong ionization and 399nm ionization beams are combined in one fiber as showed in Fig. 4.16. The beam paths before the trap is showed in Fig. 2.6. When we use fibers, we should use tilted end fibers (FC/APC) to reduce the reflection to diode lasers from fibers.

4.3 The pulse laser system

To manipulate the qubit and motional states, we use the pulse laser. The theory has been described in the third chapter. Here I will introduce all the experiment set up in the lab related to the pulse laser system. The pulse width is about 10ps. Thus its line width is about 100GHz. The frequency fluctuation compared with the laser linewidth is too small. The pulse laser operation is based on the repeatation rate. If the the repeatation rate is not stable, the coherence of all the operation will be destroyed. To lock the repeatation rate, I have tried two methods: feed forward and feed back. The feed forward method has been well described in Ref. [46]. I will not introduce more. With the feed forward lock, we can improve the coherence time of the carrier operation up to tens ms from less than 1 ms. The coherence will also affected by the laser power fluctuation. The only problem for this set up is that it can not work when the spin is not involved. In the spin independent force, the feed forward lock will even make the coherence worth. To solve this problem, I change to use the feed back method. I try this method in two pulse laser. At first, I use the HighQ laser. It is a SESAM picosecond pulse Nd:YAG laser. Its frequency is 1064-532-355. The line width of its repeatation rate is quite narrow measured with the 532nm laser for the detector does not work for the 355nm directly. Using the ultrafast PD, we see the linewidth at 6.32GHz high harmonic is just about

several Hz. So I do not need to reduce its linewidth. Just compensating the long term drift is enough. I feed back through the PLL system with the base frequency at 80MHz. The next pulse laser I use is the Mira laser from Coherent. It is Ti sapphire laser. We find its linewidth at the 6.32GHz high harmonic is about 1 – 2kHz. It is too big. Just using the base frequency at 76.2MHz is not enough to reduce its linewidth, because the error signal is too slow and P component in the PI servo controller does not work. It can only guarantee the long term drift. To solve this problem, I choose to use the high harmonic to lock as showed in Fig. 4.17. At the high harmonic detected by the ultrafast PD (EOT-4000 from EOT), the error signal will be much faster than that of the base mode. So we can increase the P components in the servo controller (LB1005 from New Focus). With this high speed PLL feedback, we can reduce the linewidth of the repetition at 12.64GHz within 0.1Hz, which is estimated through the error signal. Thus the coherent control will not be affected by the repetition rate. Another decoherence source from the pulse laser is the intensity fluctuation. To reduce it, we add an AOM at the beginning of the beam path and control the intensity as showed in Fig. 4.17. A window plate is used to sample the laser power and we use the internal DC source as the reference. At first we use built-in AM function for the feedback. Later we find this built-in function has a delay on the scale of tens of μ s level. So we change to use the mixer as a voltage controlled attenuator. Its speed is just 1 μ s level.

After this two stabilizations, the coherence time of the carrier operation is still tens of ms level. We believe the main error source is pointing stability of the UV pulse laser. To improve this, one possible way is to use fiber like the diode laser system. However the normal PM fiber will be damaged by the UV pulse laser easily. When the power is larger than 10mW, it is very obvious. The Ref. [47] introduces that hydrogen loading can be used to make the fibers stronger against the UV. We do this with a photon crystal fiber and find up to 100mW, the fiber is still safe for the 355nm picosecond pulse laser.

The pointing error can also be introduced by the angle difference of the AOM at different driving frequency. The first order motional sidebands are 3MHz from the carrier transition. This frequency difference will affect the alignment of the Raman beam. To compensate this error, we use the reply imaging. We focus the beam at the AOM and put a 300 mm lens after

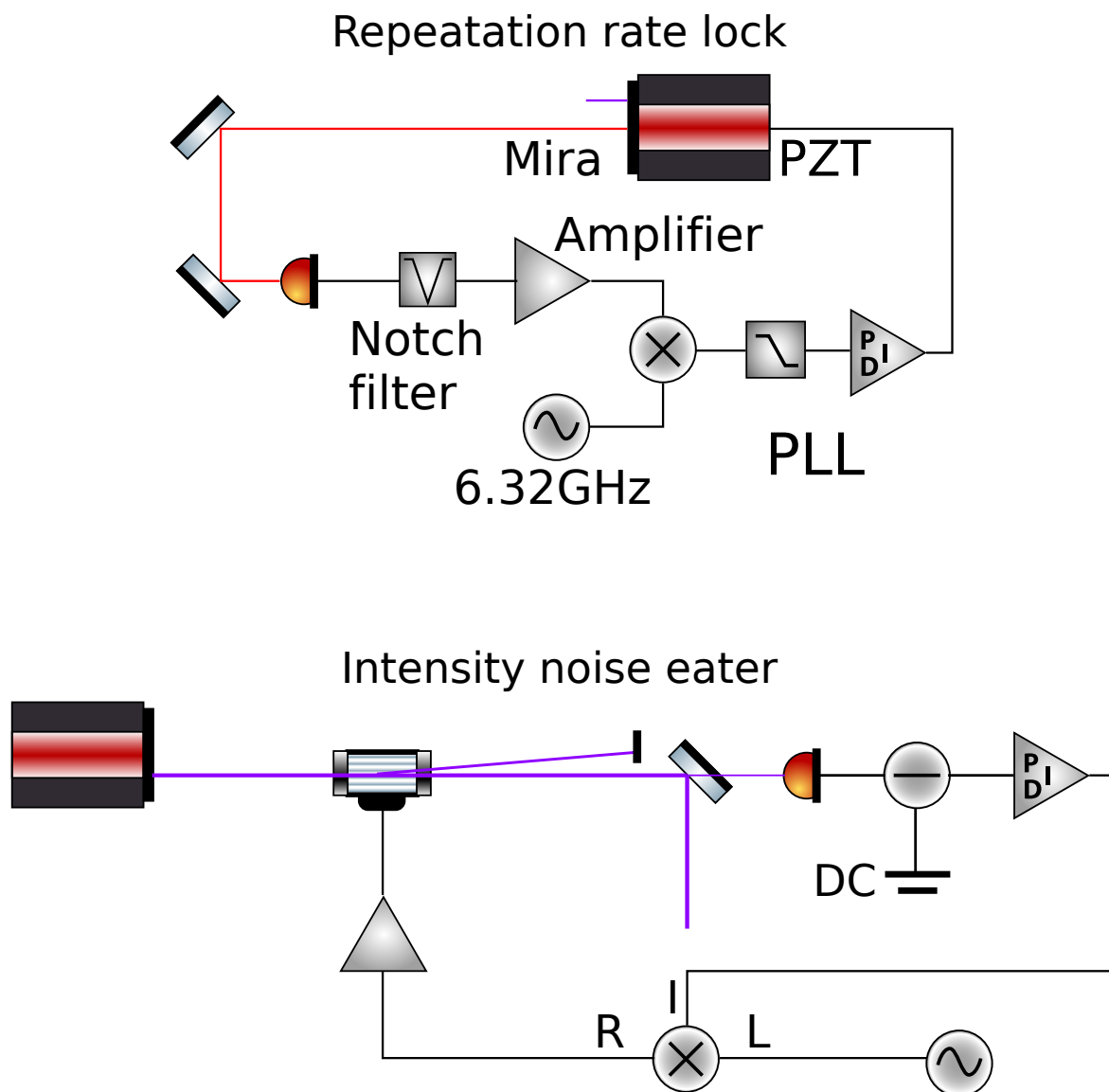


Fig. 4.17 The repeation rate and intensity noise eater for the pulse laser. In the repeation rate lock system, we choose to use the high harmonic to realize the PLL.

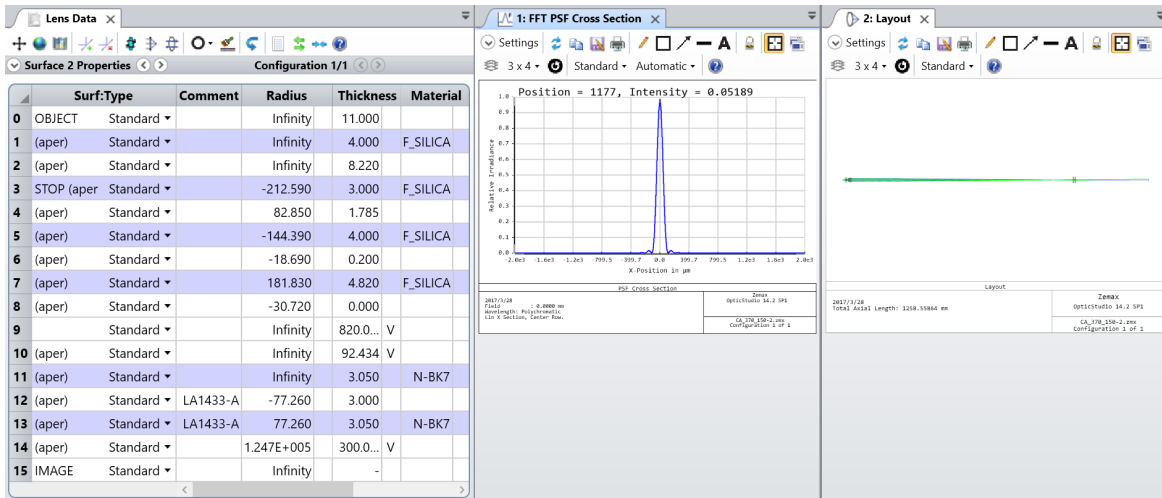
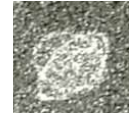


Fig. 4.18 The imaging simulation of the CVI lens at 370 nm. Its N.A. is 0.23. And we can see an ion clearly without noticeable abbreviation. The detection for $\bar{n} = 10$ photons takes $350\mu\text{s}$.

the AOM at the focus length of the lens, after which the beam will be parallel. Then we use two lens to amplify the width of the beams by 3 times to increase the laser intensity at the ion. We put an $150\mu\text{m}$ pinhole at the focus point after the first amplification lens. It will help to clean the scattering and work as a reference for the beam alignment. Finally it will be focus down by a 100 mm lens. At the ion position the width will be around $15\mu\text{m}$. And the AOM is also imaged at the ion position, which means the beam will be stable when the frequency of the AOM is changed.

4.4 The detecting system

We have used three different kinds of objective lens. The first is UVO-20.0-10.0-355-532 from CVI. Its N.A. is 0.23. The beam paths, optics and the simulation is showed in Fig. 4.18. Because its N.A. is still not that large, we can see the ion without noticeable abbreviation. The detection takes a relatively long duration of $350\mu\text{s}$. We also try a similar lens with a shorter effective focus length from a local company. Later we change to the large N.A.=0.6 lens [48] and get a shorter detection duration of $60\mu\text{s}$. However we see a serious abbreviation as showed in Fig. 4.19. We try to correct the abbreviation by using the cylindrical lens and



Defocused

Focused

Defocused

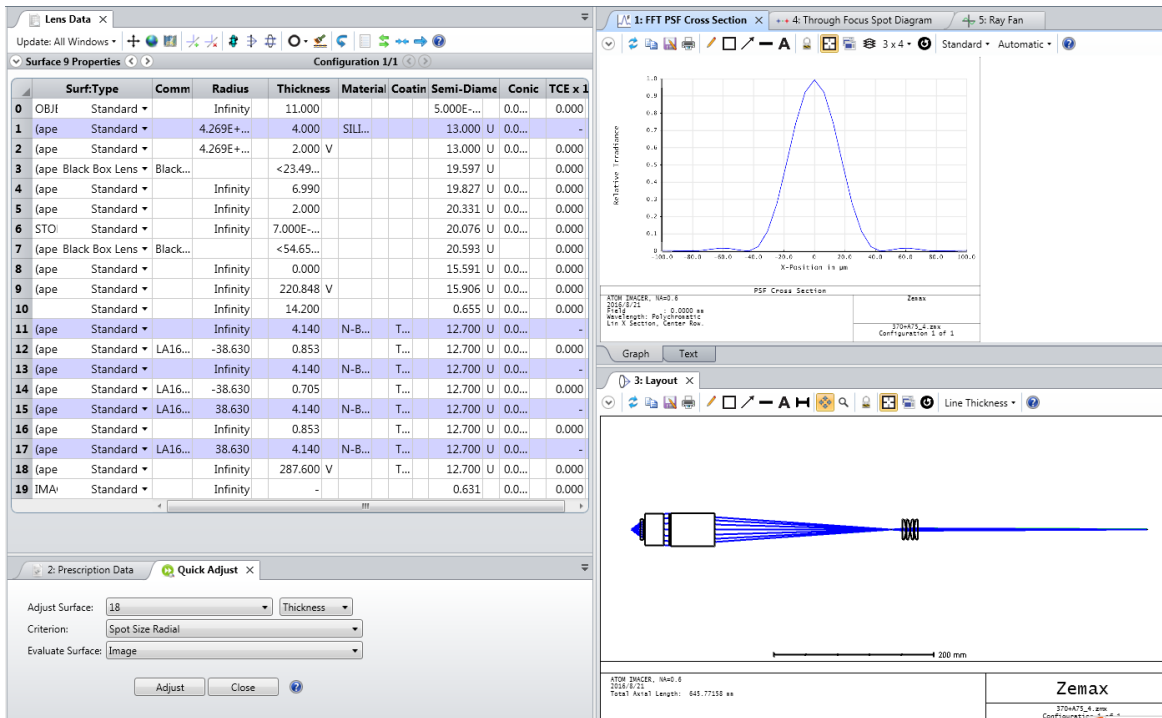


Fig. 4.19 The imaging simulation of the Photon Gear large N.A. lens at 370 nm. We see the noticeable abbreviation.

use the five axis translation stage to align the objective lens. Unfortunately, the image is not improved.

Chapter 5

Experimental test of the quantum Jarzynski equality

In this chapter I will add more data, experiment details and theory background of our publication [49].

5.1 The quantum Jarzynski equality

The Jarzynski equality relates the free-energy difference between two equilibrium states to the work done on a system through far-from-equilibrium processes. Though the classical version was discovered at first [50], the quantum version is relatively easy to get in a closed system

$$\begin{aligned}\langle e^{-\beta W} \rangle &= \sum_{n,m} \frac{e^{-\beta \epsilon_0^n}}{Z_0} P_{n \rightarrow m} e^{-\beta W} \\ &= \sum_{n,m} \frac{1}{Z_0} P_{n \rightarrow m} e^{-\beta \epsilon_1^m} \\ &= \sum_m \frac{e^{-\beta \epsilon_1^m}}{Z_0} \\ &= \frac{Z_1}{Z_0} = e^{-\beta \Delta F}\end{aligned}\tag{5.1}$$

where we use the subscript 0(1) to denote the initial(final) equilibrium system. The partition function and free energy are

$$Z = \sum_n e^{-\beta \epsilon^n} \quad (5.2)$$

$$F = -\beta^{-1} \ln Z. \quad (5.3)$$

And the work is defined as

$$W = \epsilon_1^m - \epsilon_0^n. \quad (5.4)$$

For a more rigorous treatment, the Ref. [51] is a good choice. Traditionally the thermal dynamics rules are in the inequality form, such as the second law and Clausius inequality

$$\langle W \rangle \geq \Delta F. \quad (5.5)$$

Using the Jensen's inequality, we can easily get it from the Jarzynski equality. The Jarzynski equality is a better understanding of fluctuation relation. And it can allow us to measure the free energy difference with arbitrarily fast process. Its classical version has been tested in experiment in Ref. [52]. However its quantum version was still an untested theory before our work. We report an experimental test of the quantum Jarzynski equality with a single $^{171}\text{Yb}^+$ ion. We perform projective measurements to obtain phonon distributions of the initial thermal state. We then apply a laser-induced force to the projected energy eigenstate and find transition probabilities to final energy eigenstates after the work is done. By varying the speed with which we apply the force from the equilibrium to the far-from-equilibrium regime, we verify the quantum Jarzynski equality in an isolated system.

5.2 The thermal state preparation

As what we have seen in the derivation, the initial thermal state is very important. After the Doppler cooling, the average phonon is about 10. It is a little too high. So we start from the resolved sideband cooling. The average phonon is about 0.02 after the resolved sideband

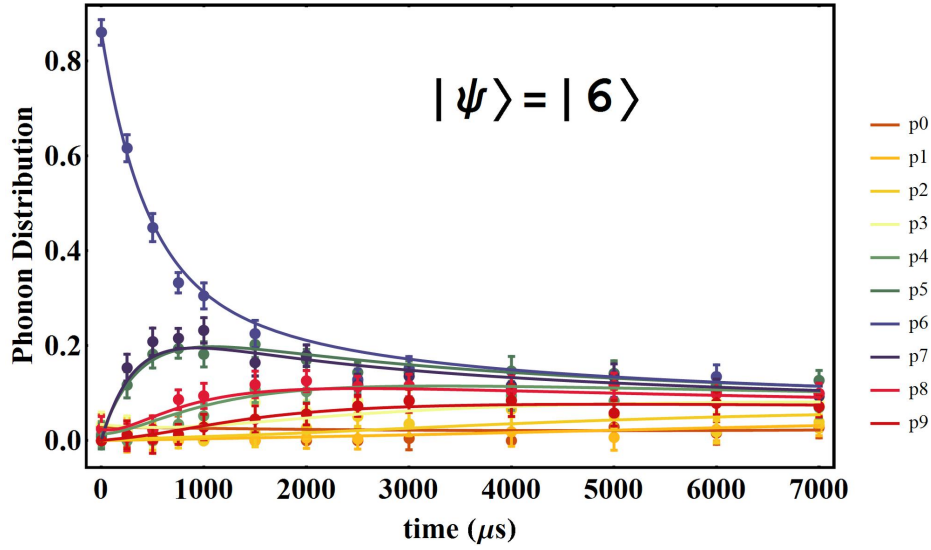


Fig. 5.1 The $|n\rangle = |6\rangle$ thermalization under the natural reservoir. The theory curve is predicted from Eq.3.44. It proves Eq.3.44 describes the natural environment well.

cooling at the condition of 3.1MHz trap frequency. By simply waiting, the environment noise will heat the ion. This process should be described by Eq.3.44. But all the previous reports in the trapped system is just from the engineered thermal reservoir [53]. So we conduct the number state heating test as showed in Fig. 5.1. It prove the environment is a thermal reservoir. According to the numerical simulation, we know if the state starts from a vacuum state and experience the thermal reservoir, the state will always be thermal state. By waiting for 1ms, we get the thermal state of average phonon of 0.157 as showed in Fig. 5.2. We measure the phonon with the blue sideband fitting and the projective measurement, which will be introduced in the next subsection.

5.3 Phonon projective measurement

The projective measurement is the key to realize the two point measurement of the quantum work [51]. In most situation the projective measurement for the spin is relatively easy. For other quantum observables, it is not always that easy. The photon QND projective measurement was realized by Serge Haroche [54]. The phonon projective measurement we use here was proposed for the Boson sampling problem at first [55]. The basic operation is

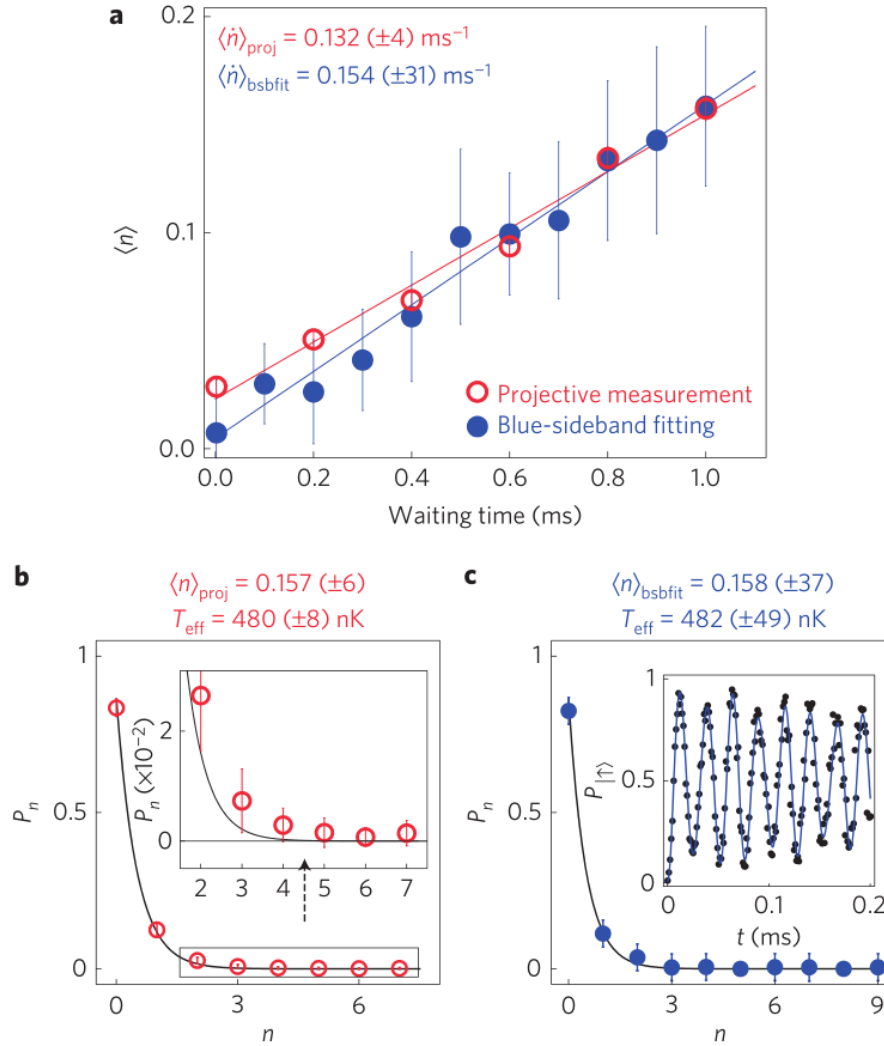


Fig. 5.2 Thermal state preparation of phonon and measurement results. (a) Measurements on heating rate of trapped ion's harmonic motion in X -direction. After the ground state cooling, the average phonon number increases linearly with the waiting time. The temperature is extracted from the average phonon number \bar{n} by $T_{\text{eff}} = \hbar\nu/k_B \ln(1 + 1/\bar{n})$, where ν is effective trap frequency. The projective measurements on the phonon states (red circles) are performed at various waiting time and the results are compared to those from the phonon-distribution measurement based on the dependence of the blue-sideband Rabi frequency on the phonon number (filled blue circles). The measured heating rate by phonon projection is consistent with that by fitting the blue-sideband transition within error bars. (b) The phonon distribution (red circles) measured by projective measurement at 1 ms waiting time, fitted by thermal distribution function $P_n^{\text{th}} = \bar{n}^n / (\bar{n} + 1)^{n+1}$ (solid line). The error bars are standard deviation. (c) The phonon distribution at 1 ms obtained by fitting the data in the inset with a superposition of Fock states (filled blue circles) and by a thermal distribution with \bar{n} (solid line). The error bars come from the one standard deviation in parameter estimations of the fitting.

showed in Fig. 5.3. We use the carrier, adiabatic blue sideband and detection to transfer the phonon projective measurement to the spin projective measurement. One problem of the scheme showed here is that if we use the bright state for the spin detection, after the detection the spin up state can be distributed to other Zeeman levels. To overcome this problem, we can use adiabatic red sideband and carrier to do the same work. To project $n = 0$, we apply adiabatic red sideband then detection. If we see the dark count, the state is projected to $n = 0$. To project $n = 1$, we apply adiabatic red, carrier and adiabatic red then detection. When it is bright, the state is larger than 1. If we detect the dark count, the initial $n = 1$ goes to 0 now and the initial 0 goes to 1. Then we apply another adiabatic red sideband and detection. If it is dark, we project to the original $n = 1$ by preparing $n = 1$ from $n = 0$. The probability of $n = 1$ is $P_1 = D_1 D_2$. For $n = 2$, we apply adiabatic red, carrier, adiabatic red, carrier and adiabatic red then detection. When we see the dark count, the state is projected to $n \leq 2$. Then we apply one adiabatic red sideband and detection. If it is dark, we project to the initial $n = 2$ by preparing $n = 2$ from $n = 0$ unitarily. The state is not destroyed by the detection in this way. The disadvantage is that the post selection process decreases the efficiency. In the adiabatic blue sideband method, every count result has its meaning. In experiment, we find the result of these two methods are almost the same.

The most important technique is the adiabatic motional sideband. The waveforms we use to realized it is showed in Fig. 5.4. To reduce the duration required by the adiabatic operation, we use the transition-less driving theory [56, 57] and add a small amount of σ_y component in the driving filed. The idea behind it is not that difficult. When we change the Hamiltonian adiabatically and change to the instantaneous framework, we can get the instantaneous Hamiltonian. If the speed is not infinitesimal, despite the energy eigen-Hamiltonian we get more terms. The diagonal terms will contribute to the famous Berry phase. The non-diagonal terms will introduce the non-adiabatic transitions. To reduce this excitation, we can add an auxiliary filed called the counter-diabatic Hamiltonian H_{CD} with an opposite sign with the non-diagonal terms to cancel them out. By change back to the lab framework, we know what the H_{CD} we should apply in the lab framework. Now let us derive. The time dependent

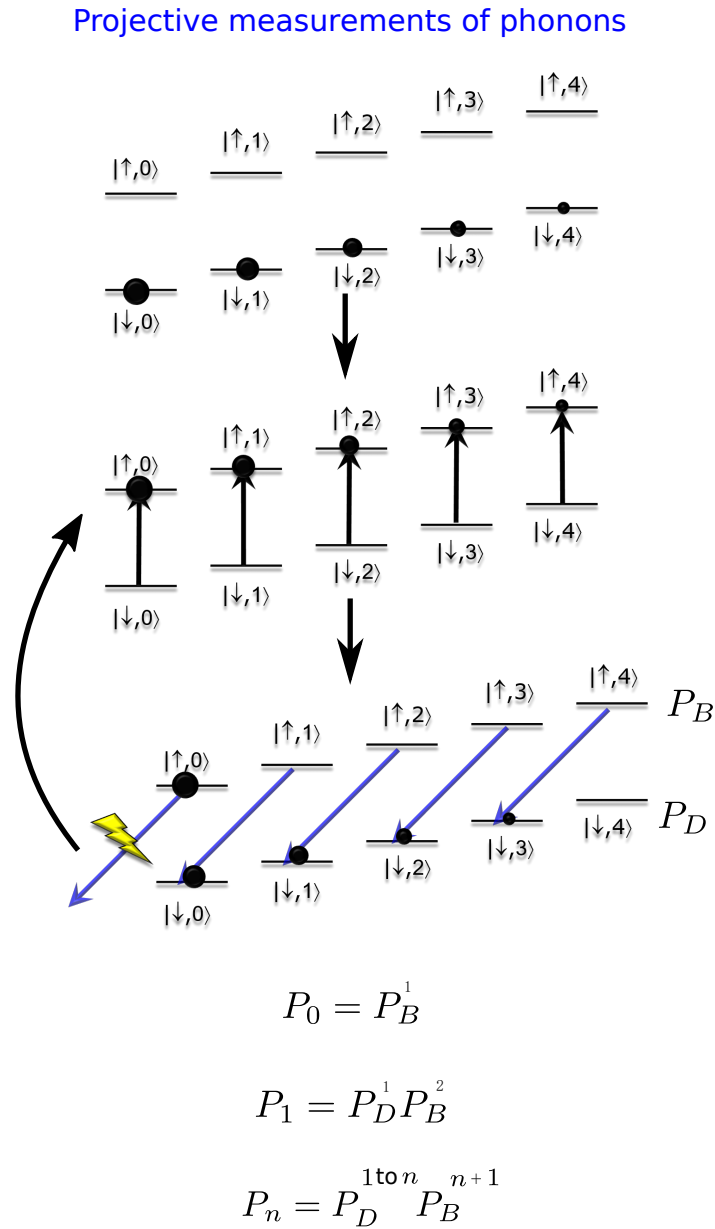


Fig. 5.3 The phonon projective measurement. We use the carrier and adiabatic blue sideband together to realize the phonon projective measurement. The probability of the phonon state n is $P_n = P_D^{n-1} P_B$. After the first bright detection, we reverse the whole sequence to prepare the $|n\rangle$ state.

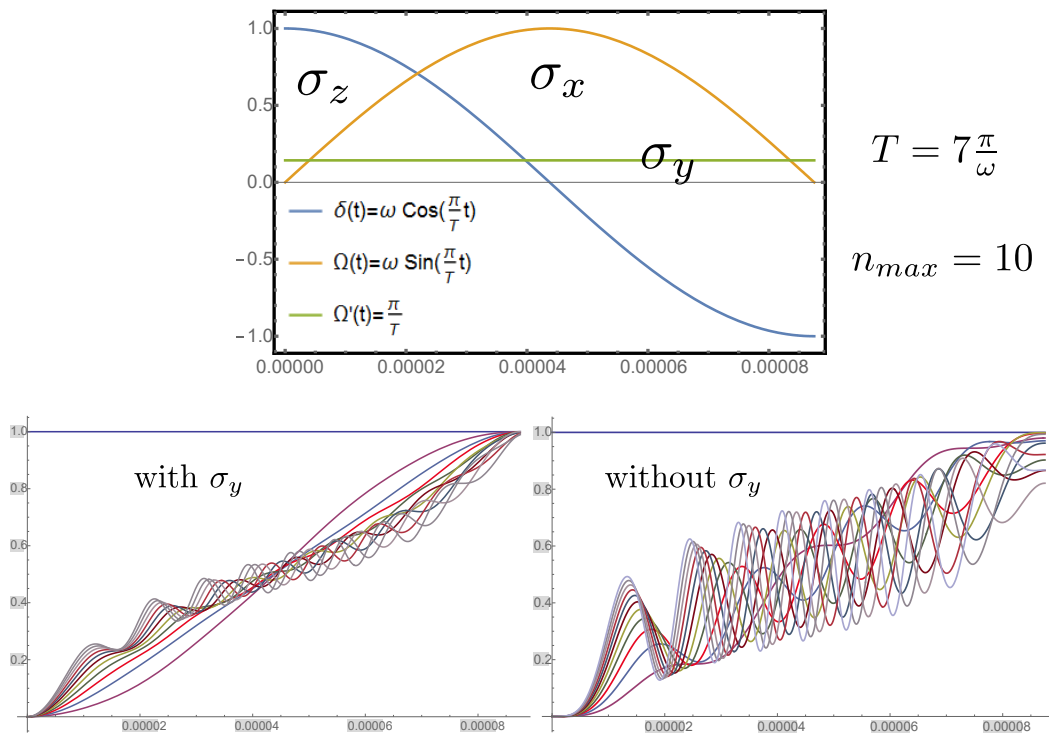


Fig. 5.4 The adiabatic blue sideband. We use the cos and sin waveform to change the Hamiltonian adiabatically. The state will follow the Hamiltonian. In this way we compensate the different Rabi frequency for different $|n\rangle$. The problem of this simple way is the long duration. If we just use 7 times of dynamical blue π duration, the fidelity will drop to 80% for $|10\rangle$. If the duration is too long, the heating and decoherence will destroy the state we want to measure. To solve this problem, we add a small amount of σ_y . It will cancel out a lot of the non-adiabatic transition. Up to $|10\rangle$, the fidelity in experiment is larger than 98%.

Hamiltonian H_0 and its eigen-state is

$$H_0(t)|n(t)\rangle = E_n(t)|n(t)\rangle. \quad (5.6)$$

When we apply $H_0(t)$ adiabatically, the evolution is

$$i|\dot{\psi}_n(t)\rangle = H_0|\psi_n(t)\rangle. \quad (5.7)$$

Berry points out the relation between $|\psi_n(t)\rangle$ and $|n(t)\rangle$. If we assume

$$|\psi_n(t)\rangle = \exp\left(-i \int E_n(t') dt'\right) \exp(i\gamma_n(t)) |n(t)\rangle \quad (5.8)$$

and insert it into Eq. 5.7, we can easily find

$$|\psi_n(t)\rangle = \exp\left(-i \int E_{n'}(t') dt' - \int \langle n(t') | \dot{n}(t') \rangle dt'\right) |n(t)\rangle. \quad (5.9)$$

We can find a new Hamiltonian $H(t)$ that can generate the dynamic solution of $|\psi_n(t)\rangle$.

Considering

$$H(t) = i\dot{U}(t)U^\dagger(t) \quad (5.10)$$

and

$$U(t) = \sum_n \exp\left(-i \int E_n(t') dt' - \int \langle n(t') | \dot{n}(t') \rangle\right) |n(t)\rangle \langle n(0)|, \quad (5.11)$$

we can get

$$H(t) = \sum_n E_n |n(t)\rangle \langle n(t)| + i \sum_n (\langle \dot{n}(t) | \langle n(t) | - |n(t)\rangle \langle \dot{n}(t) | n(t)\rangle \langle n(t) |) \equiv H_0 + H_1. \quad (5.12)$$

The derivation looks not that convenient. Considering

$$\langle m | \dot{n} \rangle = \frac{\langle m | \dot{H}_0 | n \rangle}{E_n - E_m}, \quad (5.13)$$

we can get a simple for of H_1 as

$$H_1 = i \sum_{m \neq n} \frac{|m\rangle\langle m|\dot{H}_0|n\rangle\langle n|}{E_n - E_m}. \quad (5.14)$$

For two level system, it is not that difficult to get the waveforms we use in experiment.

5.4 Applying work with spin dependent force and the fast effective adiabatic ramp

After determining and preparing the projected energy eigenstate $|n\rangle$, we apply work to the system. We apply the laser-induced force of Eq.3.16 on the prepared state for durations of $5\mu\text{s}$, $25\mu\text{s}$ and $45\mu\text{s}$ with a linearly increasing strength to the same maximum value, as shown in Fig. 5.5. We already prepare the spin on the eigen state of σ^x and the spin part can be traced out. Here in order to drag the harmonic oscillator, we add a detuning ν on this force. The interaction in th lab framework is

$$H(t) = \frac{\eta\Omega(t)}{2} \left(ae^{-i\nu t} + a^\dagger e^{i\nu t} \right). \quad (5.15)$$

Then we change to laser frequency framework, the interaction is

$$H(t) = \nu(a^\dagger a + 1/2) + \frac{\eta\Omega(t)}{2} \left(a + a^\dagger \right). \quad (5.16)$$

This is the dragged harmonic oscillator model.

After the work process, we need another phonon measurement to realize the two point measurement to get the quantum work. However when the spin dependent force laser is on, we can not measure. We add another adiabatic process to transform back to the lab framework and turn off the forcing laser. Traditionally such process may require tens of the oscillating periods. In experiment, we find when we reduce the force linearly in the duration of integral times of the oscillating period, this process is also an effective adiabatic process. The same phenomenon has been found in the cold atoms and real space ion transport experiment

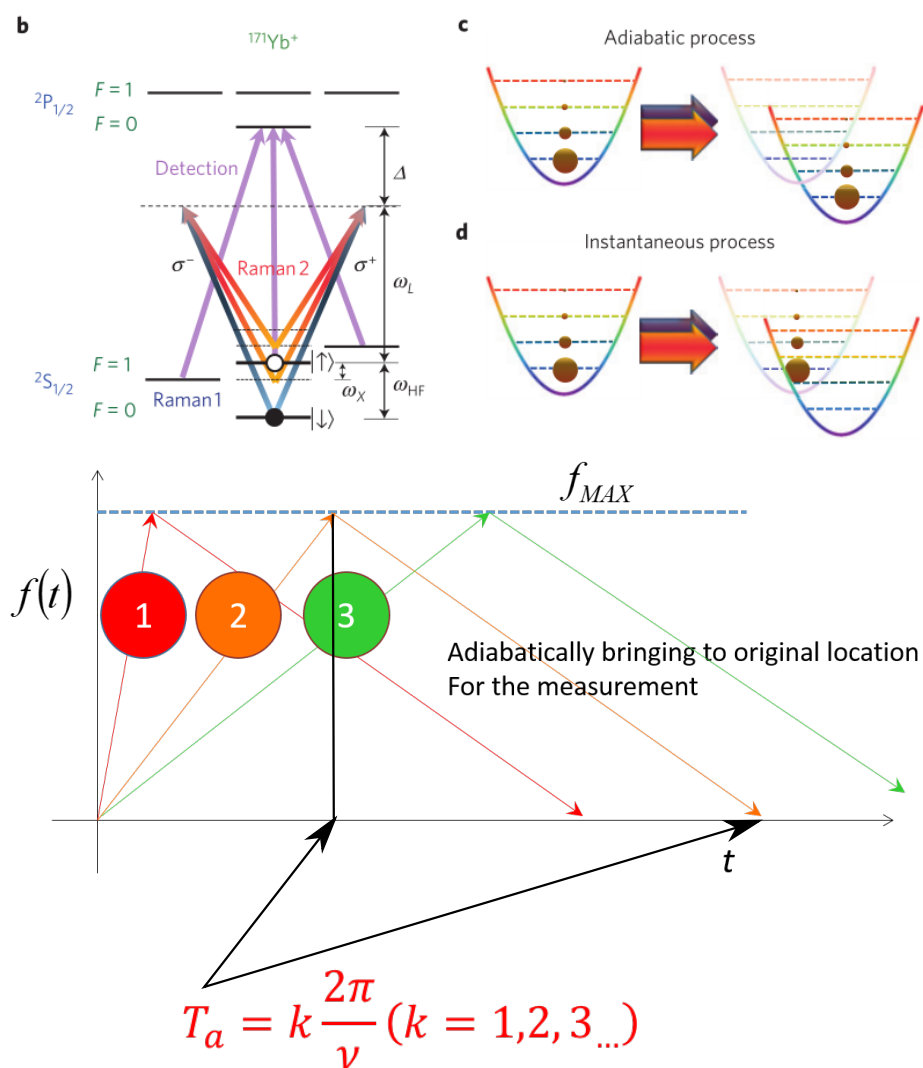
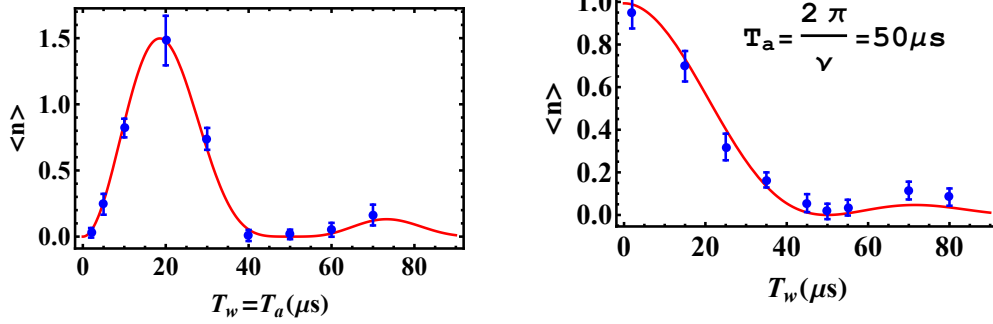


Fig. 5.5 The waveforms used to apply the work and the adiabatic transformation. We apply the laser-induced force on the prepared spin eigen state for durations of $5\mu\text{s}$, $25\mu\text{s}$ and $45\mu\text{s}$ with a linearly increasing strength to the same maximum value.



(a) Average phonon v.s. $T_w = T_a$. The red solid line is the prediction from equation 5.17.

(b) The real experiment process: T_w changes with $T_a = 50 \mu s$ fixed. The theory result for $T_a = +\infty$ and $k \frac{2\pi}{\nu}$ ($k = 1, 2, 3 \dots$) are the same red line.

Fig. 5.6 Test of the rapid adiabatic process.

[58, 59]. This can be explained by the time evolution of the whole experiment. We can express the time evolution in the form of displacement operator $D(\alpha) = \exp(\alpha \hat{a}^\dagger - \alpha^* \hat{a})$ (a common phase neglected). When we increase the laser intensity in T_w and decrease in T_a linearly, the displacement is

$$\alpha = -i \frac{\Delta k x_0 \Omega_{max}}{2} \left(\frac{e^{iT_w \nu} (1 - iT_w \nu) - 1}{T_w \nu^2} + \frac{e^{iT_a \nu} (1 - e^{iT_a \nu} + iT_a \nu)}{T_a \nu^2} \right) \quad (5.17)$$

where $\Omega_{max} = 2\pi \times 378$ kHz and the detuning $\nu = 2\pi \times 20$ kHz in our experiment. The first item is the displacement for the leading edge and the second for the falling edge. It is interesting that α is the same for $T_a = +\infty$ or $k \frac{2\pi}{\nu}$ ($k = 1, 2, 3 \dots$). As a consequence, if we set $T_a = \frac{2\pi}{\nu} = 50 \mu s$, we can change the frame about \hat{H}_0 to the lab frame rapidly without changing the phonon distribution. We test this rapid effective adiabatic process by fitting the coherent state generated by applying the force from vibrational ground state. We fit α or average phonon $\langle n \rangle = |\alpha|^2$ in two cases: change $T_w = T_a$ together or change T_w with $T_a = 50 \mu s$ fixed Fig. 5.6. The result is in line with Eq. 5.17. From Fig. 5.6a, we can see the ion's reaction clearly. At first, the pushing speed is too fast, the ion can not response immediately ($2 \mu s$). If we increase the T_w and T_a , the ion's displacement will be accumulated (5 and $10 \mu s$). After a maximal point ($20 \mu s$), the displacement will be accumulated destructively (30 and $40 \mu s$). When $T_w = T_a = \frac{2\pi}{\nu}$ ($50 \mu s$), the ion will be not

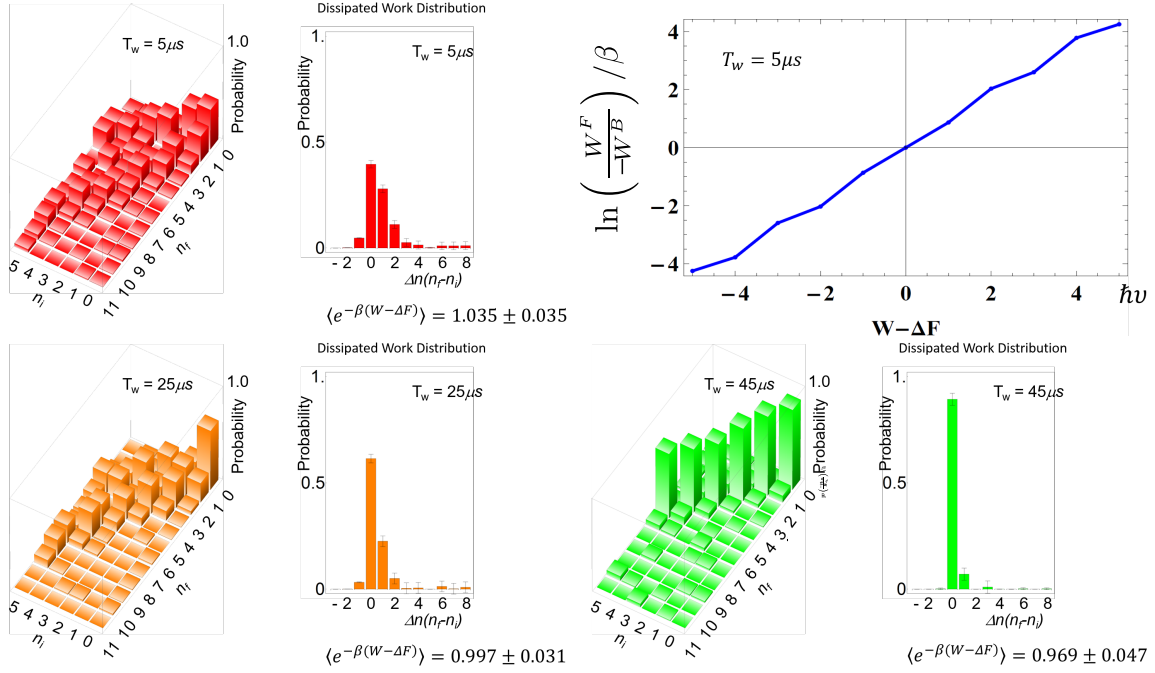


Fig. 5.7 The dissipated work distribution, the Jarzynski equality and Crooks relation results. We show only the Crooks relation for the fastest situation. Only in this situation, the work distribution is large enough compared with errors.

displaced at all. Some smaller excitations follow on. From Fig.5.6b, we see the faster pushing time T_w results in a larger phonon excitation within $50 \mu s$. We choose $T_w = 5, 25, 45 \mu s$ as the samples for the fastest, medium and slowest pushing speed in our experiment.

5.5 Work distribution, Jarzynski equality and the Crooks relation

The experimental work distribution, the Jarzynski equality and the Crooks relation results are showed in Fig. 5.7. When we consider the detailed fluctuation relation as Crooks relation, we need add a time reversed process. The work distribution for the forward and backword has a simple relation

$$\frac{P^F(W)}{P^B(-W)} = e^{-\beta(W-\Delta F)}. \quad (5.18)$$

This is the Crooks relation [60]. By integrate the backword process, we can easily get the Jarzynski equality. The Crooks relation has deep relation with the detailed balance principle. Its classical version has been tested in experiment [61]. To test quantum Crooks relation can deepen our understanding of the quantum fluctuation and thermal dynamics. In the dragged harmonic oscillator model, the for- and backword process have the same work distribution. We do not need to take the data for the backword process. We show only the result for the fastest dragging. Because the work distribution is wider, the signal noise ration is higher. The result still looks linear as in Fig. 5.7. When the work distribution is more condensed, the signal at the large work side will be dominated by experiment errors. The ration in the Crooks relation at large work will be strongly distorted by these errors. Because of the limited experimental precision and the special identical work distribution, we do not claim we have tested the quantum Crooks relation. However the linear relation showed at least shows our data quality is very good.

Chapter 6

Experimental realization of Shortcut to adiabaticity

The application of adiabatic protocols in quantum technologies is severely limited by environmental sources of noise and decoherence. As what we have seen in the previous chapter, the shortcut to adiabaticity is very important for the experiment. The next step for us is to study the adiabatic shortcut techniques more systematically [62]. Shortcuts to adiabaticity by counter-diabatic driving constitute a powerful alternative that speed up time-evolution while mimicking adiabatic dynamics. We present the first experimental implementation of counter-diabatic driving in a continuous variable system, a shortcut to the adiabatic transport of a trapped ion. The resulting dynamics is equivalent to a “fast-motion video” of the adiabatic trajectory. The robustness of this protocol is shown to surpass that of competing schemes based on classical local controls and Fourier optimization methods. In Fig. 6.1, we show a classical analog of the transition-less driving. We can use a counter-diabatic Hamiltonian to compensate the non-adiabatic transition. We can also notice that the counter-diabatic should be orthogonal to the adiabatic state of the original Hamiltonian. Thus the added counter-diabatic Hamiltonian will not introduce any quantum work in the system. We accelerate the adiabatic process without do work on the system. Such property makes the transitionless driving suitable for the quantum heat engine. It can be used to improved the efficiency and power of the quantum heat engine at the same time [63, 64].

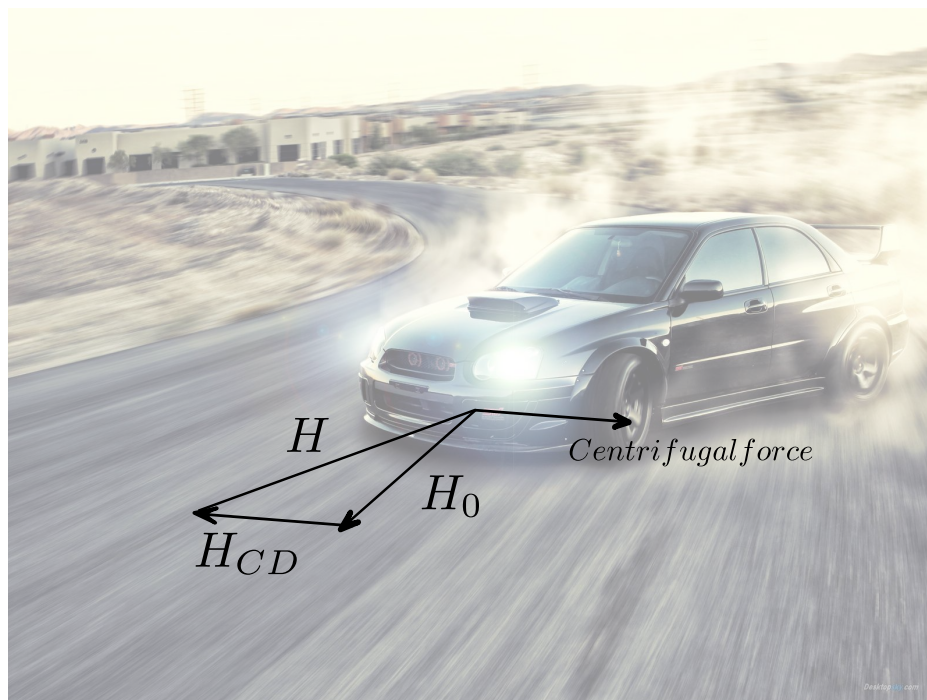


Fig. 6.1 The classical analog of adiabatic shortcut. When we drive and turn around a corner, if fast enough, we will feel a strong centrifugal force pushing us away from the trajectory. It is similar to the situation when we change the Hamiltonian and the non-adiabatic transition will make the state different from the adiabatic ground state of the Hamiltonian. In the classical situation, we compensate the centrifugal force by turn the direction of the car different from the trajectory we want to follow. In the transition-less driving, we add counter-diabatic Hamiltonian to the original Hamiltonian to compensate the non-adiabatic transitions.

6.1 Transport in the phase space

Different from the Jarzynski work, we use the spin independent force 3.11 to transport the ion in the phase space. We test and compare three different kinds of shortcuts including the transitionless driving. The comparison are showed in Fig.6.2. Similar as in the spin dependent force, we also add a detuning $\nu = 20\text{kHz}$ to the spin independent force

$$H = \frac{\eta\Omega}{2}(ae^{-i(\nu t+\phi)} + a^\dagger e^{i(\nu t+\phi)}). \quad (6.1)$$

Change to the laser frequency framework, we get the dragged harmonic hamiltonia

$$H'_x(t) = \frac{p^2}{2m} + \frac{1}{2}m\nu^2x^2 + f(t)x \quad (\phi = 0) \quad (6.2)$$

$$H'_p(t) = \frac{p^2}{2m} + \frac{1}{2}m\nu^2x^2 + h(t)p \quad (\phi = \pi/2) \quad (6.3)$$

We can add the momentum operator to the dragged harmonic oscillator by changing the relative phase of the Raman laser by $\pi/2$. Up to now we have all the operation needed in the following subsections.

6.2 Transitionless driving

The most important and the first proposed shortcut to adiabaticity is the transitionless driving. For the transport problem, we can get the counter diabatic Hamiltonian without using the general formula 5.14. When we transport the ion with force $f(t)$ as in Fig. 6.3, the Hamiltonian is

$$H_0 = \frac{p^2}{2m} + \frac{1}{2}m\nu^2x^2 + f(t)x. \quad (6.4)$$

The time evolution is defined as $D(\alpha)$, we can change to the instantaneous framework of H_0 with $U = D(-\alpha)$ and get the Hamiltonian in the instantaneous framework

$$H_U = UH_0U^\dagger + i\dot{U}U^\dagger = \frac{p^2}{2m} + \frac{1}{2}m\nu^2x^2 + \frac{\dot{f}(t)}{m\nu^2}p. \quad (6.5)$$

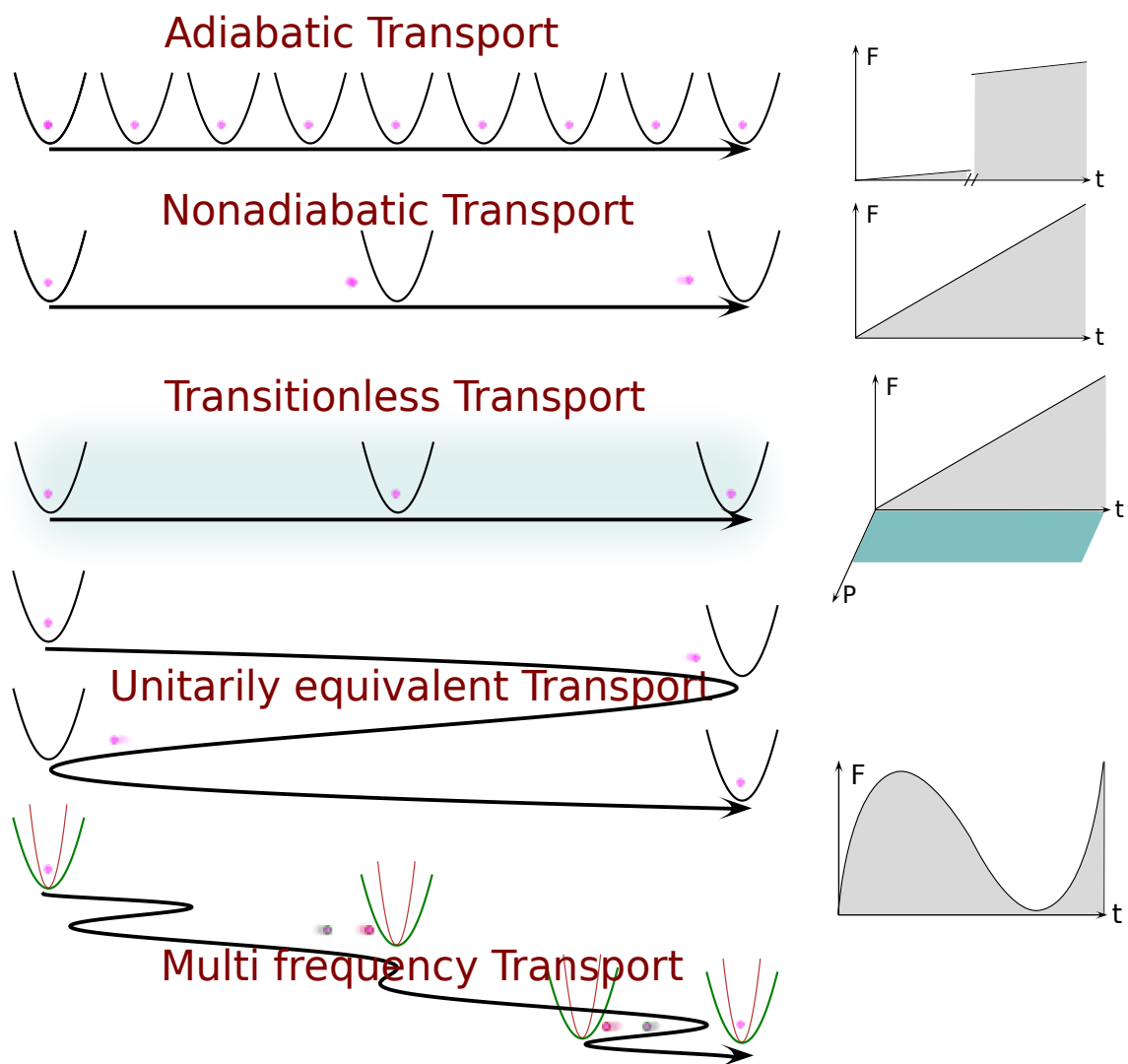


Fig. 6.2 The comparison between different transportation schemes.

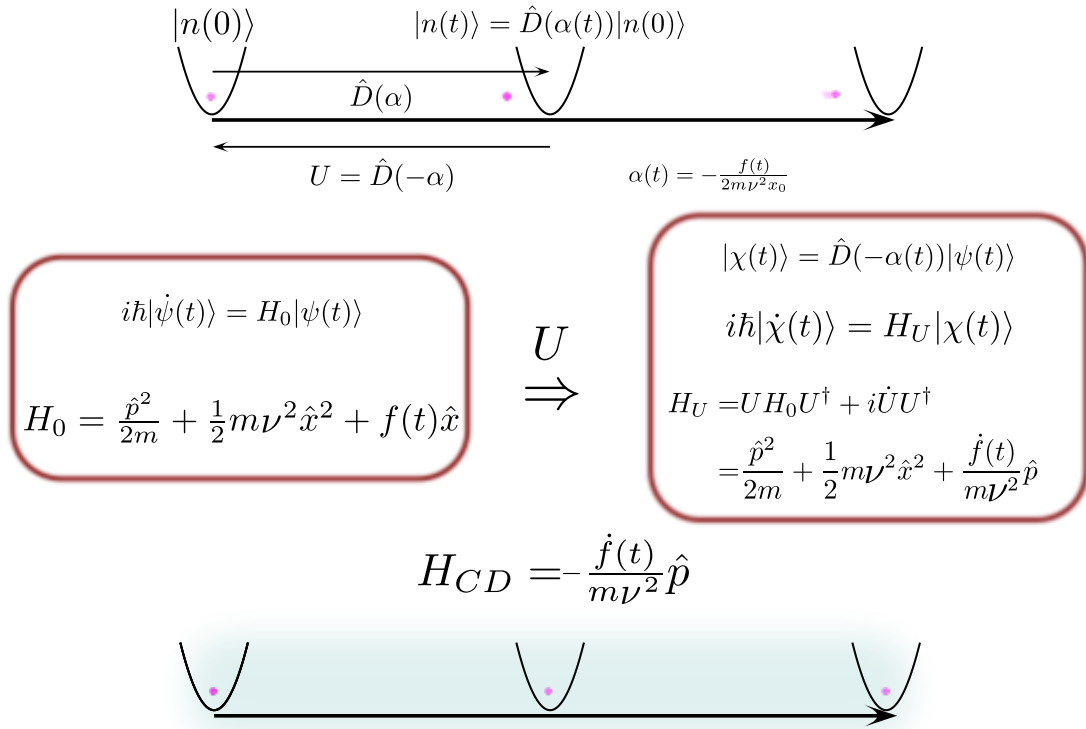


Fig. 6.3 The illustration for the transitionless transport.

The last term will introduce the non-adiabatic and disappear in the adiabatic limitation. We can add an auxiliary Hamiltonian to cancel it out. Because momentum operator is conserved under the transformation, we can find the counter-diabatic Hamiltonian

$$H_{CD} = -\frac{\dot{f}(t)}{mV^2}p. \quad (6.6)$$

6.3 Unitarily equivalent driving

The Hamiltonian we want to apply is

$$H = H_0 + H_{CD}. \quad (6.7)$$

However the momentum operator can not be realized in the lab with only electric filed, we solve this problem with an unitary transformation U . It should be a momentum shift

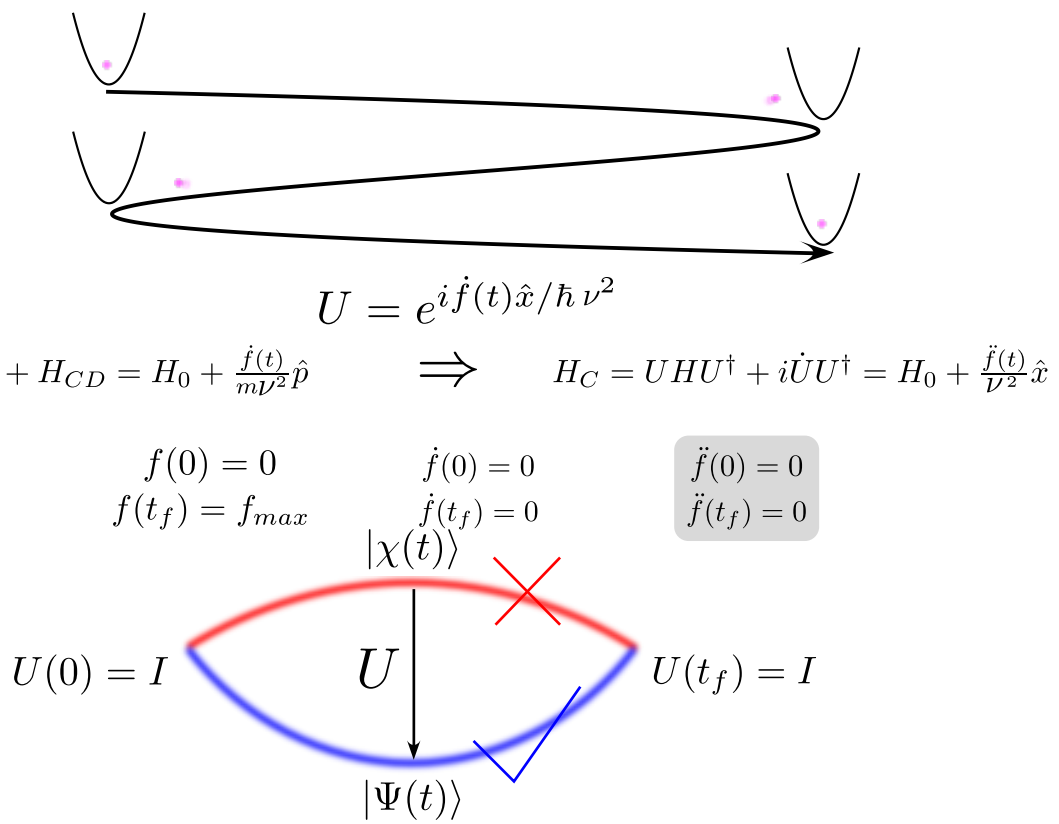


Fig. 6.4 The illustration for the unitarily equivalent transport.

operation

$$U = e^{ifx/v^2}. \quad (6.8)$$

After this transformation, we can get rid of the momentum term and obtain a new force term

$$H_C = H_0 + \frac{\dot{f}(t)}{v^2}x. \quad (6.9)$$

In the transformed framework, we can realize the transitionless driving with H_C in the lab framework. To get the ground state also in the lab framework, we should make sure

$$U(0) = \mathbf{I} \quad U(t_f) = \mathbf{I}, \quad (6.10)$$

which means the overlap between these two framework at the begin and the final points of the transport. Thus we have two groups of boundary conditions

$$f(0) = 0 \quad f(t_f) = f_{max} \quad (6.11)$$

$$\dot{f}(0) = 0 \quad \dot{f}(t_f) = 0. \quad (6.12)$$

Under these boundary conditions, we can construct the suitable waveforms of $f(t)$. Higher order boundary conditions can also be added to make the waveforms smoother as showed in Fig. 6.5. Fig. 6.5(d) shows the comparison of the robustness against the trap frequency errors for the case of $s = 1$. The robustness of the first order waveform is the best, which is consistent to the result in Ref. [65]. However, it requires the instantaneous switching of the control field, which is difficult in our experimental system. Therefore, we use the second order polynomial waveform in the experiment.

6.4 Multi-frequency driving

In this section we briefly describe the STA protocol based on the Fourier optimization scheme, which is well-explained in Ref. [66]. The method exploits the fact that when a force $f(t)$ is applied to a particle in the ground state from $f(0) = 0$ to $f(t_f)$ with the first order

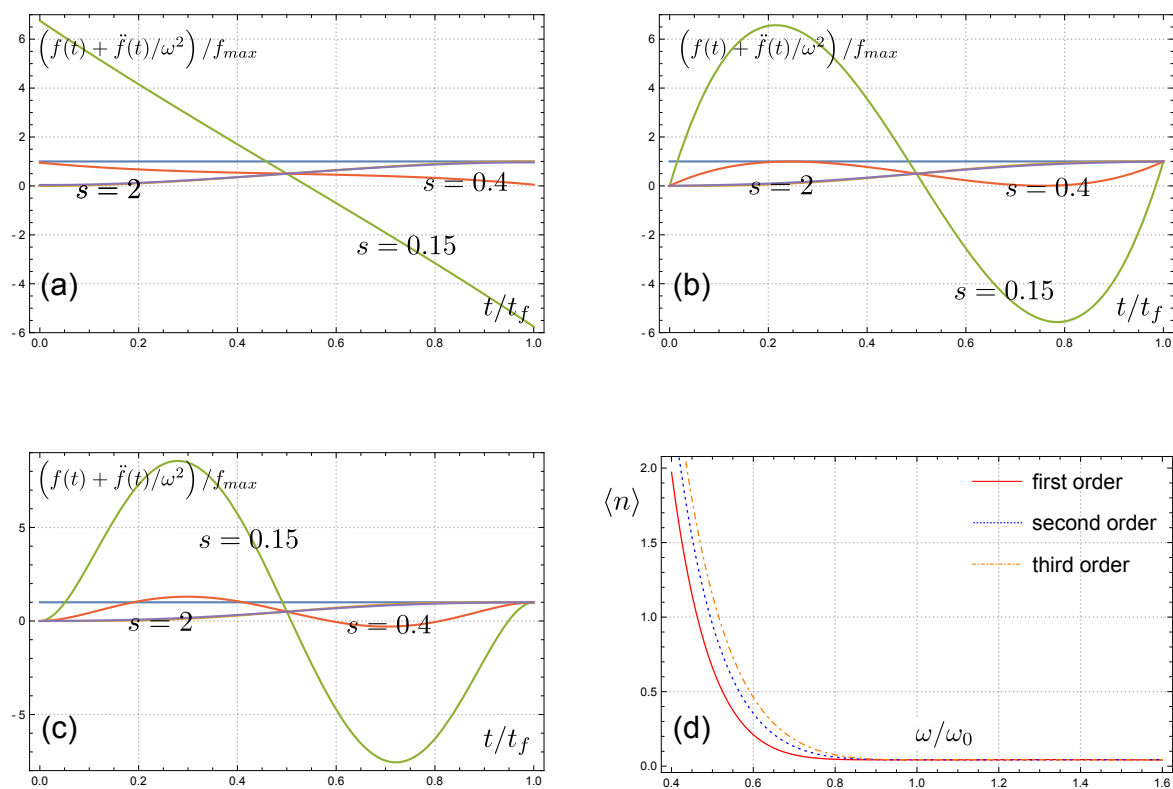


Fig. 6.5 Waveforms of (a) the first, (b) second and (c) third order polynomials and (d) their robustness against trap frequency errors. In (d), the robustness for different solutions against the trap frequency errors is compared for the case of $s = 1$.

boundary conditions $\dot{f}(0) = \dot{f}(t_f) = 0$, the final excitation energy is written by

$$\Delta E(\omega_0) = \left| \int_0^{t_f} \ddot{f}(t') e^{-i\omega t'} dt' \right| / m\omega^2, \quad (6.13)$$

where ω is the trap frequency. If we'd like to optimize the protocol for two-different trap frequencies ω_1, ω_2 , we have to minimize the excitation $\Delta E(\omega_1)$ and $\Delta E(\omega_2)$ with proper $f(t)$. If we set $\omega_1 = \omega_2 = \omega$, the robustness of the protocol against the trap frequency error is increased. An auxiliary function $g(t)$ is introduced to satisfy the following condition,

$$\ddot{f}(t) = \frac{d^4 g}{dt^4} + (\omega_1^2 + \omega_2^2) \frac{d^2 g}{dt^2} + \omega_1^2 \omega_2^2 g(t), \quad (6.14)$$

with the boundary conditions $g(0) = g(t_f) = \dot{g}(0) = \dot{g}(t_f) = \ddot{g}(0) = \ddot{g}(t_f) = \ddot{\ddot{g}}(0) = \ddot{\ddot{g}}(t_f) = 0$. Combining Eq. (6.13) and (6.14), we get

$$\Delta E(\omega) = \left| (\omega^2 - \omega_1^2)(\omega^2 - \omega_2^2) \int_0^{t_f} e^{-i\omega t'} g(t') dt' \right| \quad (6.15)$$

and find $\Delta E(\omega_1) = \Delta E(\omega_2) = 0$. Therefore, we can choose a polynomial function $g(t)$ to satisfy the boundary conditions for $g(t)$ as well as $f(t)$. For this kind of the order $N = 2$, we can choose $g(t) \propto (t/t_f)^4(1 - t/t_f)^4(1 - 2t/t_f)$. The technique can be generalized for the multiple frequency cases by satisfying the condition of $\Delta E(\omega_i) = 0$ for a set of frequencies $\{\omega_i | i = 1, \dots, N\}$. By setting these frequencies to be degenerate, the protocol exhibits an enhanced robustness against frequency errors with the order N . For the N -order case $g(t) \propto (t/t_f)^{2N}(1 - t/t_f)^{2N}(1 - 2t/t_f)$, from which one can derive $f(t)$. In our paper we show the waveform of order $N = 3$ for $s = 1.5$ due to the limitation of $f(t)/f_{max} < 1$. Here we compare waveforms of different values of N and their robustness against the trap frequency errors 6.6. We can see the maximum amplitude of the control field of this protocol is extremely sensitive to N and s . And for a fixed protocol duration a higher robustness can be achieved by increasing the amplitude of the control field.

As the final results, we test the instantaneous excitation and the robustness comparison for different waveforms in Fig. 6.7.

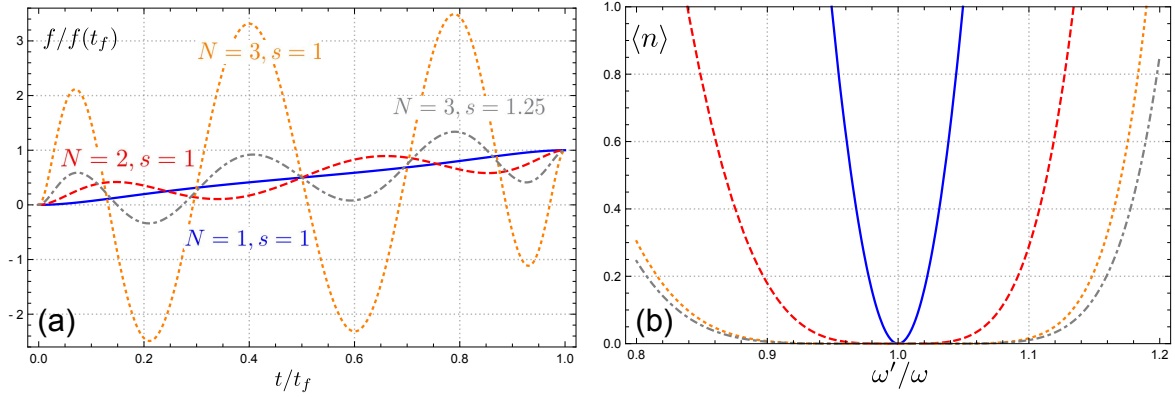
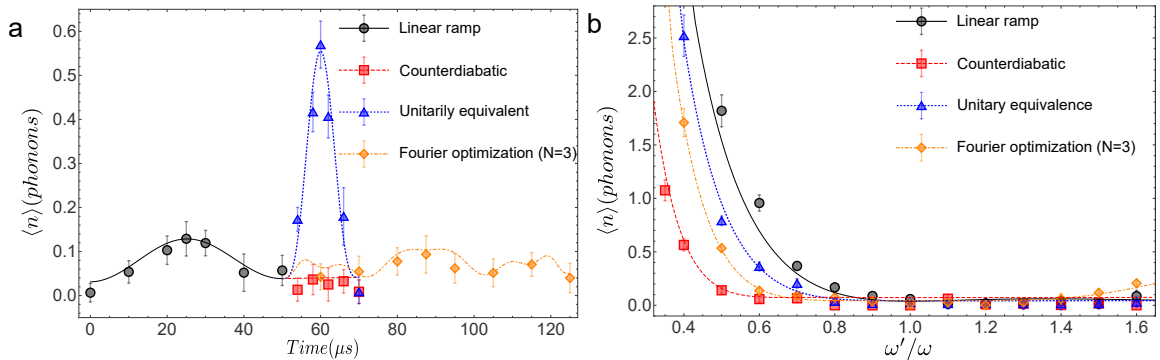


Fig. 6.6 Waveforms for the Fourier optimization scheme of different order N and their robustness against the trap frequency errors. (a) The maximum amplitude of $f(t)$ increases rapidly with the order N and decreases quickly with the shortcut ratio s . (b) With the same $s = 1$, the robustness would be better for a larger order N . With the same order $N = 3$, the robustness would be better for a larger shortcut ratio s .



(a) To measure non-adiabatic excitations during each STA, the shortcut waveform stops at a specific time and the system is transported back adiabatically to the initial position $q = 0$ (see section B of supplementary information). This process for the nominal trap frequency $\omega = 2\pi \times 20$ kHz brings phonon distributions back to the lab frame. Finally we measure the average values of excited phonons. Note that only the CD phonons. For a fair comparison, we set $s = 1.5$ realizes the adiabatic following.
 (b) To study the robustness of different STA protocols against the trap frequency drift, we change the trap frequency ω to ω' during the shortcut process. For a fair comparison, we set $s = 1.5$ for all three STA protocols.

Fig. 6.7 Phonon excitations in the instantaneous frame during different STA protocols and the robustness against trap frequency errors.

Chapter 7

Conclusion and outlook

In this thesis, I have show my effort to improve the quantum control ability both on the hardware side, such as the blade trap, and the software side including the phonon projective measurement, adiabatic shortcut and so on. We conduct the first experiment test of the quantum Jarzynski equality and realize the adiabatic shortcut in both spin and phonon system. Our work contributes some techniques to the trapped ion community. As the next step with our set up, there are several important directions we may go for as discussed bellow.

The first thing we can do easily is to check the fidelity measurement between two motional modes with the beam splitting operation 3.25. When two modes are the same, we get the purity. In experiment, this operation has been used to detect the entanglement entropy [67]. The beam splitting operation can also be used in the quantum thermal dynamics study. It can be used to connect a system to the environment.

Another direction we can pursue is the reservoir engineering 3.50. Up to now, the purely motional cat states are still not realized in experiment. If we can improve the motional coherence to a good enough condition or change to the axial modes, we should also try this. The cat code including the holonomic quantum controls should also be realized with this engineered reservoir. The beam splitting operation can be used to generate the entangled states for the cat codes.

The quantum Crooks relation up to now is still not tested with the projective work measurement. If we change from the dragged harmonic oscillator model to the trap frequency quench model, we should see different work distribution for the for- and backward processes.

The new entanglement scheme 3.1.7 can also be tested for different species or the same kind of ions. The requirement of this operation is similar as the Cirac-Zoller gate. We need the ground state cooling, and the individual ion addressing ability for the same kind of ions. If two different species, just ground state cooling is enough. But the operation itself is easier.

In an ion chain, if we just apply the same off-resonate motional sideband to two ions, their spin will be exchanged. Such spin exchange interaction 3.40 can also be used to realize the XY model. It is different from the existing method by increasing the effective magnetic field strength in the Ising model.

Finally, the most important thing is to scale up the number of ions we can manipulate well. The blade trap is a promising platform. To compensate the micro-motion along the axial direction should be the next step to get a stable ion chain with high trap frequency. The single ion addressing also should be considered. There are still a lot of things to do for successors and myself.

References

- [1] Warren Nagourney. *Quantum electronics for atomic physics and telecommunication*. OUP Oxford, 2014.
- [2] Dik Bouwmeester, Jian-Wei Pan, Klaus Mattle, Manfred Eibl, Harald Weinfurter, and Anton Zeilinger. Experimental quantum teleportation. *Nature*, 390(6660):575–579, 1997.
- [3] Thaddeus D Ladd, Fedor Jelezko, Raymond Laflamme, Yasunobu Nakamura, Christopher Monroe, and Jeremy L O’Brien. Quantum computers. *Nature*, 464(7285):45–53, 2010.
- [4] Iulia Buluta and Franco Nori. Quantum simulators. *Science*, 326(5949):108–111, 2009.
- [5] Rainer Blatt and CF Roos. Quantum simulations with trapped ions. *Nature Physics*, 8(4):277–284, 2012.
- [6] Juan I Cirac and Peter Zoller. Quantum computations with cold trapped ions. *Physical review letters*, 74(20):4091, 1995.
- [7] David P DiVincenzo et al. The physical implementation of quantum computation. *arXiv preprint quant-ph/0002077*, 2000.
- [8] Shlomi Kotler, Nitzan Akerman, Yinnon Glickman, Anna Keselman, and Roee Ozeri. Single-ion quantum lock-in amplifier. *Nature*, 473(7345):61–65, 2011.
- [9] Victor V Albert, Chi Shu, Stefan Krastanov, Chao Shen, Ren-Bao Liu, Zhen-Biao Yang, Robert J Schoelkopf, Mazyar Mirrahimi, Michel H Devoret, and Liang Jiang. Holonomic quantum control with continuous variable systems. *Physical review letters*, 116(14):140502, 2016.
- [10] Daoyi Dong and Ian R Petersen. Quantum control theory and applications: a survey. *IET Control Theory & Applications*, 4(12):2651–2671, 2010.
- [11] Wolfgang Paul. Electromagnetic traps for charged and neutral particles. *Reviews of modern physics*, 62(3):531, 1990.
- [12] Dietrich Leibfried, Rainer Blatt, Christopher Monroe, and David Wineland. Quantum dynamics of single trapped ions. *Reviews of Modern Physics*, 75(1):281, 2003.
- [13] Kilian Singer, Ulrich Poschinger, Michael Murphy, Peter Ivanov, Frank Ziesel, Tommaso Calarco, and Ferdinand Schmidt-Kaler. Colloquium: Trapped ions as quantum bits: Essential numerical tools. *Reviews of Modern Physics*, 82(3):2609, 2010.

- [14] Olmschenk Steven. *Quantum teleportation between distant matter qubits*. PhD thesis, University of Maryland, College Park, 2009.
- [15] JD Siverns, LR Simkins, S Weidt, and WK Hensinger. On the application of radio frequency voltages to ion traps via helical resonators. *Applied Physics B*, 107(4):921–934, 2012.
- [16] DJ Berkeland, JD Miller, JC Bergquist, WM Itano, and DJ Wineland. Minimization of ion micromotion in a paul trap. *Journal of applied physics*, 83(10):5025–5033, 1998.
- [17] Robert C Weast, Melvin J Astle, William H Beyer, et al. *CRC handbook of chemistry and physics*, volume 69. CRC press Boca Raton, FL, 1988.
- [18] JE Sansonetti, WC Martin, and SL Young. Handbook of basic atomic spectroscopic data, number 1.1. 2, national institute of standards and technology, gaithersburg, md, 2005.
- [19] C Ospelkaus, U Warring, Y Colombe, KR Brown, JM Amini, D Leibfried, and D-J Wineland. Microwave quantum logic gates for trapped ions. *Nature*, 476(7359):181–184, 2011.
- [20] U Warring, C Ospelkaus, Y Colombe, R Jördens, D Leibfried, and DJ Wineland. Individual-ion addressing with microwave field gradients. *Physical review letters*, 110(17):173002, 2013.
- [21] J David Jackson. *Electrodynamics*. Wiley Online Library, 1975.
- [22] Harold J Metcalf and Peter Van der Straten. *Laser cooling and trapping*. Springer Science & Business Media, 2012.
- [23] Shantanu Debnath. *A programmable five qubit quantum computer using trapped atomic ions*. PhD thesis, University of Maryland, College Park, 2016.
- [24] DF James and Jonathan Jerke. Effective hamiltonian theory and its applications in quantum information. *Canadian Journal of Physics*, 85(6):625–632, 2007.
- [25] PC Haljan, K-A Brickman, L Deslauriers, PJ Lee, and C Monroe. Spin-dependent forces on trapped ions for phase-stable quantum gates and entangled states of spin and motion. *Physical review letters*, 94(15):153602, 2005.
- [26] PJ Lee, KA Brickman, L Deslauriers, PC Haljan, LM Duan, and C Monroe. Phase control of trapped ion quantum gates. *Journal of Optics B: Quantum and Semiclassical Optics*, 7(10):S371, 2005.
- [27] MS Kim, Jinhyoung Lee, and William J Munro. Experimentally realizable characterizations of continuous-variable gaussian states. *Physical Review A*, 66(3):030301, 2002.
- [28] Anders Sørensen and Klaus Mølmer. Quantum computation with ions in thermal motion. *Physical review letters*, 82(9):1971, 1999.

- [29] C Senko, P Richerme, J Smith, A Lee, I Cohen, A Retzker, and C Monroe. Realization of a quantum integer-spin chain with controllable interactions. *Physical Review X*, 5(2):021026, 2015.
- [30] Philip Richerme, Zhe-Xuan Gong, Aaron Lee, Crystal Senko, Jacob Smith, Michael Foss-Feig, Spyridon Michalakis, Alexey V Gorshkov, and Christopher Monroe. Non-local propagation of correlations in quantum systems with long-range interactions. *Nature*, 511(7508):198–201, 2014.
- [31] Petar Jurcevic, Ben P Lanyon, Philipp Hauke, Cornelius Hempel, Peter Zoller, Rainer Blatt, and Christian F Roos. Quasiparticle engineering and entanglement propagation in a quantum many-body system. *Nature*, 511(7508):202–205, 2014.
- [32] Y Lin, JP Gaebler, F Reiter, TR Tan, R Bowler, AS Sørensen, D Leibfried, and DJ Wineland. Dissipative production of a maximally entangled steady state of two quantum bits. *Nature*, 504(7480):415–418, 2013.
- [33] Giovanna Morigi, Jürgen Eschner, Cecilia Cormick, Yiheng Lin, Dietrich Leibfried, and David J Wineland. Dissipative quantum control of a spin chain. *Physical review letters*, 115(20):200502, 2015.
- [34] Daniel FV James. Quantum dynamics of cold trapped ions with application to quantum computation. *Applied Physics B: Lasers and Optics*, 66(2):181–190, 1998.
- [35] Jonathon P Home. Quantum science and metrology with mixed-species ion chains. *Adv. At. Mol. Opt. Phys.*, 62:231, 2013.
- [36] LD Landau and EM Lifshits. Theoretical physics, vol. 1: Mechanics. *English translation, Pergamon Press, Book p*, 9099, 1988.
- [37] Marlan O Scully and M Suhail Zubairy. *Quantum optics*. AAPT, 1999.
- [38] DA Hite, Y Colombe, AC Wilson, KR Brown, U Warring, R Jördens, JD Jost, KS McKay, DP Pappas, D Leibfried, et al. 100-fold reduction of electric-field noise in an ion trap cleaned with in situ argon-ion-beam bombardment. *Physical review letters*, 109(10):103001, 2012.
- [39] DA Hite, Y Colombe, AC Wilson, DTC Allcock, D Leibfried, DJ Wineland, and DP Pappas. Surface science for improved ion traps. *MRS bulletin*, 38(10):826–833, 2013.
- [40] Daniel Kienzler, H-Y Lo, B Keitch, L de Clercq, F Leupold, F Lindenefelser, M Marinelli, V Negnevitsky, and JP Home. Quantum harmonic oscillator state synthesis by reservoir engineering. *Science*, 347(6217):53–56, 2015.
- [41] Hsiang-Yu Lo, Daniel Kienzler, Ludwig de Clercq, Matteo Marinelli, Vlad Negnevitsky, Ben C Keitch, and Jonathan P Home. Spin-motion entanglement and state diagnosis with squeezed oscillator wavepackets. *Nature*, 521(7552):336–339, 2015.
- [42] RL de Matos Filho and W Vogel. Even and odd coherent states of the motion of a trapped ion. *Physical review letters*, 76(4):608, 1996.

- [43] Andrew Chew. *Doppler-free spectroscopy of iodine at 739nm*. PhD thesis, The University of Michigan, 2008.
- [44] David J Hopper. *Investigation of laser frequency stabilisation using modulation transfer spectroscopy*. PhD thesis, Queensland University of Technology, 2008.
- [45] Michael W Lee, Marie Claire Jarratt, Christian Marciniak, and Michael J Biercuk. Frequency stabilization of a 369 nm diode laser by nonlinear spectroscopy of ytterbium ions in a discharge. *Optics express*, 22(6):7210–7221, 2014.
- [46] R Islam, WC Campbell, T Choi, SM Clark, CWS Conover, S Debnath, EE Edwards, B Fields, D Hayes, D Hucul, et al. Beat note stabilization of mode-locked lasers for quantum information processing. *Optics letters*, 39(11):3238–3241, 2014.
- [47] Yves Colombe, Daniel H Slichter, Andrew C Wilson, Dietrich Leibfried, and David J Wineland. Single-mode optical fiber for high-power, low-loss uv transmission. *Optics express*, 22(16):19783–19793, 2014.
- [48] JD Wong-Campos, KG Johnson, B Neyenhuis, J Mizrahi, and C Monroe. High-resolution adaptive imaging of a single atom. *Nature Photonics*, 10(9):606–610, 2016.
- [49] Shuoming An, Jing-Ning Zhang, Mark Um, Dingshun Lv, Yao Lu, Junhua Zhang, Zhang-Qi Yin, HT Quan, and Kihwan Kim. Experimental test of the quantum jarzynski equality with a trapped-ion system. *Nature Physics*, 2014.
- [50] Christopher Jarzynski. Nonequilibrium equality for free energy differences. *Physical Review Letters*, 78(14):2690, 1997.
- [51] Massimiliano Esposito, Upendra Harbola, and Shaul Mukamel. Nonequilibrium fluctuations, fluctuation theorems, and counting statistics in quantum systems. *Reviews of modern physics*, 81(4):1665, 2009.
- [52] Jan Liphardt, Sophie Dumont, Steven B Smith, Ignacio Tinoco, and Carlos Bustamante. Equilibrium information from nonequilibrium measurements in an experimental test of jarzynski’s equality. *Science*, 296(5574):1832–1835, 2002.
- [53] QA Turchette, CJ Myatt, BE King, CA Sackett, David Kielpinski, WM Itano, C Monroe, and DJ Wineland. Decoherence and decay of motional quantum states of a trapped atom coupled to engineered reservoirs. *Physical Review A*, 62(5):053807, 2000.
- [54] Christine Guerlin, Julien Bernu, Samuel Deleglise, Clement Sayrin, Sebastien Gleyzes, Stefan Kuhr, Michel Brune, Jean-Michel Raimond, and Serge Haroche. Progressive field-state collapse and quantum non-demolition photon counting. *Nature*, 448(7156):889–893, 2007.
- [55] Chao Shen, Zhen Zhang, and L-M Duan. Scalable implementation of boson sampling with trapped ions. *Physical review letters*, 112(5):050504, 2014.
- [56] Mustafa Demirplak and Stuart A Rice. Adiabatic population transfer with control fields. *The Journal of Physical Chemistry A*, 107(46):9937–9945, 2003.

- [57] MV Berry. Transitionless quantum driving. *Journal of Physics A: Mathematical and Theoretical*, 42(36):365303, 2009.
- [58] Antoine Couvert, T Kawalec, G Reinaudi, and David Guéry-Odelin. Optimal transport of ultracold atoms in the non-adiabatic regime. *EPL (Europhysics Letters)*, 83(1):13001, 2008.
- [59] R Bowler, J Gaebler, Y Lin, TR Tan, D Hanneke, JD Jost, JP Home, D Leibfried, and DJ Wineland. Coherent diabatic ion transport and separation in a multizone trap array. *Physical review letters*, 109(8):080502, 2012.
- [60] Gavin E Crooks. Entropy production fluctuation theorem and the nonequilibrium work relation for free energy differences. *Physical Review E*, 60(3):2721, 1999.
- [61] Delphine Collin, Felix Ritort, Christopher Jarzynski, Steven B Smith, Ignacio Tinoco, and Carlos Bustamante. Verification of the crooks fluctuation theorem and recovery of rna folding free energies. *Nature*, 437(7056):231–234, 2005.
- [62] Shuoming An, Dingshun Lv, Adolfo Del Campo, and Kihwan Kim. Shortcuts to adiabaticity by counterdiabatic driving for trapped-ion displacement in phase space. *Nature communications*, 7, 2016.
- [63] Jiawen Deng, Qing-hai Wang, Zhihao Liu, Peter Hänggi, and Jiangbin Gong. Boosting work characteristics and overall heat-engine performance via shortcuts to adiabaticity: Quantum and classical systems. *Physical Review E*, 88(6):062122, 2013.
- [64] Adolfo Del Campo, J Goold, and M Paternostro. More bang for your buck: Towards super-adiabatic quantum engines. *arXiv preprint arXiv:1305.3223*, 2013.
- [65] Hoi-Kwan Lau and Daniel FV James. Decoherence and dephasing errors caused by the dc stark effect in rapid ion transport. *Physical Review A*, 83(6):062330, 2011.
- [66] David Guéry-Odelin and JG Muga. Transport in a harmonic trap: Shortcuts to adiabaticity and robust protocols. *Physical Review A*, 90(6):063425, 2014.
- [67] Rajibul Islam, Ruichao Ma, Philipp M Preiss, M Eric Tai, Alexander Lukin, Matthew Rispoli, and Markus Greiner. Measuring entanglement entropy in a quantum many-body system. *Nature*, 528(7580):77–83, 2015.
- [68] Jacques Vanier and Claude Audoin. The quantum physics of atomic frequency standards. 1989.

Appendix A

Codes related with CPO

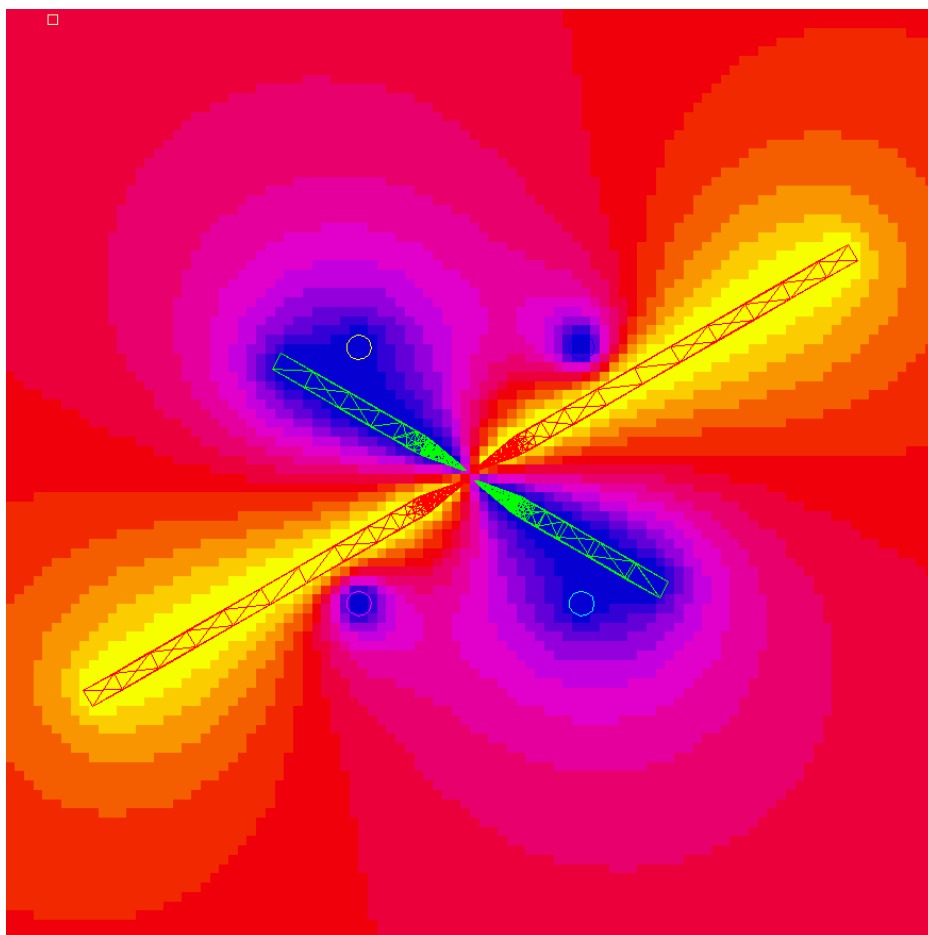


Fig. A.1 The potential of the blade trap.

The longer blades are the RF rods and the micromotion compensation bars are grounded.

To get the potential and field of the blade trap, we define the global constants at first.

```
Clear[mYb171, mYb174, mBa137, mBa138, e, QRF, dcorr];
mYb171 = QuantityMagnitude[IsotopeData["Ytterbium171", "AtomicMass"]] * 1.660538921 * 10-27;
mYb174 = QuantityMagnitude[IsotopeData["Ytterbium174", "AtomicMass"]] * 1.660538921 * 10-27;
mBa137 = QuantityMagnitude[IsotopeData["Barium137", "AtomicMass"]] * 1.660538921 * 10-27;
mBa138 = QuantityMagnitude[IsotopeData["Barium138", "AtomicMass"]] * 1.660538921 * 10-27;
e = 1.602176565 * 10-19;
dcorr = 10-3;
QRF = 2 π 30 * 106;
```

Then we take out the position of the nodes of the mesh generated by Comsol.

```
Clear[path1, path2, s, t, a, b, c];
path1 = "E:\\Inventor\\Shuoming\\Small2DBlade\\";
(*s = "rf.stl";*) (*s = "ground.stl";*) (*s = "dc1.stl";*) (*s = "dc2.stl";*)
(*s = "dc3.stl";*) (*s = "end1.stl";*) (*s = "end2.stl";*) (*s = "end3.stl";*)
(*s = "end4.stl";*) (*s = "trap.stl";*) (*s = "bar1.stl";*) (*s = "bar2.stl";*)
(*s = "bar3.stl";*) (*s = "bar4.stl";*) (*s = "rfwithbar.stl";*) (*s = "groundwithbar.stl";*)
s = "dcground.stl";
path2 = "C:\\cpo\\SIMU\\Shuoming\\SmallBlade\\";
(*t = "rf.dat";*) (*t = "ground.dat";*) (*t = "dc1.dat";*) (*t = "dc2.dat";*) (*t = "dc3.dat";*)
(*t = "end1.dat";*) (*t = "end2.dat";*) (*t = "end3.dat";*) (*t = "end4.dat";*) (*t = "trap.dat";*)
(*t = "bar1.dat";*) (*t = "bar2.dat";*) (*t = "bar3.dat";*) (*t = "bar4.dat";*) (*t = "rfwithbar.dat";*)
(*t = "groundwithbar.dat";*)
t = "dcground.dat";
a = ReadList[path1 <> s, Record,
RecordSeparators -> {"outer loop", "endloop", "vertex", "facet normal", "endfacet", "solid COMSOL mesh mesh1"}];
b = Table[{a[[7 n - 3]], a[[7 n - 2]], a[[7 n - 1]]}, {n, 1, (Length[a] - 2) / 7}];
c = StringJoin @@ Table[
(**) "triangle
<> \"\n\"
<> StringTrim[StringDrop[b[[n, 1]], -1]] <> " coner 1" <> "\"\n\"
<> StringTrim[StringDrop[b[[n, 2]], -1]] <> " coner 2" <> "\"\n\"
<> StringTrim[StringDrop[b[[n, 3]], -1]] <> " coner 3" <> "\"\n\"
<> (**) " 10 10 numbers of 2 applied voltages (can be same)" <> "\"\n\"
<> "1 number of subdivisions" <> "\"\n\"
<> (**) "colour 10" <> "\"\n\"
, {n, 1, Length[b]};
Export[path2 <> t, c, "TEXT"];
```

Finally we generate the file that CPO can use.

```

Clear[path, t, head, end, c];
path = "C:\\cpo\\SIMU\\Shuoming\\SmallBlade\\";
t = "Blade.dat";

head = "Default or template for CPO3D
c:\\cpo\\SIMU\\Shuoming\\SmallBlade\\Blade.t name of hidden output file, for processed data
c:\\cpo\\SIMU\\Shuoming\\SmallBlade\\Blade.txt name of main ray output file, for ray data
m bbbi n/p/m/a for print level, cumulative, blank comment start, colour electrodes
0 0 0 0 voltage reflection symmetries in x,y,z,x=y planes
9 number of different voltages (time-independent)
0.0001 20 0 allowed consistency error, side/length ratio check, allow outside zs
a apply inscribing correction (a/s/n=always/sometimes/never)";
end = "end of electrode information
0 1 0.5 final nmbr segs, nmbr steps, weight, disable overlap test
1e-07 charge inacc,non-0 total Q,improve matrix,import
end of segment information
1.000000E+00 rf
0.000000E+00 ground
0.000000E+00 dc1
0.000000E+00 dc2
0.000000E+00 dc3
0.000000E+00 end1
0.000000E+00 end2
0.000000E+00 end3
0.000000E+00 end4
0.000000E+00 dcground
n no more magnetic fields from menu
y y n potentials and fields along a line
0 0 -0.1 coordinates of initial end
0 0 0.1 coordinates of final end end
5 Number of points
1e-05 inaccuracy of evaluation
n n n no more potentials and fields along a line
no ray information
Default or template for CPO3D";
c =
head <> "\\n" <>
(*Import[path<>"rf.dat", "TEXT"]<>"\\n"<>
Import[path<>"ground.dat", "TEXT"]<>"\\n"<>
Import[path<>"dc1.dat", "TEXT"]<>"\\n"<>
Import[path<>"dc2.dat", "TEXT"]<>"\\n"<>
Import[path<>"dc3.dat", "TEXT"]<>"\\n"<>
Import[path<>"end1.dat", "TEXT"]<>"\\n"<>
Import[path<>"end2.dat", "TEXT"]<>"\\n"<>
Import[path<>"end3.dat", "TEXT"]<>"\\n"<>
Import[path<>"end4.dat", "TEXT"]<>"\\n"<>*)
Import[path<>"rfwithbar.dat", "TEXT"] <> "\\n" <>
Import[path<>"groundwithbar.dat", "TEXT"] <> "\\n" <>
end;
Export[path <> t, c, "TEXT"];

```

Here I show an example code for the effective potential of the blade trap(1V on the RF rods) in Fig. A.2. Only the pseudo potential is not enough for the real situation. In experiment, we add bias DC W on the ground blades. Its field should look like Fig. A.3. If we use the micro-motion compensation bars to correct the DC field, the simulated potential of one bar is showed in Fig. A.4. Now we can add the effective potential, the bias DC potential

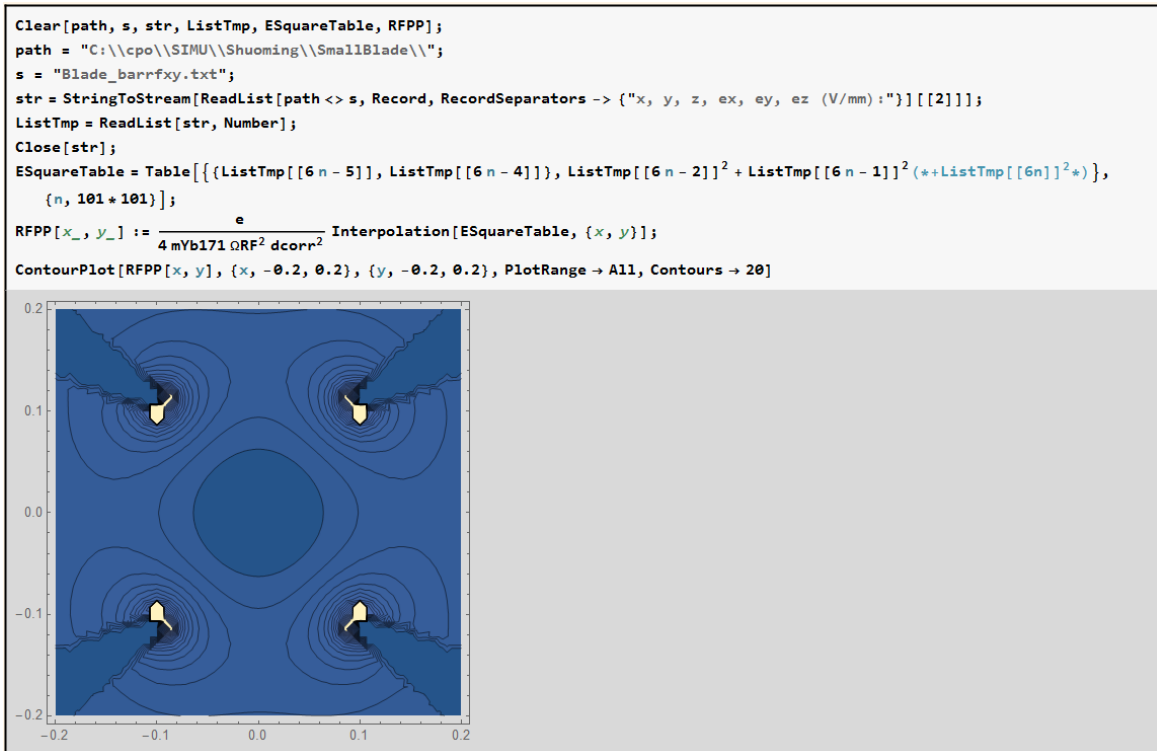


Fig. A.2 The effective potential calculated from the electric field simulated with CPO.

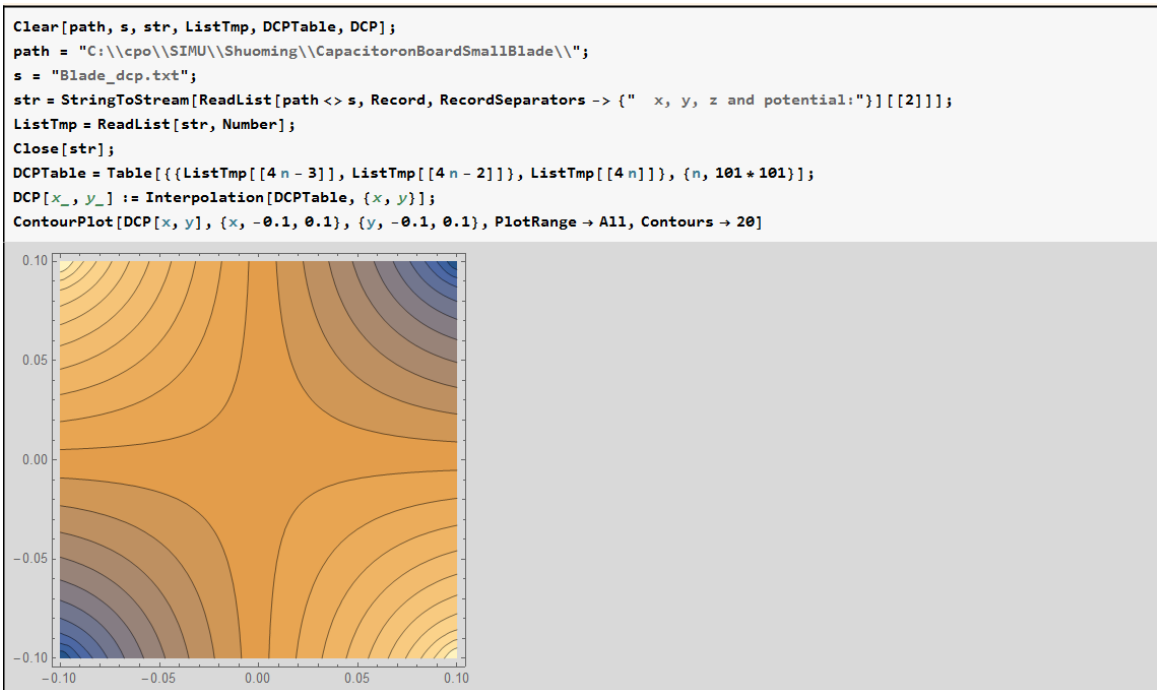


Fig. A.3 The potential generated by the bias DC on the ground blades.

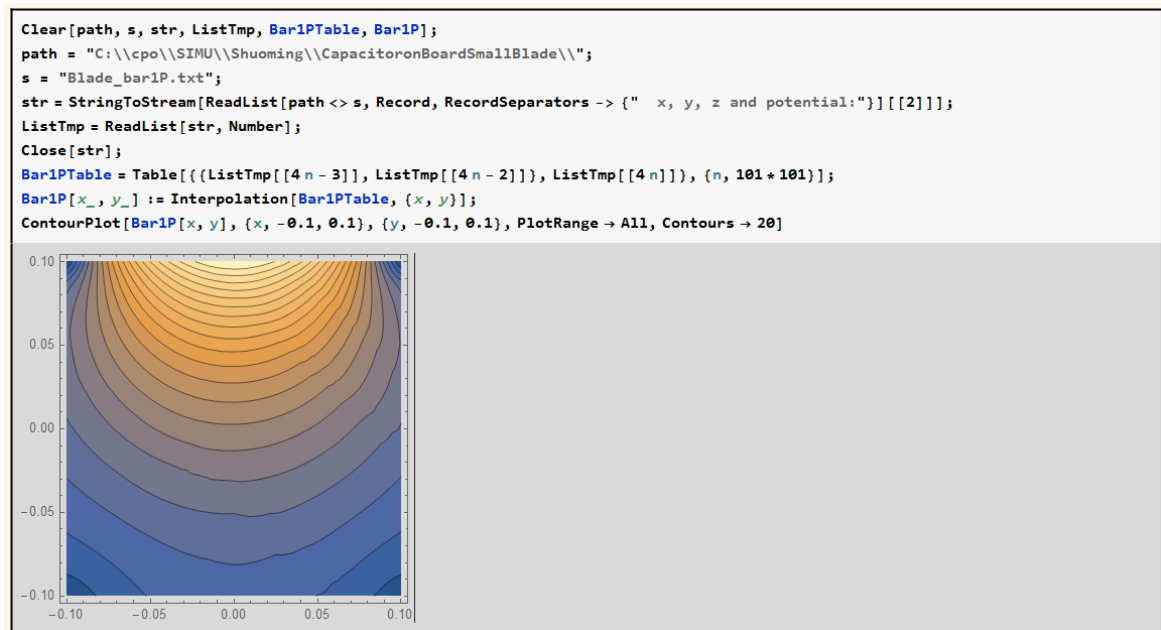


Fig. A.4 The potential generated by the micro-motion compensation electrodes.

and the micro-motion compensation potential together to get the whole potential. The codes in Fig. A.5 show how to get the ion position, the motional axis and the trap frequency. If necessary, we can simulate the potential generated from each DC section to get the effect of each DC section.

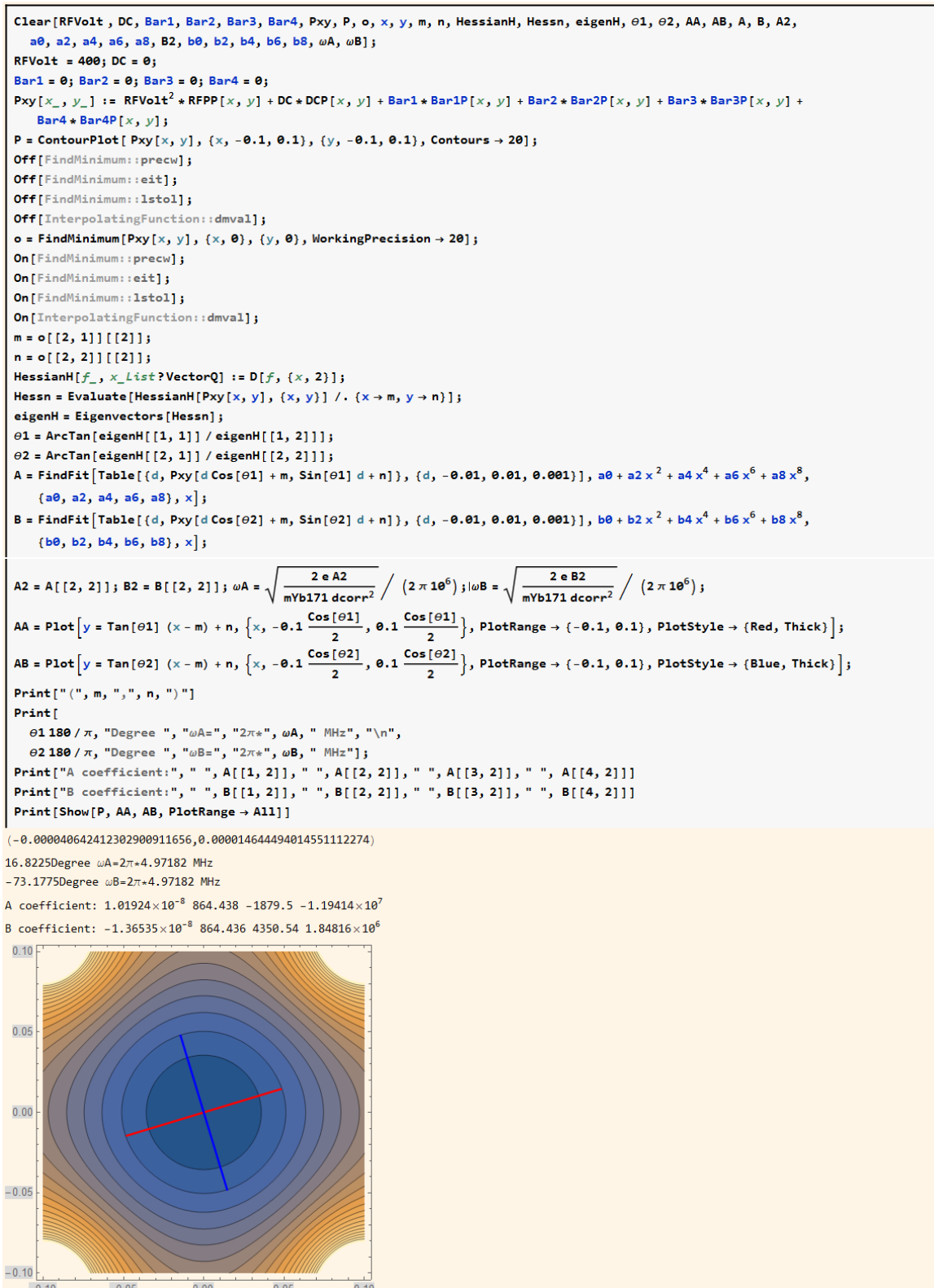


Fig. A.5 The codes and results of the final results of the CPO simulation.

Appendix B

Breit-Rabi-Zeeman splitting

When we apply the magnetic field, the Zeeman levels will separate. In the weak field situation, this is simply the Zeeman splitting. When the \mathbf{B} is large enough, the splitting is no longer linear. The exact formula is named after Breit-Rabi-Zeeman

$$E_{F=I\pm J}(m, B) = -\frac{H_F}{2(2I+1)} - g_I \mu_B m B / 10^4 \pm \frac{H_F}{2} \sqrt{1 + \frac{4m(g_J + g_I) \mu_B B / 10^4}{H_F(2I+1)} + \left(\frac{(g_J + g_I) \mu_B B / 10^4}{H_F} \right)^2}, \quad (\text{B.1})$$

Where the magnetic field B is in the unit of Gauss and all constants can be found in Ref. [68]. If the slope of the energy level is the same, the clock qubit is robust against the magnetic field up to the first order of B . Such intermediately field clock qubit have been reported for ${}^9\text{Be}^+$ and ${}^{43}\text{Ca}^+$. In our lab, we use ${}^{171}\text{Yb}^+$ and ${}^{137}\text{Ba}^+$. I also try to study whether we can also use this intermediately field to improve the coherence of the qubit. Here I will show the example code to calculate the energy levels and the magnetic field strength for the clock qubit. For ${}^9\text{Be}^+$, the code is showed in Fig. B.1. I try to search all the pairs of energy levels for the qubit. And try to find the lowest magnetic field for all the possible pair. We compare ${}^9\text{Be}^+$, ${}^{43}\text{Ca}^+$, ${}^{137}\text{Ba}^+$ and ${}^{171}\text{Yb}^+$ in Fig. . For ${}^{137}\text{Ba}^+$, the strength of the magnetic field is 767.875Gauss. It is relatively too high for us. For ${}^{171}\text{Yb}^+$, the strength of the magnetic field is 0Gauss. However, if $\mathbf{B} = 0$, the cooling for the ion will not work for the coherent

```

Clear[HF, II, gI, μB, gJ, EH, EL, BB];
HF = 6.62606957 × 10-34 × 1250017674. × 1; II =  $\frac{3}{2}$ ; gI = -0.42749 × 10-3; gJ = 2.0023; μB = 927.400968 × 10-26; BB = 300;
(*- when F=I-J;*) (*+ when F=I+J;*)
EH[m_, B_] :=  $\left( -\frac{HF}{2(2II+1)} - gI \mu B m \frac{B}{10^4} + \frac{1}{2} HF \left( 1 + \frac{4m}{2II+1} \frac{(gJ+gI) \mu B \frac{B}{10^4}}{HF} + \left( \frac{(gJ+gI) \mu B \frac{B}{10^4}}{HF} \right)^2 \right)^{1/2} \right) / (6.62606957 \times 10^{-34} \times 10^6)$ ;
EL[m_, B_] :=  $\left( -\frac{HF}{2(2II+1)} - gI \mu B m \frac{B}{10^4} - \frac{1}{2} HF \left( 1 + \frac{4m}{2II+1} \frac{(gJ+gI) \mu B \frac{B}{10^4}}{HF} + \left( \frac{(gJ+gI) \mu B \frac{B}{10^4}}{HF} \right)^2 \right)^{1/2} \right) / (6.62606957 \times 10^{-34} \times 10^6)$ ;
Print[Show[
  Plot[Evaluate[Table[EH[m, B], {m, -2, 2}], {B, 0, BB}], PlotRange → All, AxesOrigin → {0, 0}],
  Plot[Evaluate[Table[EL[m, B], {m, -1, 1}], {B, 0, BB}], PlotRange → All, AxesOrigin → {0, 0}]];
Print[Plot[EH[1, B] - EL[0, B], {B, -BB, BB}]];
Print[FindMinimum[EH[1, B] - EL[0, B], {B, -100}][[2, 1]]];

```

Fig. B.1 The code to calculate the energy levels and the magnetic field strength for the clock qubit. We consider ${}^9\text{Be}^+$ here. All the constant is founded in the book [68].

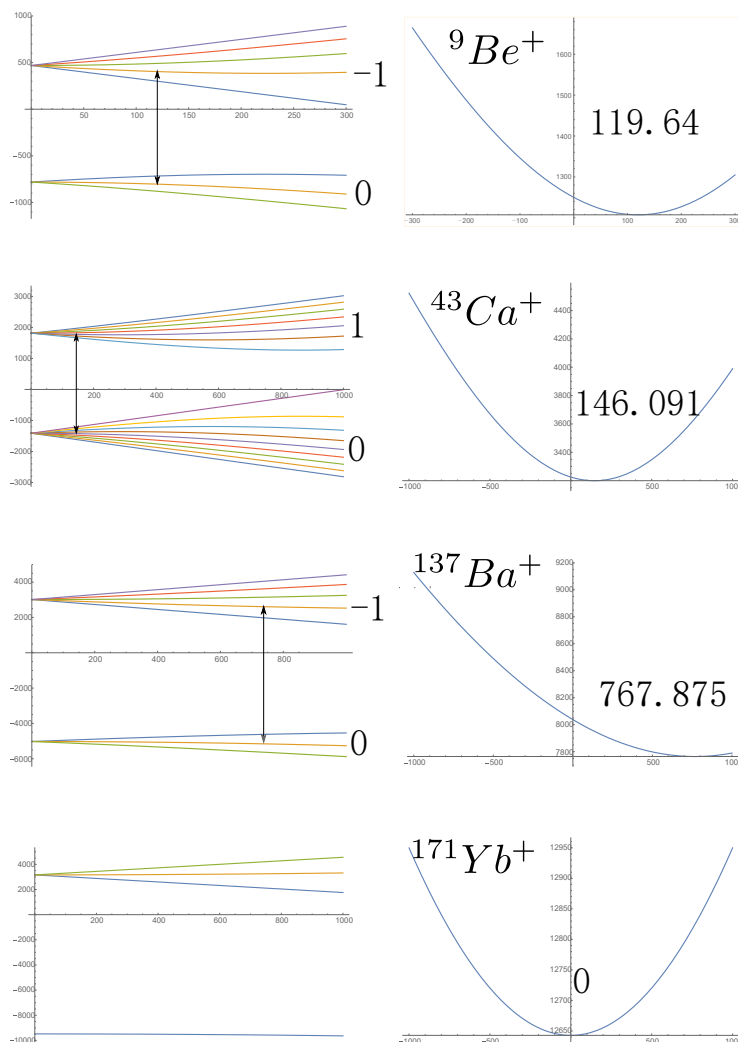


Fig. B.2 The energy level and the strength of the magnetic field for the clock qubit. The strength of \mathbf{B} field for ${}^9\text{Be}^+$, ${}^{43}\text{Ca}^+$, ${}^{137}\text{Ba}^+$ and ${}^{171}\text{Yb}^+$ are 119.64, 146.091, 767.875 and 0 Gauss respectively. The energy levels are in the unit of MHz.

population trapping between the Zeeman levels. We use 8Gauss in our experiment. Thus we can not realize the clock qubit in our lab.

Appendix C

Debye-Waller factor and the Lamb-Dicke parameter

In the Lamb-Dicke regime we expect the Rabi rate between $|\downarrow, n\rangle \rightarrow |\uparrow, n+1\rangle$ is

$$\Omega_{n,n+1} = \sqrt{n+1}\eta\Omega. \quad (\text{C.1})$$

This simple form is not the exact formula, because we only consider a^\dagger . The terms such as $a^i a^{\dagger(i+1)}$ will also contribute to this transitions. Only when $\eta \rightarrow 0$, which means the ion is an ideal point, the Eq. C.1 is exact. Now we try to give an exact formula for the Rabi rate. The interaction as Eq. 3.11 between the phonon and spin states is

$$\begin{aligned} \langle \uparrow, n' | H_{eff} | \downarrow, n \rangle &= \frac{\Omega}{2} e^{-i\delta t - i\phi} \langle n' | e^{i\eta(ae^{-i\omega t} + a^\dagger e^{i\omega t})} | n \rangle \\ &= \frac{\Omega}{2} e^{-i\delta t - i\phi} \sum_{j=0}^{\infty} \frac{\langle n' | (i\eta(ae^{-i\omega t} + a^\dagger e^{i\omega t}))^j | n \rangle}{j!}. \end{aligned} \quad (\text{C.2})$$

When $\delta = (n' - n)\omega + \nu$, only the proper oscillating terms are left with rotating wave approximation. It can be simplified as

$$\langle \uparrow, n' | H_{eff} | \downarrow, n \rangle = \frac{\Omega}{2} e^{-i\nu t - i\phi} \sum_{j=0}^{\infty} \frac{\langle n' | (i\eta(a + a^\dagger))^j | n \rangle}{j!} = \frac{\Omega}{2} e^{-i\nu t - i\phi} \langle n' | e^{i\eta(a + a^\dagger)} | n \rangle \quad (\text{C.3})$$

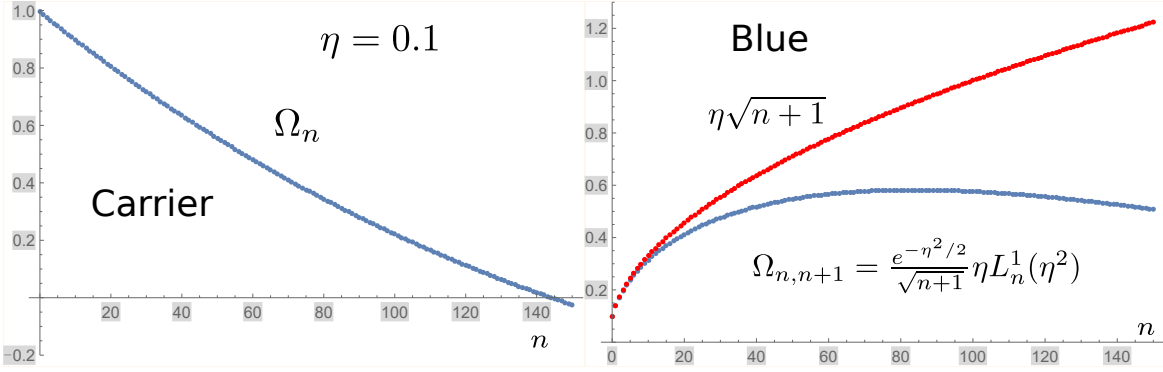


Fig. C.1 The Rabi rate dependence on the phonon number. For the carrier transition, we find when n is large enough, Ω_n can change the sign, For the blue sideband, we find when n is large enough, $\Omega_{n,n+1}$ can even be bent. Here we use the Lamb-Dicke parameter $\eta = 0.1$.

The Debye-Waller factor is

$$\langle n' | e^{i\eta(a+a^\dagger)} | n \rangle = D_{n',n}. \quad (\text{C.4})$$

Its explicit form is

$$D_{n',n} = e^{-\eta^2/2} \left(\frac{n_{<}!}{n_{>}!} \right)^{1/2} \eta^{|n'-n|} L_{n_{<}}^{|n'-n|}(\eta^2), \quad (\text{C.5})$$

where $n_{<}$ is the smaller one between n' and n and L_n^α is the associated Laguerre polynomial

$$L_n^\alpha(x) = \sum_{m=0}^{\infty} (-)^m C_{n+\alpha}^{n-m} \frac{x^m}{m!}, \quad (\text{C.6})$$

and $C_n^k = \frac{n!}{k!(n-k)!}$ is the Binomial coefficient. For the carrier transition, the phonon dependent Rabi frequency is

$$\Omega_n = \Omega e^{-\eta^2/2} L_n(\eta^2). \quad (\text{C.7})$$

For the blue sideband $n' = n + 1$, $\nu = 0$ and $\phi = 0$, the Rabi rate is

$$\Omega_{n,n+1} = \Omega \frac{\eta e^{-\eta^2/2}}{\sqrt{n+1}} L_n^1(\eta^2). \quad (\text{C.8})$$

The Rabi rate for the red sideband is similar as the blue sideband.

To test whether the ion motion is within the Lamb-Dicke regime and measure η , we generate number states up to $n = 20$ and compare the exact formula fitting with the approxi-

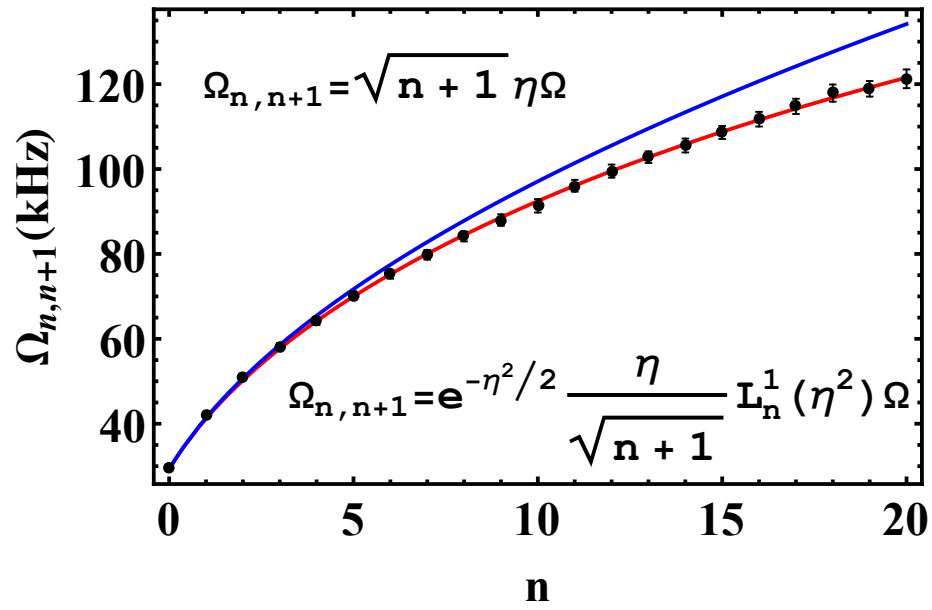


Fig. C.2 $\Omega_{n,n+1}$ for different n .

mation Fig. C.2. It is clear that the approximation holds for $n \leq 5$ and $\eta = 0.098$.

Appendix D

RF switch without dead time and the drawing of the invar confocal cavity

In the micro-motion compensation subsection, we switch the RF power between high and low power. Here I will show the illustration of the power switch we make without dead time in Fig.D.1. When we simply use the single-pole, double-throw switch (SPDT), there will be a dead time for the RF output, and the ion will disappear. When we use a two stage switch, the dead time is minimized and the ion can still be hold.

When we realize the PDH laser frequency lock, we use the invar cavity designed as showed in Fig. D.2. We also use it to monitor the laser spectrum.

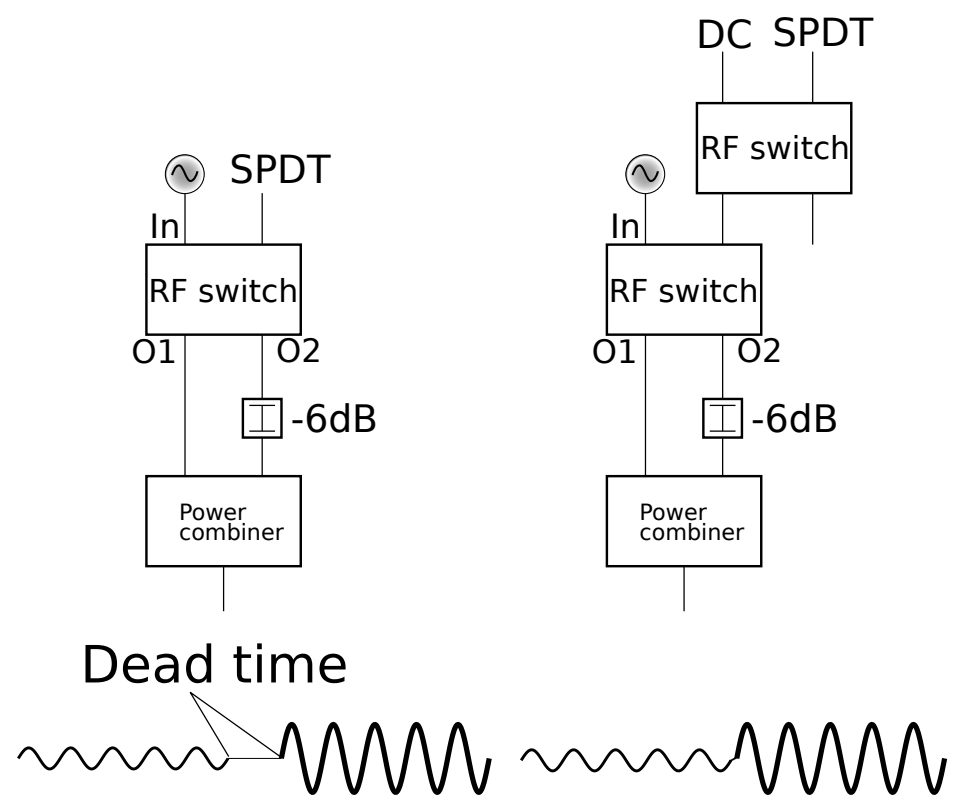


Fig. D.1 RF switch without dead time. SPDT is the single-pole, double-throw switch.

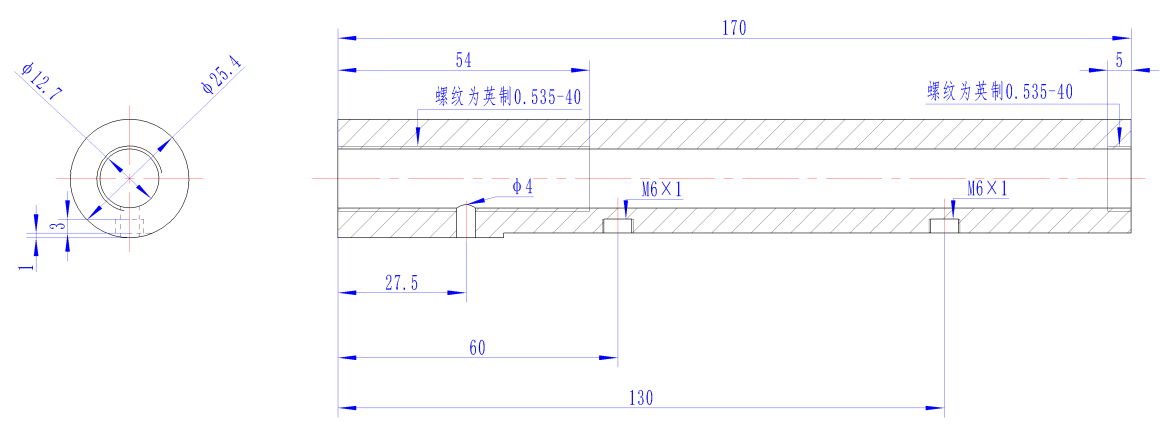


Fig. D.2 Invar confocal design used for PDH lock and F-P monitor.

Appendix E

The code used to calculate the position and mode structure of a mixed ion chain

As the first step, we should know the position of a mixed ion chain. In this code we just need to write down the mass of the ion in a list. For two Yb ion and one Ba ion from the left to right one by one, we should write $\{171, 171, 137\}$, the axial voltage V and the axial distance ρ in the corresponding place in the code in Fig. E.1.

The next step is to get the axial motional frequencies as showed in Fig. E.2. Here we should give the RF voltage U , the driving frequency Ω and also the ion-electrode distance $\rho\rho$ in the code. Finally we can get the radial frequencies and also the mode vector as showed in Fig. E.3. Once we get the mode vector, we can multiply it with η to get $\eta_{i,m}$.

```

Clear[A, e, V, M, ρ, χZ, χX, χY, e0, NN, z, s];
A = {171, 171, 137};
V = 1000;
χZ = 2; χX =  $\frac{-\chi Z}{2}$ ; χY =  $\frac{-\chi Z}{2}$ ; ρ =  $10 \times 10^{-3}$ ;
e =  $1.6 \times 10^{-19}$ ; M =  $1.660538921 \times 10^{-27}$ ; e0 =  $8.854 \times 10^{-12}$ ;
NN = Length[A];
z[i_] := Symbol["z" <> ToString[Floor[i]]];
Print["v=2π ", Table[ $\sqrt{\frac{2 e V \chi Z}{A[[i]] M \rho^2}}$ , {i, 1, NN}]/(2 π 106), " MHz"];
Print[s = Chop[N[FindRoot[
  Table[ $\frac{2 e V \chi Z}{\rho^2} z[m] + \frac{e^2}{4 \pi e0} \left( -\text{Sum}\left[\frac{1}{(z[m] - z[n])^2}, \{n, 1, m-1\}\right] + \text{Sum}\left[\frac{1}{(z[m] - z[n])^2}, \{n, m+1, NN\}\right] \right) = 0, \{m, 1, NN\}$ ],
  Table[{z[m],  $\frac{m}{10}$ }, {m, 1, NN}]]]]];
Print[ListPlot[
  Table[{s[[i, 2]], 0},
    {i, 1, NN}
  ], Axes → {True, False}
  ], PlotStyle → Directive[PointSize[0.04], Black]
  ], PlotRange → All, AspectRatio → 0.2]
v=2π {0.755592, 0.755592, 0.844161} MHz
{z1 →  $-3.55528 \times 10^{-6}$ , z2 → 0, z3 →  $3.55528 \times 10^{-6}$ }

```




Fig. E.1 The Mathematica code used to get the position of an ion chain. We just need to configure the mass of different ion one by one in the list and the axial voltage, we can get the axial frequencies and the position of different ions.

```

Clear[U, xx, xy, Ω, ρρ];
U = 1000; Ω = 2 π 26 × 106; ρρ = 0.4 × 10-3; xx = 1; xy = -xx;

Print["ω=2π ", Table[ $\sqrt{\frac{2 e^2 U^2 x x^2}{(A[[i]] M)^2 \Omega^2 \rho \rho^4} + \frac{2 e V x x}{A[[i]] M \rho^2}}$ , {i, 1, NN}]/(2 π 106), " MHz"];

ω=2π {4.82267, 4.82267, 6.02688} MHz

Clear[AA, B, vv, v];
B = 0 IdentityMatrix[NN];
Do[B[[i, i]] =  $\frac{2 e V x z}{A[[i]] M \rho^2} + 2 \frac{e^2}{4 \pi \epsilon_0} \text{Sum}[\text{If}[i == j, 0, \frac{1}{A[[i]] M \text{Abs}[s[[i, 2]] - s[[j, 2]]]^3}], \{j, 1, NN\}], \{i, 1, NN\}];
AA = B + Table[ $\text{If}[i == j, 0, \frac{e^2}{4 \pi \epsilon_0} \frac{-2}{\sqrt{A[[i]] A[[j]]} M \text{Abs}[s[[i, 2]] - s[[j, 2]]]^3}], \{i, 1, NN\}, \{j, 1, NN\}];
Print["2π", Reverse[ $\sqrt{\text{Eigenvalues}[AA]}$ ]/(2 π 106), "MHz"];
Print[vv = -Reverse[Eigenvectors[AA]] // MatrixForm];
Print[v = Table[ $\frac{\sqrt{A[[j]]} vv[[1]][[i, j]]}{\sqrt{\text{Sum}[A[[j]] vv[[1]][[i, j]]^2, \{j, 1, NN\}]}}$ , {i, 1, NN}, {j, 1, NN}] // MatrixForm];
Print[Graphics[Table[Table[{Arrowheads[0.03], Thickness[0.001], Arrow[{{106 s[[j, 2]],  $\frac{-i}{3}$ }, {106 s[[j, 2]] + 1.5 v[[1]][[i, j]],  $\frac{-i}{3}$ }}}], {j, 1, NN}, {i, 1, NN}]]]

2π{0.780326, 1.38302, 1.86282}MHz
( 0.621009 0.602855 0.500913
  0.702287 -0.144181 -0.69714
 -0.348052 0.784715 -0.512915
  0.637105 0.61848 0.459979
  0.738895 -0.151696 -0.656523
 -0.357529 0.806081 -0.4716 )$$ 
```

Fig. E.2 The Mathematica code used to get the axial frequencies and mode vector of the axial mode of an ion chain. We should give the RF voltage U , frequency Ω and the ion-electrode distance $\rho\rho$.

```

Clear[CC, vv, v];
CC = DiagonalMatrix[Table[ $\frac{2 e^2 U^2}{(A[[i]] M)^2 \Omega^2 \rho \rho^4}$ , {i, 1, NN}]] -  $\frac{1}{2}$  AA;
Print["2 $\pi$ ", Reverse[ $\sqrt{\text{Eigenvalues}[CC]}$ ] / (2  $\pi$  106), "MHz"];
Print[vv = Reverse[Eigenvectors[CC]] // MatrixForm];
Print[v = Table[ $\frac{\sqrt{A[[j]]} vv[[1]][[i, j]]}{\sqrt{\text{Sum}[A[[j]] vv[[1]][[i, j]]^2, \{j, 1, NN\}]}}$ , {i, 1, NN}, {j, 1, NN}] // MatrixForm];
Print[Graphics[Table[Table[{Arrowheads[0.03], Thickness[0.004], Arrow[{{106 s[[j, 2]], -2 i},
{106 s[[j, 2]], -2 i + 1.5 v[[1]][[i, j]]}}]}, {j, 1, NN}, {i, 1, NN}]]];

```

2 π {4.69411, 4.79942, 5.97511}MHz

$$\begin{pmatrix} 0.5391 & -0.841744 & 0.0289532 \\ 0.842218 & 0.538511 & -0.0259741 \\ 0.0062719 & 0.0383875 & 0.999243 \end{pmatrix}$$

$$\begin{pmatrix} 0.539145 & -0.841814 & 0.0259176 \\ 0.842275 & 0.538547 & -0.0232504 \\ 0.00700577 & 0.0428792 & 0.999056 \end{pmatrix}$$

Fig. E.3 The Mathematica code used to get the radial frequencies and mode vector of an ion chain.

致 谢

衷心感谢导师 Kihwan Kim 副教授对本人的精心指导。他们的言传身教将使我终生受益。特别感谢吕定顺，没有他的协作我的工作是不可能顺利快速完成的。我的实验中没有张翔完成的控制系统和张君华完善的FPGA板也是不可能完成的。感谢实验室全体老师，行政人员和同学们的热情帮助和支持！

声 明

本人郑重声明：所呈交的学位论文，是本人在导师指导下，独立进行研究工作所取得的成果。尽我所知，除文中已经注明引用的内容外，本学位论文的研究成果不包含任何他人享有著作权的内容。对本论文所涉及的研究工作做出贡献的其他个人和集体，均已在文中以明确方式标明。

签 名：_____ 日 期：_____

个人简历、在学期间发表的学术论文与研究成果

个人简历

1989年11月19日出生于河南省洛阳市。

2008年9月考入北京大学物理学院物理专业，2012年7月本科毕业并获得理学学士学位。

2012年9月免试进入清华大学交叉信息研究院攻读理学博士学位至今。

发表的学术论文

- [1] **Shuoming An**, Dingshun Lv, Adolfo del Campo and Kihwan Kim, Shortcuts to adiabaticity by counterdiabatic driving for trapped-ion displacement in phase space, Nature Communications 7, 12999
- [2] **Shuoming An**, Jing-Ning Zhang, Mark Um, Dingshun Lv, Yao Lu, Junhua Zhang, Zhang-Qi Yin, H. T. Quan and Kihwan Kim, Experimental Test of Quantum Jarzynski Equality with a Trapped Ion System, Nature Physics 11, 193–199
- [3] Dingshun Lv, **Shuoming An**, Mark Um, Junhua Zhang, Jing-Ning Zhang, M. S. Kim, and Kihwan Kim Phys. Rev. A 95, 043813
- [4] Mark Um, Junhua Zhang, Dingshun Lv, Yao Lu, **Shuoming An**, Jing-Ning Zhang, Hyunchul Nha, MS Kim, Kihwan Kim, Phonon arithmetic in a trapped ion system, Nature Communications 7, 11410
- [5] Xiang Zhang, Mark Um, Junhua Zhang, **Shuoming An**, Ye Wang, Dong-ling Deng, Chao Shen, Luming Duan and Kihwan Kim, State-independent experimental test of quantum contextuality with a single trapped ion, Physical review letters 110 (7), 070401